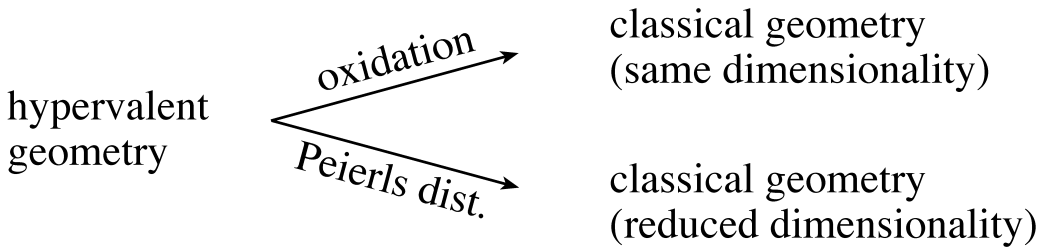

Examples

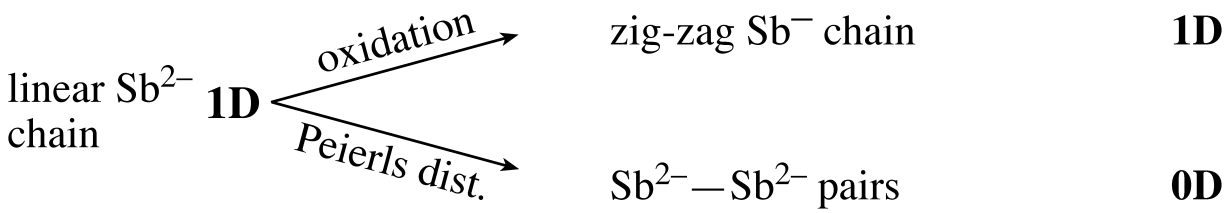

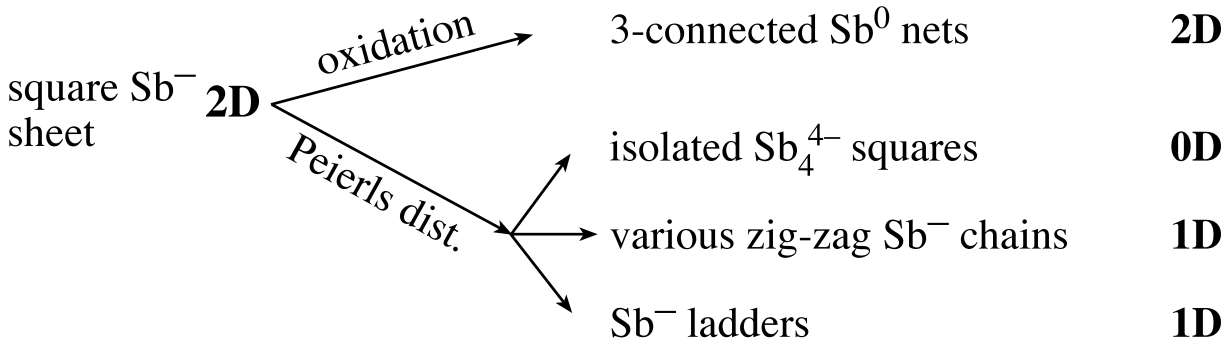

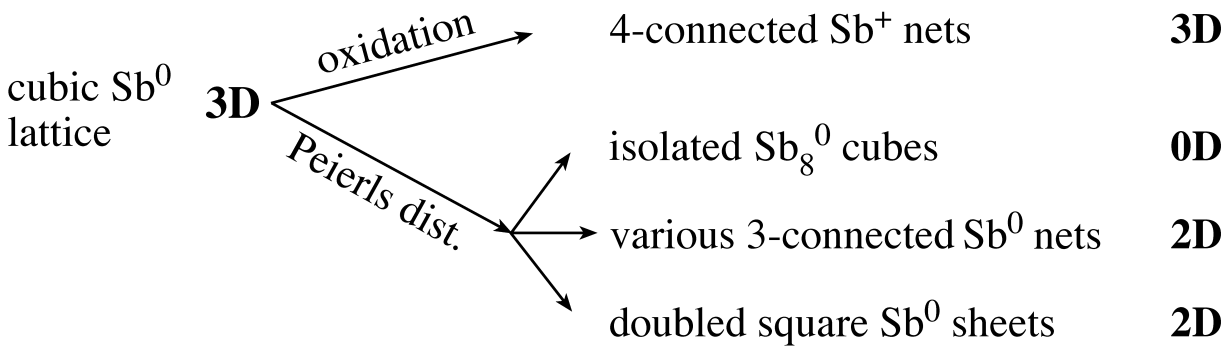

Hypervalent Bonding in One, Two, and Three Dimensions: Extending the Zintl–Klemm Concept to Nonclassical Electron-Rich Networks

Garegin A. Papoian* and Roald Hoffmann*

We construct a theory for electron-rich polyanionic networks in the intermetallic compounds of heavy late main group elements, building a bonding framework that makes a connection to well-understood hypervalent bonding in small molecules such as XeF_4, XeF_2, and I_3^-. What we do is similar in spirit to the analogy between the Zintl–Klemm treatment of classical polyanionic networks and the octet rule for molecules. We show that the optimal electron count for a linear chain of a heavy main group element is seven electrons per atom, six electrons per atom for a square lattice, and five electrons per atom for a simple cubic lattice. Suggestions that these electron counts are appropriate already exist in the literature. We also derive electron counts for more complicated topologies, including one-dimensional ladders and one dimensional strips cut from a square lattice. We also study pairing (Peierls) distortions from these ideal geometries as well as other deformations. The presence of s-p mixing (or its absence) plays a critical role in the propensity for pairing and, in general, in determining the geometrical and electronic structure of these phases. Hypervalent bonding goes along with the relative absence of significant s-p interaction; there is a continuum of such mixing, but also a significant difference between the second-row and heavier elements. We attribute the existence of undistorted metallic networks of the latter elements to diminished s-p mixing, which in turn is due to the contraction of less-screened s orbitals relative to p orbitals down the groups in the Periodic Table. The number of electrons in the polyanionic network may be varied experimentally. An important general principle emerges from our theoretical analysis: upon oxidation a hypervalent structure transforms into a classical one with the same lattice dimensionality, while upon Peierls distortion the hypervalent structures transform into classical ones with the lattice dimensionality reduced. Dozens of crystal structure types, seemingly unrelated to each other, may be understood using the unifying concept of electron-rich multicenter bonding. Antimonides, which are explored in great detail in the current work, conform particularly well to the set of electron counting rules for electron-rich nonclassical networks. Some deviation up and down from the ideal electron count is exhibited by known stannides and tellurides. We can also make sense of the bonding in substantially more complicated alloys, including $La_{12}Mn_2Sb_{30}$ and Tl_4SnTe_3. The hypervalent electron counting scheme developed in this paper, along with the classical Zintl–Klemm electron counting rules, gives an easy qualitative understanding of bonding in a wide variety of intermetallic compounds of heavy main group elements.

Keywords: bond theory · hypervalent compounds · solid-state structures

1. Introduction

A significant number of pieces of the diverse and important intermetallic mosaic is made up by phases containing heavy late main group elements. The majority of these networks obey classical Zintl–Klemm electron counting rules, among the most important and useful paradigms in solid-state chemistry.[1–3] However, many networks built from main group elements show an unusual, nonclassical local coordination, for instance, a triangular one (in polyhedra) or a linear one, as in one-dimensional linear chains or two-dimensional square sheets. Along with the unusual geometries often come interesting physical properties such as metallic conductivity.

Some intermetallic systems are electron deficient. Indeed, first, second, and Group 13 elements form networks[4] with an abundance of triangular faces. This tendency has been rationalized within the context of a moments theory by a large and energy-controling third moment for the low electron count.[5, 6] Certain groups of extended electron-deficient compounds may be understood by the application of

[*] Dr. G. A. Papoian, Prof. Dr. R. Hoffmann
Department of Chemistry and Chemical Biology
and Materials Science Center
Cornell University, Ithaca NY 14853-1301 (USA)
Fax: (+1) 607-255-5707
E-mail: rh34@cornell.edu

  1433-7851/00/3912-2409 $ 17.50+.50/0

Wade–Mingos rules, which give a guide to magic electron counts for some common polyhedra.[7–10] An important review of bonding in electron-deficient intermetallic compounds has been written by Nesper.[11]

On the right side of the Periodic Table (the late main group elements) bonding in intermetallic phases is very different. These electron-rich compounds often feature locally "linear" nonclassical geometries, two-dimensional square sheets, and a number of fascinating geometries derived from these.

Electron counting schemes for these unusual electron-rich geometries are the main subject of this review and antimony is our entry point. We choose antimony as our workhorse example, prompted by its rich structural chemistry. However, our ideas are applicable to a variety of structures of other late main group elements as well, and we discuss a selection of these.

Suggestions of appropriate electron counts in the nonclassical geometries encountered in the remarkably rich chemistry of antimony have arisen from experimental studies. For instance, Jeitschko and co-workers[12, 13] proposed that one should count long bonds as one electron in the one dimensional (1D) linear Sb chain in U_3TiSb_5 and in the 2D square Sb sheet in $CeAgSb_2$. Nesper[14] suggested one electron per bond in the 1D linear chain in Li_2Sb,[15] also on the basis of the long bond length determined experimentally. He also argued[14] that the square Bi sheet in LiBi is stable because of the relativistic contraction of s orbitals, that is, only p orbitals are involved in bonding. A similar, more general argument concerning the contraction (relativistic and nonrelativistic) of s orbitals down the groups, is one of the cornerstones of our analysis.

Are the electron counts proposed above a general phenomenon characteristic of all late main group elements and, if yes, what are the reasons behind that? We will provide a theoretical rationale for these electron counts in two ways: by using conventional molecular orbital theory[16] and band structure analysis.[17] In addition, we will suggest new optimal electron counts for a 3D simple cubic lattice, 1D strips cut from a square lattice, and a number of other nonclassical frameworks. Most importantly, we will provide and exemplify an aufbau principle for analyzing any hypervalent network.

In the theoretical section we explain a phenomenon that at first seems quite disjoint from the above unusual geometries—the important tendency of heavier late main group elements to remain metallic while lighter elements in the group undergo Peierls distortion[18] to become semiconductors or insulators. We also consider Peierls distortion pathways for various nonclassical bonding geometries, in particular for a square net. This subject has been studied earlier by our group[19] as well as by Lee and co-workers.[20–24] Finally, the electron counting scheme developed for simple networks with electron-rich multicenter bonding will show its utility in an analysis of the bonding in quite complicated anionic sublattices, such as those that occur in the intermetallic phases $La_{12}Mn_2Sb_{30}$ and Tl_4SnTe_3.

2. A Roadmap

In order to facilitate reading of this paper a brief description of the remaining sections is given below:

- Section 3: The many classical and hypervalent Sb networks are reviewed. A general electron counting scheme emerges

Garegin A. Papoian was born in Yerevan, Armenia in 1973. He completed four years of undergraduate studies in the Higher College of the Russian Accadamy of Sciences, carrying out research under the guidance of Pofessor Alexander Pasynskii. After completing an M.S. degree from the University of Kansas in 1995, he was a Ph.D student in the Department of Chemistry at Cornell University working with Roald Hoffmann and completed his studies on a wide variaty of problems in solid-state chemistry and heterogeneous catalysis in 1999. He then joined the research group of Professor Michael Klein at the University of Pennsylvania as a postdoctoral associate. His current research interests lie in the application of quantum mechanical and statistical mechanical methods to important chemical and physical properties of solid-state, surface-catalytic, and biocatalytic systems.

G. A. Papoian

R. Hoffmann

Roald Hoffmann was born in 1937 in Zloczow, Poland. He moved to the U.S. in 1949 and studied chemistry at Columbia University and Harvard University (Ph.D 1962). Since 1965 he has been at Cornell University, now as the Frank H. T. Rhodes Professor of Humane Letters. He has received many of the honors of his profession, including the 1981 Nobel Prize in Chemistry (shared with Kenichi Fukui). "Applied theoretical chemistry" is the way Roald Hoffmann likes to characterize the particular blend of computations which are stimulated by experiment and the construction of generalized models, of frameworks for understanding, that is his contribution to chemistry. Dr. Hoffmann also has a career as a writer, that profession sometimes overlapping his chemistry, sometimes not. He writes poems, essays, nonfiction, and plays.

for hypervalent networks, which applies to all Sb phases known to us.

- Sections 4–8: The major assumptions of our theoretical model are given. A theory is developed which rationalizes electron counting in hypervalent networks. The tendency of heavier elements to form metallic frameworks as well as the distortion pathways of hypervalent networks is explored. The interrelationship of electron counting, dimensionality, and Peierls distortion is highlighted.
- Section 9: The theory developed in Sections 4–8 is applied to a seemingly complicated $La_{12}Mn_2Sb_{30}$ alloy. Retrotheoretical analysis is introduced as a powerful strategy to understand solid-state compounds which contain several sublattices.
- Section 10: We look at linear chains and derivative networks made up of main group elements other than Sb.
- Section 11: Electron counting and the stability of a wide range of binary, ternary, and quaternary phases of Group 14 elements containing square sheets are discussed in detail.
- Section 12: The upper stability range of electron counting in square sheets is examined in chalcogen compounds. The charge density wave (CDW) distortions of the latter sheets are reviewed.
- Section 13: Conclusions.

Now we are ready to take a close look at Sb networks in a wide variety of Sb phases. The observed structures are at the same time striking and complex, begging to be shown and explained.

3. Electron Counting in Individual Structures

The basic idea behind the Zintl–Klemm concept is the transfer of electrons from more electropositive elements to more electronegative elements, with the potential for the formation of strong bonds between the latter. This protocol usually works well with alkali, alkaline earth, and rare earth elements as electron donors. Things are not so simple for the transition metals, where multiple oxidation states are common and the electronegativities approach and even surpass those of some main group elements. Among the hundreds of Sb phases reported we have selected those where the extent of the electron donation to the Sb network is unambiguous. This approach does exclude many transition metal antimonides from Table 1, which is a selective listing of a variety of Sb phases characterized by classical and nonclassical structural elements.

We included some transition metals in our study for the following reasons: Firstly, magnetic measurements have been carried out on some Mn compounds, and this has allowed the assignment of a nonambigious formal charge to Mn. Secondly, FeS_2-m (marcasite) type transition metal diantimonides show a very interesting pattern of stacking of Sb–Sb pairs into a 1D ladder, which is dependent on the metal. Such strips are related to one of the geometrical patterns we analyze. Similarly, zirconium phases of antimony contain 1D strips that are electronically intriguing. We will talk about them in Section 6.2.

In this section we first apply the Zintl–Klemm electron counting concept to Sb phases with classical geometries. We

Table 1. Geometries of Sb subnetworks in various compounds.

Compound	Structure type	Geometrical patterns	
		classical	hypervalent
Ba_5Sb_4[245]	Sm_5Ge_4	0D pairs, atoms	
$Li_4Sr_3Sb_4$[246]	$Li_4Sr_3Sb_4$	0D pairs, atoms	
Zn_4Sb_3[247, 248]	Zn_4Sb_3	0D pairs, atoms	
ZnSb[249]	CdSb	0D pairs	
$EuNi_{1.51}Sb_2$[250]	$ThCr_2Si_2$	0D pairs	
$CoSb_2$[74]	$CoSb_2$	0D pairs	see the text
$Ca_{11}Sb_{10}$[251]	$Ho_{11}Ge_{10}$	0D squares, pairs, atoms	
$CoSb_3$[33]	$CoAs_3$	0D squares	
REM_4Sb_{12}[a][30, 31]	$CoAs_3$	0D squares	
(Ba_2Sb_3,[36] Eu_2Sb_3,[37] Sr_2Sb_3[38])	Sr_2Sb_3	0D Sb_6 zig-zag units	
KSb[39]	LiAs	1D helical chains	
RbSb[252]	NaP	1D helical chains	
$CaSb_2$,[253] $EuSb_2$[40]	$CaSb_2$	1D zig-zag chains	
KSb_2[254]	KSb_2	1D ribbon; edge-sharing Sb_6 octahedra	
$BaSb_3$[43]	BaP_3	2D 2,3-connected nets	
Sb[44]	As	2D 3-connected nets	
$Eu_{14}MnSb_{11}$[49]	$Ca_{14}AlSb_{11}$	0D atoms	linear 0D Sb_3 units
($CrSb_2$,[255] $FeSb_2$,[72] $CoSb_2$,[256] $NiSb_2$[257])	FeS_2	0D pairs	see the text
Li_2Sb[15]	Li_2Sb	0D pairs	linear 1D chains
U_3MSb_5 (M = Ti, V, Cr, Mn)[12]	"Anti"-Hf_5Sn_3Cu	0D atoms	linear 1D chains
La_3MSb_5(M = Zr, Hf)[58]	"Anti"-Hf_5Sn_3Cu	0D atoms	linear 1D chains
$LaSb_2$, $CeSb_2$, $SmSb_2$[258–260, 62]	$SmSb_2$	0D pairs	2D square sheets
($LaCrSb_3$,[58] $CeCrSb_3$[261])	$CeCrSb_3$	0D pairs, atoms	2D square sheets
$BaCu_2Sb_2$[262]	$BaCu_2Sb_2$	0D pairs, atoms	square 2D sheets
$EuCu_2Sb_2$,[262] $LaNi_{1.51}Sb_2$[250]	$CaBe_2Ge_2$	0D atoms	2D square sheets
REM_xSb_2[b][13, 64–70]	$ZrCuSi_2$	0D atoms	2D square sheets
$YbSb_2$[61]	$ZrSi_2$	1D zig-zag chains	2D square sheets
$M_6M'Sb_{15}$ (M = La, Ce; M′ = Mn, Cu, Zn)[71]	La_6MnSb_{15}	0D atoms, 1D Sb_3 strips, 3D Sb_{10} network	
$ZrSb_2$[105]	Co_2Si	1D Sb_4 strips	
$ZrSb_2$[106]	$ZrSb_2$	1D Sb_6 strips	

[a] RE = La, Ce, Pr, Nd, Sm, Eu; M = Fe, Ru. [b] RE = rare earth element, M = Mn, Fe, Co, Ni, Cu, Zn, Pt, Pd, Cd, Ag, Au.

show that Sb can act as a "well-behaved" Zintl–Klemm element. Then, we examine Sb phases containing unusual 1D linear chains and 2D square sheets, invoking the previously conjectured electron counting generalizations. We finish this section by analyzing the sidewise fusion of two 1D linear chains to produce 1D ladders.

3.1. Classical Geometries: 0D Sb_2 Pairs and Sb_4 Squares

The most commonly occurring Sb substructure with an Sb–Sb bond is an Sb_2 pair. In theory, the pair can have seven, six, or five electrons per Sb, which would formally correspond to single, double, or triple bonds (Scheme 1). However, π

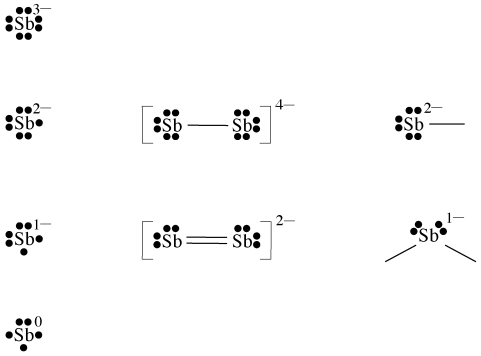

Scheme 1.

bonding is weak and rare for heavier elements, and usually only σ-bonded species are found. The typical range of observed bond lengths for the Sb_2 fragment in these phases is 2.80–2.90 Å. An unambiguous Sb–Sb single bond in a molecular hydrazine analogue, $(CH_3)_2Sb–Sb(CH_3)_2$, is 2.87 Å is used for calibration. Recently, the first Sb–Sb double bond (2.64 Å) in a molecular compound has been reported.[25]

The overwhelming majority of Sb phases containing just pairs and atoms conforms to the Zintl–Klemm concept. Thus, upon completing the octet, an isolated Sb atom should be formally −3 and Sb in a single-bonded pair −2. We considered Ba_5Sb_4 as an example (Entry 1 in Table 1). We do not show the structure, but two of the four Sb atoms per formula unit are isolated and two form a pair. The charges in Ba_5Sb_4 can be assigned as $(Ba_5)^{10+}(Sb_2^{atom})^{6-}(Sb_2^{pair})^{4-}$. The Sb–Sb separation in the pairs is 2.89 Å, which is within the normal range for a single bond. From here on we will use the label "atom" for an isolated or single atom in a structure. Similarly, the formal charges on $Li_4Sr_3Sb_4$ (Entry 2 in Table 1) can be assigned as $(Li_4)^{4+}(Sr_3)^{6+}(Sb_2^{atom})^{6-}(Sb_2^{pair})^{4-}$ on the basis of the multiplicities of Sb positions in the crystal structure. Note that these simple assignments do necessitate a knowledge of the structure of the phase, a typical (and productive) piece of nearly circular chemical reasoning.[26]

Isolated Sb_4 squares are also quite common within antimony phases. If one completes an octet around each Sb in the Sb_4 square, then one is led to a −1 charge to each Sb.[27] For example, $Ca_{11}Sb_{10}$ contains one isolated Sb_4 square, four Sb_2 pairs, and eight Sb atoms per two formula units (Figure 1).

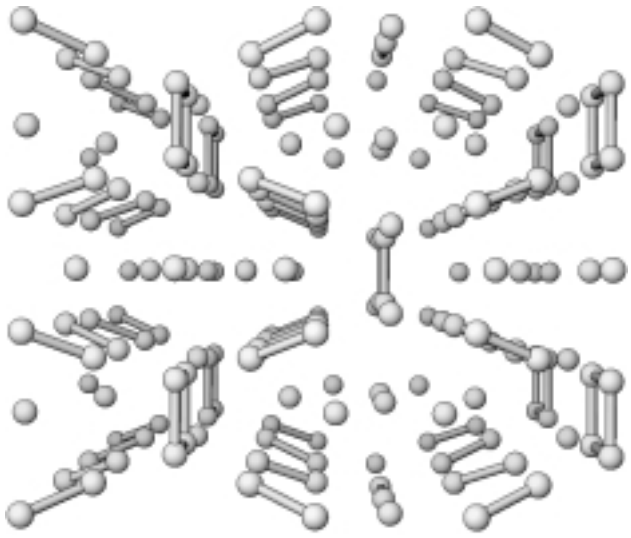

Figure 1. A perspective view of the Sb sublattice of the $Ca_{11}Sb_{10}$ crystal structure.

Following the Zintl–Klemm viewpoint, these molecular entities should carry a −1, −2, and −3 charge, respectively. Indeed, taking into account the multiplicities of the different kinds of atoms in the crystal structure, a simple charge assignment is established: $(Ca_{22})^{44+}(Sb_4^{square})^{4-}(Sb_8^{pair})^{16-}(Sb_8^{atom})^{24-}$.

The presence of transition metals complicates the bonding picture for the antimony phases with the relatively popular and fascinating skutterudite[28–31] ($CoAs_3$-type) structure. For a detailed description of bonding in these fascinating solids we refer readers to the original papers of Jung, Whangbo, and Alvarez[32] and Jeitschko and their co-workers.[31]

The picture of bonding is slightly more simple in the binary representatives of the skutterudite family, such as $CoSb_3$.[33] If one assigns a −1 charge to the Sb in squares (classical isolated Sb_4^{4-} squares), then Co becomes 3+ in $CoSb_3$.[31, 32] This d^6 electron configuration on octahedrally coordinated Co satisfies the 18 electron rule. Therefore, one expects semiconducting behavior for $CoSb_3$, and this has been observed for isoelectronic CoP_3, $RhAs_3$, $IrAs_3$, $IrSb_3$, and some other ternary skutterudites.[34, 35]

3.2. Classical Geometries: Zig-Zag Chains

The crystal structure of Ba_2Sb_3,[36] Eu_2Sb_3,[37] and Sr_2Sb_3[38]) contains isolated zig-zag chains of Sb_6 (Scheme 2). The Sb–Sb bond lengths range from 2.86 to 3.00 Å. If one completes an octet around each Sb atom in the chain, then the charges can be assigned as $(Ba_2)^{4+}Sb^{2-}Sb^{-}Sb^{-}$. This compound thus obeys the Zintl–Klemm electron counting rules.

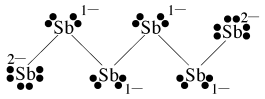

Scheme 2.

In contrast to these isolated Sb_6 units, the zig-zag chains that we discuss next are extended one-dimensional arrays. A perspective view of the Sb sublattice of the KSb crystal structure[39] is shown in Figure 2.

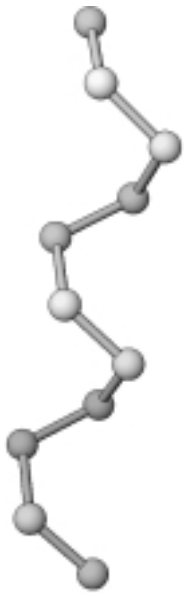

Figure 2. A perspective view of the Sb sublattice of the KSb crystal structure.

The Sb atoms form a helix, with Sb–Sb bonds of 2.83 and 2.88 Å. It is natural to assign a $1+$ charge to the potassium atom, which makes the antimony center -1. The Sb^- ion is isoelectronic to the Te atom, which indeed forms helical chains in its elemental structure. The Sb^- ions in RbSb (Table 1) also forms helical chains, but with a somewhat different conformation.

In contrast to KSb and RbSb the zig-zag chains of Sb ions in $CaSb_2$ and $EuSb_2$ (Table 1) are planar. A perspective view of the $EuSb_2$ crystal structure is given in Figure 3. The Sb–Sb distance in the chains is 2.93 Å. These compounds are also classical, since the cations are divalent (established by magnetic measurements for Eu compounds[40]). This assignment leads one to a -1 charge on the Sb center, which would be consistent with a twofold coordination. In Figure 3 one observes that the Sb chains are planar.

Why are such Sb^- chains sometimes helical and sometimes planar? A hint is provided by the shortest interchain distance in the horizontal planes being 3.54 Å (Figure 3), which can be thought of as a secondary

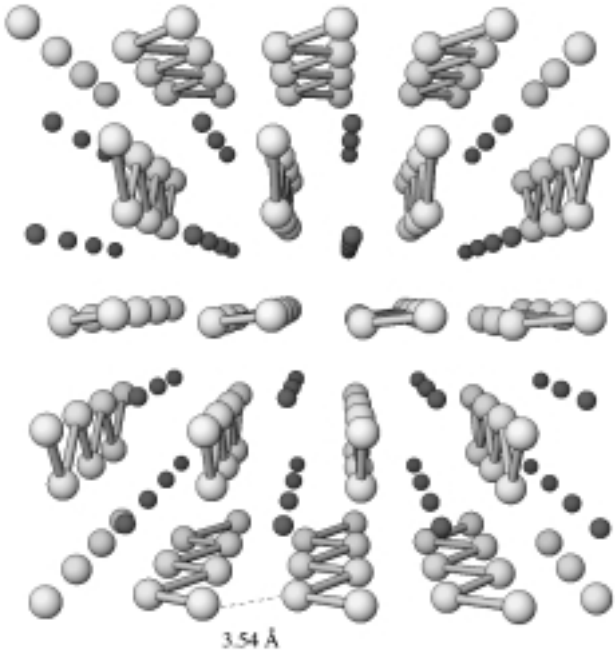

Figure 3. A perspective view of the $EuSb_2$ crystal structure. Eu = small dark spheres; Sb = large light spheres.

interaction[41, 42] (this assumption is supported by the near-linear Sb–Sb···Sb angle). When we examine the $YbSb_2$ and $SmSb_2$ crystal structures, we will consider the possibility of fusing the 1D zig-zag chains to give a square lattice.

3.3. Classical Geometries: Two-Dimensional Structures

We want to discuss two structures in this subsection: that of $BaSb_3$[43] and that of elemental Sb.[44] The former forms a two-dimensional 2,3-connected Sb net (Figure 4). As in the case of

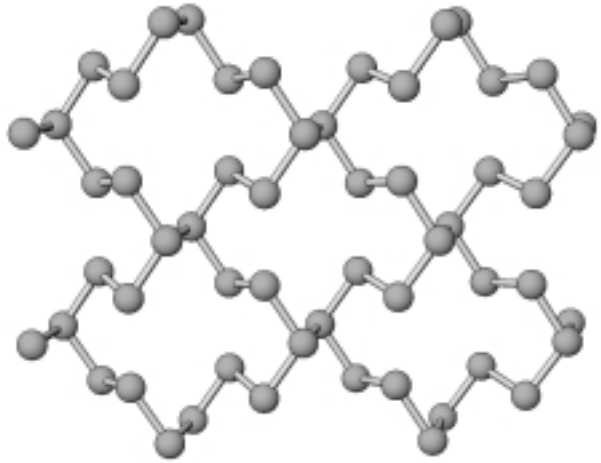

Figure 4. A perspective view of the Sb substructure of the $BaSb_3$ crystal structure.

the ribbons discussed above, we count three-connected Sb centers as neutral and two-connected Sb centers as Sb^-. Taking into account the site multiplicities in the crystal, the charges may be assigned as $Ba^{2+}Sb^0(Sb_2)^{2-}$. The Sb–Sb bonds in the crystal structure are around 2.85 Å, within the normal range. By any criterion, Sb acts as a good Zintl–Klemm element in this compound.

The crystal structure of elemental As-type Sb (Figure 5) is easy to understand, yet has some interesting features in it. If one chooses to ignore the 3.34 Å Sb–Sb inter-sheet contacts,

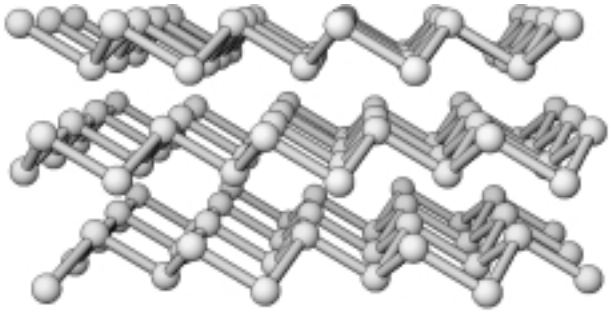

Figure 5. A perspective view of the crystal structure of elemental Sb.

then bonding in elemental Sb can be described as three-connected neutral Sb atoms that form a two-dimensional sheet, with each Sb center being appropriately pyramidal. However, two details of the structure are unsettling. The 3.34 Å inter-sheet contact is significantly shorter than an Sb···Sb van der Waals contact. Another interesting fact is the slight elongation of the Sb–Sb bond within the sheets to 2.90 Å, compared with 2.85 Å found in the sheets of $BaSb_3$. All these facts point to the existence of secondary inter-sheet interactions that also weaken the bonding within the sheets. We

hinted earlier that similar interactions exist between zig-zag chains in $CaSb_2$ and $EuSb_2$. Indeed, under high pressure (between 6 GPa and 7.5 GPa) elemental Sb undergoes a phase transformation[45] to give a simple cubic structure (Po-type), which results in equal inter- and intra-sheet Sb–Sb bonds (2.99 Å). Cubic Sb has also been prepared as a metastable phase by quenching from liquid and vapor.[46] The Sb–Sb bond length in that phase is 3.16 Å, which is longer than that in Sb after high-pressure treatment. One can think of elemental As-type Sb as having undergone a Peierls distortion[18] from cubic Sb.[47] We will return to this viewpoint in the theoretical part (Section 6).

The above sections explore the remarkable range of "normal" Zintl–Klemm type bonding in antimony compounds. But this element does not confine itself to classical structures. Next we examine the numerous Sb phases with nonclassical Sb sublattices.

3.4. Hypervalent Geometries: Linear Chains

The simplest nonclassical Sb structure may be that found in $Ca_{14}AlSb_{11}$[48] (see also $Eu_{14}MnSb_{11}$[49]) in the form of Sb_3 linear units. If the charge on Al is $3+$, the cationic charge is $31+$ per formula unit. In $Eu_{14}MnSb_{11}$ the Eu center is thought to have a charge of $2+$ and Mn correspondingly $3+$. In both structures there are eight isolated Sb atoms, which contribute -24 to the charge balance. Therefore, the remaining Sb_3 group should carry a -7 charge. The Sb_3^{7-} unit is isoelectronic with I_3^- and XeF_2, which are both classical hypervalent or electron-rich four-electron three-center species. The Sb_3 linear geometry and long Sb–Sb bonds (3.20 Å in $Ca_{14}AlSb_{11}$, 3.26 Å in $Eu_{14}MnSb_{11}$) are consistent with this suggestion. Kauzlarich, Fong, and Gallup carried out pseudopotential planewave density functional theory (DFT) calculations[50] on the analogous $Ca_{14}GaAs_{11}$ structure.[51] Their calculations were fully consistent with the existence of hypervalent As_3^{7-} units.

A word is in order here about the general framework of hypervalent or four-electron three-center bonding. Multicenter bonding is a natural extension of covalent electron-pair bonding to electron-deficient or electron-rich systems. In the context of the latter, it was initially described by Rundle for I_3^- (or XeF_2).[52, 53, 54] The reader is also referred to the important paper by Musher.[55] If the terminal atoms contribute only p orbitals (as shown here) or some hybrids of like symmetry, and the central atom only a single p orbital, one obtains the set of MOs shown in Scheme 3. In the four

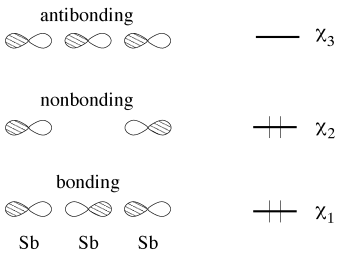

Scheme 3.

-electron system (only p orbitals of σ type are considered) χ_1 and χ_2 are occupied. The bonding scheme is modified slightly by the inclusion of an s orbital on the central atom. In that case χ_2 becomes somewhat antibonding through out-of-phase mixture of the central s orbital.

This bonding pattern may be used in a simple description of the axial bonding in PF_5, SF_4, and BrF_3 as well, though hypervalency in PF_5 has been questioned by Häser.[56] For square-planar systems (XeF_4, $TeBr_4^{2-}$) one has two perpendicular bonds of this type. The octahedral or deformed octahedral XeF_6 (and SbX_6^{3-}) have three such bonds.[57] SF_6 and SbX_6^- have two electrons less; however, a similar octahedral environment is also found in these compounds.[57]

Some people do not like the term hypervalent. We view it as a historically and heuristically useful categorization of bonding in electron-rich systems, and will use the term interchangeably with electron-rich multi-center bonding. Such bonding occurs in Sb_3^{7-}, and we will see it in linear, square net, and cubic sublattices of antimonides.

We return to our perusal of antimony bonding types. Extended linear chains of antimony atoms are found in Li_2Sb,[15] U_3MSb_5 (M = Ti,V,Cr,Mn),[12] La_3MSb_5 (Zr,Hf),[58] and other Sb phases. A perspective view of the Li_2Sb crystal structure is shown in Figure 6. There are two types of Sb in the

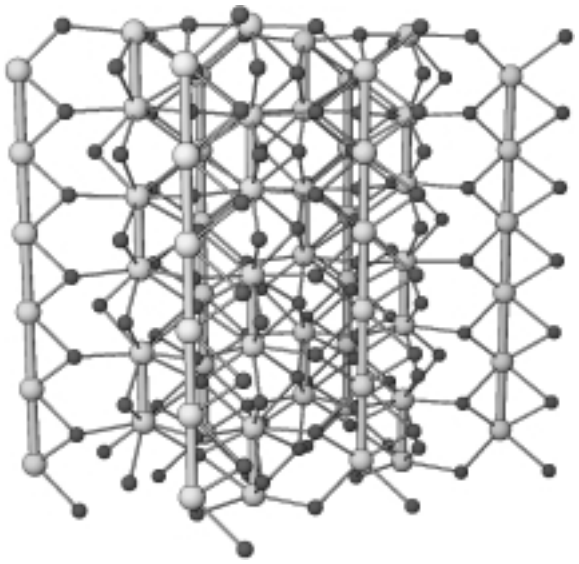
Figure 6. A perspective view of the Li_2Sb crystal structure. Li = small dark spheres; Sb = large light spheres.

crystal structure—Sb–Sb pairs and 1D linear chains, and both types occur in equal numbers. The Sb–Sb pairs are also stacked into a chain, but the inter-pair Sb–Sb contact is 3.56 Å, compared to 2.97 Å within the Sb_2 pair. In the linear chains all Sb–Sb bonds lengths are equal to 3.26 Å. This distance is long by comparison with an Sb–Sb single bond, but is definitely in the bonding regime. If one assigns a $1+$ charge to Li ions and a -2 charge to the Sb centers in the pairs, then one can assign a -2 charge also to the Sb atoms in the extended chains.

Before we take up this assignment in the theoretical section, we should mention again that Jeitschko and co-

workers,[13, 12] Nesper,[14] and Mar and co-workers[58] have suggested from empirical calculations that one consider long Sb–Sb bonds as half bonds (that is, one electron per bond). By making an implicit assumption of three additional lone pairs on each Sb atom, these authors have proposed a -2 charge for each Sb center in a linear chain, that is, three lone pairs and one bonding electron per Sb center. We will provide below a more formal theoretical analysis of this proposition.

In the theoretical section we will also consider the formation of Sb_2^{4-} pairs as the result of a Peierls (pairing) distortion in a one-dimensional linear Sb^{2-} chain with a half-filled band. What is surprising is that both Peierls distorted and undistorted chains coexist in the same crystal structure. The geometrical details alone of this fascinating structure indicate, we think, that the potential energy surface for Peierls distortion of Sb networks should be rather soft.

One-dimensional Sb chains are also found in U_3MSb_5 (M = Ti,V,Cr,Mn)[12] and La_3MSb_5 (M = Zr,Hf).[58] The Sb–Sb bonds in the linear chains again are somewhat long for both series of compounds, being around 3.17 Å for the former series and 3.06 Å in the latter. A perspective view of the La_3ZrSb_5 crystal structure is given in Figure 7. For two formula

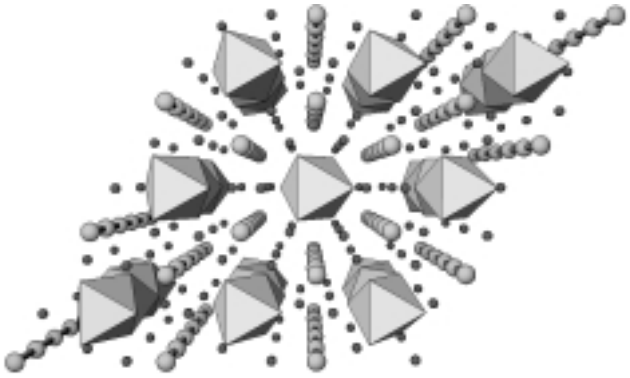

Figure 7. A perspective view of the La_3ZrSb_5 crystal structure. La = small dark spheres; Sb = large light spheres; $ZrSb_6$ octahedra are shown in a polyhedral representation.

units per unit cell, one could assume that cations donate $6 \times (+3) + 2 \times (+4) = (+26)$ electrons to the anionic framework. There are two kind of Sb atoms present in the crystal structure. Isolated Sb atoms, which comprise the Sb part of the face-sharing $ZrSb_3$ octahedral chains, occupy a six-fold Wyckoff position. Thus, they contribute a $6 \times (-3) = -18$ charge to the overall charge balance. The remaining Sb atoms in the linear Sb chains are found in a fourfold position, therefore each should carry a -2 charge in order to preserve the neutrality of the unit cell.[58]

A -2 charge per Sb atom in these linear chains was also suggested for La_3MSb_5(M = Ti,Hf)[58] and U_3TiSb_5.[12] A clear assignment of charges for the Mn analogue of the latter compound was not possible.[12] Sb–Sb bond lengths between Sb atoms in 1D linear chains vary greatly from compound to compound (for example, 3.26 Å in Li_2Sb and 3.06 Å in Sb_5MLa_3 (M = Zr, Hf)).

In summary, there are a number of Sb phases with linear Sb arrays. An electron count of seven electrons per Sb atom for 1D linear Sb chains makes sense of the electron counting in these structures. In these chains the Sb–Sb bonds are significantly elongated relative to a single Sb–Sb bond.

One final point should be made, which is relevant to the longer Sb–Sb bonds found in the linear arrays discussed here and also found in the square nets still to be mentioned. On one hand this is a reflection of the hypervalent bonding being weaker than normal electron pair bonding (compare, for instance, the I–I separation of 2.90 Å in I_3^- with 2.76 Å in diatomic I_2). There is also a connection to be made to donor–acceptor viewpoints of bonding and "secondary bonding" in numerous crystal structures. What we see are manifestations of a continuum between covalent bonding and closed-shell interactions, a subject that we[59] and others[60] have considered in detail elsewhere.

3.5. Hypervalent Geometries: Square Sheets

It is convenient to begin the discussion of square Sb sheets by first revisiting the structures of $CaSb_2$ and $EuSb_2$ (Table 1). We contemplated already the possibility of the horizontal zig-zag chains in Figure 3 collapsing into a square sheet. Indeed, this essentially happens in the $YbSb_2$ case (Figure 8).[61] Actually, the "square" sheets in $YbSb_2$ are slightly puckered,

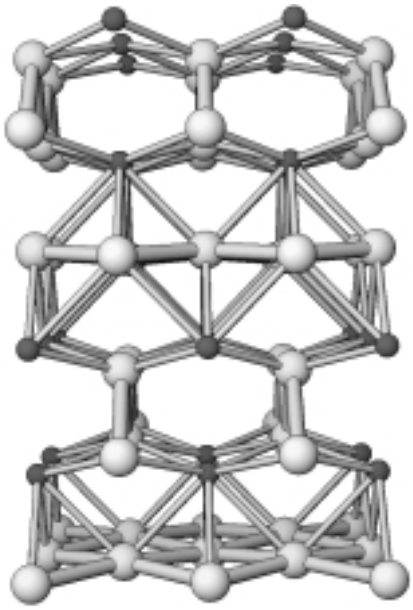

Figure 8. A perspective view of the crystal structure of $YbSb_2$. Yb = small dark spheres; Sb = large light spheres.

with Sb-Sb-Sb angles within the sheet of 93° and 86°. The Sb–Sb bond lengths are significantly longer (3.12 Å) than those found in the zig-zag chains of the $EuSb_2$ crystal structure (2.93 Å).

The magnetic susceptibility data for the Yb ion in $YbSb_2$ are consistent with Yb^{2+}, with a small (2%) admixture of the Yb^{3+} cation. If one assigns a -1 charge to Sb in the zig-zag chains (Figure 8), then Sb must also carry the same -1 charge in the approximately square sheets (there are as many chain Sb

atoms as those in the square sheet). Similar to a Peierls distortion of linear Sb^{2-} chains into the relatively isolated classical Sb_2^{4-} pairs (see the discussion on Li_2Sb in Section 3.4), square sheets of Sb^- ions may distort into classical zig-zag Sb^- chains (which could still have secondary interactions with each other). This, however, does not happen in $YbSb_2$. Tremel and Hoffmann argued that the existence of a small amount of Yb^{3+} ions in $YbSb_2$ suppresses the possible distortion to a zig-zag chain.[19] The electrostatic interactions within the lattice have to be taken into account as well to provide a detailed explanation of this behavior.

The crystal structures of $EuSb_2$ and $YbSb_2$ prompt us to think about what might happen to an Sb network of this type when a divalent rare earth element is replaced by a trivalent one. If we start with the $EuSb_2$ crystal structure (Figure 3), two resolutions come to mind. Upon reduction by one electron per two Sb atoms one of the two types of zig-zag chains might break into isolated pairs ($RE^{3+}(Sb^{zig\text{-}zag})^-(Sb^{pair})^{2-}$). If the newly formed $Sb_2^{pair\,4-}$ pairs are appropriately aligned, they might further fuse into a linear Sb chain. Alternatively, one could begin with the $YbSb_2$ structure with its approximately square sheets and zig-zag chains. One might guess that upon reduction the presumably weaker hypervalent bonds within the square sheets will disrupt before the break-up of classically bonded zig-zag chains. There is an implicit assumption here that the hypervalent bands, being only partially filled, would be occupied more easily by extra electrons than presumably high-lying empty antibonding orbitals of classical zig-zag chains.

Neither of those alternatives takes place in the $SmSb_2$ crystal structure (Figure 9)! Magnetic measurements for the isostructural Ce compound, $CeSb_2$, indicate a trivalency of rare earth cations.[62] Other rare earth atoms are also thought to be trivalent in rare earth diantimonides (La also forms an isostructural phase). The $SmSb_2$ structure is best viewed as derived from the $YbSb_2$ crystal structure by breaking the zig-zag chains into isolated pairs. The approximately square lattice of $YbSb_2$ becomes nearly ideal in $SmSb_2$ (Sb–Sb distances in the sheets are 3.03 Å and 3.09 Å). The Sb–Sb distance of 2.79 Å in Sb_2 pairs is within a normal Sb–Sb single bond range. Again the electron count is consistent with a -1 charge on the Sb atoms in the "square" sheets ($Sm^{3+}(Sb^{sheet})^-$-$(Sb^{pair})^{2-}$).

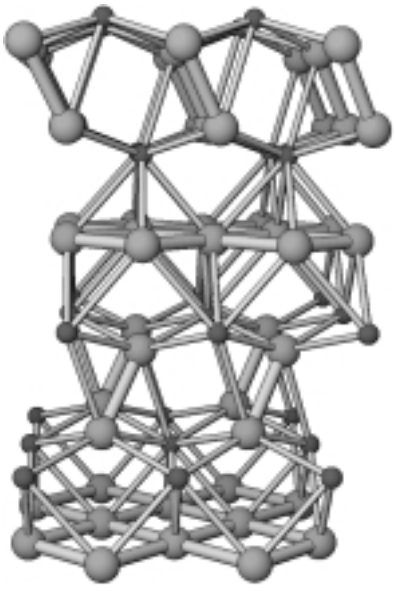

Figure 9. A perspective view of the crystal structure of $SmSb_2$. Sm = small dark spheres; Sb = large light spheres.

Perfect square Sb sheets are found[63] in the $BaZnSb_2$ crystal structure (Figure 10). Zn atoms are surrounded by isolated Sb atoms in a tetrahedral environment. The closest Sb···Sb contact between isolated Sb atoms is 4.49 Å, which is clearly nonbonding. The Sb–Sb bonds in the square sheets are rather long (3.24 Å), which is consistent with the observed trend for other square sheets. It is reasonable to assume that both Ba and Zn are dipositive, which requires again a -1 charge on Sb atoms in the square sheets. The charges on the elements in this compound then can be written as $Ba^{2+}Zn^{2+}(Sb^{sheet})^-(Sb^{atom})^{3-}$.

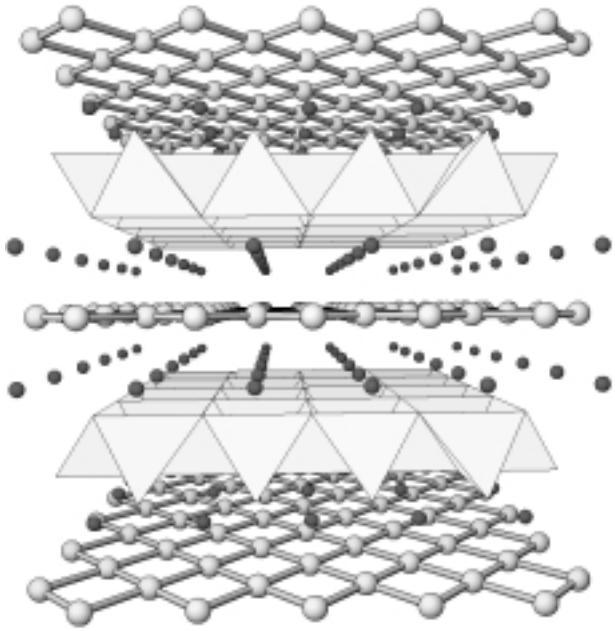

Figure 10. A perspective view of the crystal structure of $BaZnSb_2$. Ba = small dark spheres; Sb = large light spheres; $ZnSb_4$ tetrahedra are shown in a polyhedral representation.

Perfect square sheets exist in a wide variety of other antimonides. Among the most common of these[13, 64, 65, 66, 67, 68, 69, 70] are compounds with a stoichiometry REM_xSb_2, where RE stands for a rare earth, M is a transition metal (M = Mn, Fe, Co, Ni, Cu, Zn, Pt, Pd, Cd, Ag, Au), and x is usually less or equal to one. This structure is a variation of the $BaZnSb_2$ crystal structure given above. The rare earth ions in these compound have been shown[70, 71, 67, 68] to be tripositive. Since that $3+$ charge is exactly canceled out by a -3 charge on isolated Sb atoms (one of the Sb atoms is in the square sheet, one is isolated), the formal charge on Sb in the square sheets is determined solely by the charge on M_x part. If we assume a -1 charge on the square sheet Sb atoms, a count we have seen is consistent in other cases, we are led to a singly charged M ion if x is near one. The structures where this is plausible are $LaCu_{0.82-0.87}Sb_2$,[64] $REAgSb_2$,[67] $LaAuSb_2$,[69] and others. On

the other hand, if x is close to 0.5 then we expect the metal to be dipositive. This assumption seems quite reasonable for $LaZn_{0.52}Sb_2$.[64]

For other transition metals in this group of compounds, the assignment of charges becomes ambiguous. Here we will discuss only the Mn case, where good magnetic susceptibility data are available.[70, 68] The x value for these Mn compounds varies from 0.65 to 0.90. A magnetic moment of 4.3 μ_B, which corresponds roughly to four unpaired electrons, has been calculated for Mn atoms in $CeMn_{0.9}Sb_2$ (in addition to the Ce^{3+} magnetic moment). This result led the authors to assign a $3+$ charge to the Mn ion (d^4 configuration). This electron count then results in a large -2.7 charge per Sb atom in the sheets, but this fails to explain the relatively short Sb–Sb bonds in the sheets (3.10 Å)—there is very little that would hold the $Sb^{2.7-}$ centers together.

The Mn ions are located in a tetrahedral environment, where a high-spin d^6 configuration will also lead to four unpaired electrons (Scheme 4). We think that both the

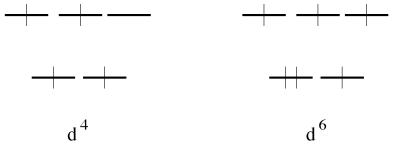

Scheme 4.

magnetic data and internal consistency of the structural information in $CeMn_{0.9}Sb_2$ allow an interpretation of the Mn oxidation state in these compounds as $+1$. Admittedly, this is not a usual oxidation state for the Mn ion.

In summary, many structures of antimonides which contain square or near-square Sb sheets give a consistent charge partitioning (in the Zintl–Klemm sense) if a -1 charge is assigned to each Sb atom in the square sheet. This is not an absolute requirement, for instance if we think about the $CeMn_xSb_2$ phase just discussed, the relatively large range of x values (0.65–0.9) indicates a fractional band filling in the square sheets. Eventually, by considering other main group elements, we will see a similar range of possible counts. The electron count of six electrons per Sb atom indicates only a preferred electron count, actual fluctuations around that number are to be expected, hopefully within a reasonably narrow range.

3.6. Other Geometries: The Marcasite- and Arsenopyrite-Type Compounds

Hybrid classical-hypervalent Sb subnetworks are present in transition metal dipnictides with the marcasite (FeS_2) crystal structure. A perspective view of the $FeSb_2$ crystal structure[72] is shown in Figure 11. One can view the Sb subnetwork as composed of regular Sb–Sb pairs (2.88 Å) that are stacked to form a one-dimensional ladder structure with an inter-pair Sb–Sb distance of 3.18 Å. An alternative (and perhaps more conventional) view would be to treat the Sb–Sb pairs as noninteracting units. A -2 charge is required to complete an

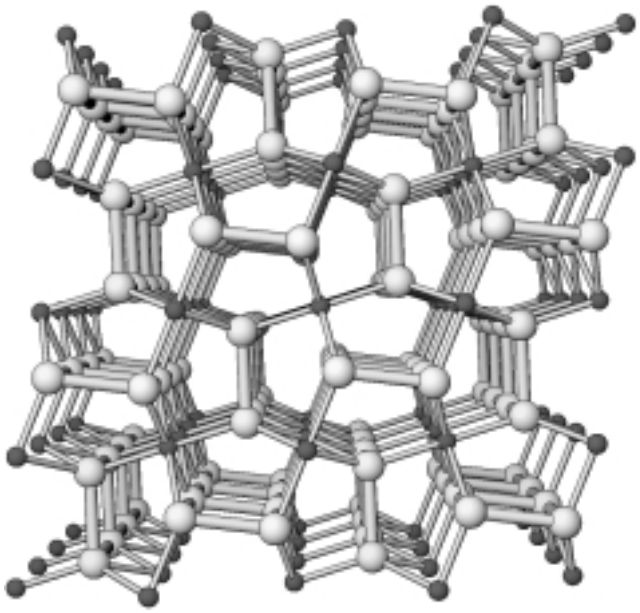

Figure 11. A perspective view of the crystal structure of $FeSb_2$. Fe = small dark spheres; Sb = large light spheres.

octet around each Sb in the latter case, which leads to a $4+$ charge on the metal center. Since the Sb electronegativity is not very high it is hard to justify such a high oxidation state on the transition metal atom, at least for some of the metals listed in Table 2. Relatively short inter-pair Sb–Sb distances also cast doubt on this line of reasoning.

Table 2. Geometrical data for the marcasite-type transition metal dianti-monides.

Compound	$CrSb_2$[255]	$FeSb_2$[72]	$CoSb_2$$[256]	$NiSb_2$[257]
intra-pair Sb–Sb distance [Å]	2.85	2.88 A	2.82 A	2.88 A
inter-pair Sb–Sb distance [Å]	3.27	3.19	3.37	3.84

Another approach would be to construct the Sb subnetwork in $FeSb_2$ beginning with a linear Sb chain (Sb–Sb distance of 3.19 Å). The electron count for such a chain should be seven electrons per Sb, as suggested in Section 3.4 and as we will prove in the theoretical section (Section 4). The next step is to pair up two linear chains to form the ladder structure. This would result in strong lone pair—lone pair repulsion (Scheme 5). To form Sb–Sb bonds between the chains, an

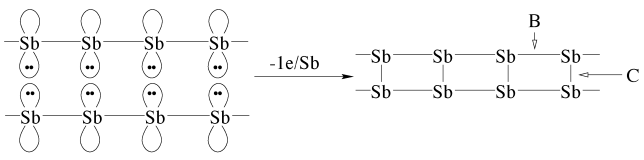

Scheme 5.

electron should be taken away from each Sb atom. This line of reasoning results in a -1 charge on each Sb center, which in turn corresponds to a formal $2+$ charge on Fe ions. The

resulting d^6 configuration for the octahedrally coordinated Fe ion is consistent with the 18e rule.

The analysis for the other metals in Table 2 is less clear. The intra-pair Sb–Sb distance (bond C in Scheme 5) becomes larger for Cr, Co, and Ni. In the Ni case the isolated pair view could be more justified, although again $4+$ is an unusual oxidation state for the Ni ion. On the other hand, if the Ni ion had a charge of $2+$, then Sb_2^{2-} would have a Sb–Sb double bond, something not supported by the Sb–Sb bond length (2.88 Å). Some experimental indication of the metal oxidation states would be very helpful in clarifying the issue of bonding within the Sb subnetworks of the marcasite type diantimonides. Holseth and Kjekshus[73] carried out magnetic susceptibility measurements on the marcasite-type dipnictides but, unfortunately, could not assign oxidation states to the transition metals. The arsenopyrite – marcasite phase transformation of $CoAs_2$ and $CoSb_2$ has been studied by Siegrist and Hulliger.[74] They have detected a phase transition, but the semiconductor – metal nature of this transition has not been confirmed. One might expect metallic properties for the marcasite structure because of the partial filling of the p_z band (z being the chain axis) in evenly spaced one-dimensional ladders (see the later discussion for more details).

An interesting connection can be made between the marcasite-type structures and the zig-zag ladders of main group elements as well as main group – transition metal elements. If a linear ladder were kinked at every Sb atom, then a zig-zag ladder would be produced (Scheme 6). An

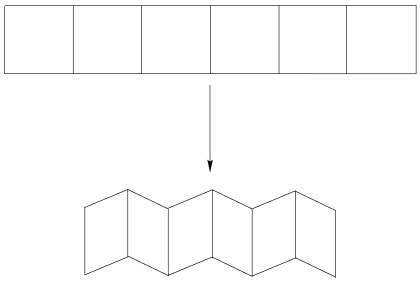

Scheme 6.

isolated zig-zag ladder contains three-connected classical atoms (pyramidal); appropriate to these would be an electron count of five electrons per atom. Zig-zag ladders could be fused together to produce the characteristic four-connected networks found in the $BaIn_2$-type[75] binary compounds and the TiNiSi-type[76] ternary compounds.

In the next section we present theoretical arguments for the conjectured electron counting schemes for nonclassical hypervalent networks.

4. Theory: Basic Principles

4.1. Assumptions of the Model

Our calculations, used throughout this work to support qualitative bonding considerations, are based on the extended Hückel (EH) method, an approximate molecular orbital (MO) theory.[77, 78, 79] Parameters for extended Hückel calculations are given in Appendix I (Section 14).

Key to our analysis will be an assumption of weak π interactions and weak (although, still significant) s-p mixing. Heavier main group elements are known to have weak π bonding, presumably because at the E–E distance set by the σ-bonding framework the p–p π overlap is quite small. Hence, the first assumption seems plausible. The weak s-p mixing can be traced to the contraction of the outer s orbital relative to the p orbitals down the groups in the Periodic Table. We will elaborate on this (and so understand the effect of including such mixing) when we discuss the *instability* of a hypothetical linear N^{2-} chain toward a pairing distortion, relative to an Sb^{2-} chain (such as the one that exists in Li_2Sb, for example). For the heaviest elements this contraction is further enhanced by relativistic effects, as was pointed out for these particular systems by Lohr[80] and by Nesper.[14] We will further explore this subject in this Section 4.6.

4.2. The Linear 1D Chain: A Simple MO Approach

There are several ways to derive an optimal electron count for a linear 1D Sb chain. We begin with a simple molecular orbital picture that does not require a band structure analysis.

The chain coordinate system is given in Scheme 7. By

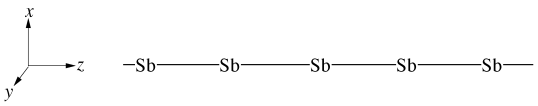

Scheme 7.

assuming weak π bonding and an excess of electrons, the p_x and p_y orbitals in the chain are essentially lone pairs. Furthermore, if we assume little s-p mixing occurs we can consider the s orbital simply as an occupied lone pair. Three filled lone pairs (Scheme 8) correspond already to six

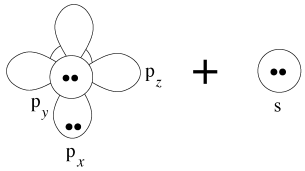

Scheme 8.

electrons per atom. Therefore, the final electron count will be determined by the occupancy of the remaining p_z orbital, which emerges as responsible for the presence or absence of bonding in the chain.

We consider first the oligomers which develop into this polymer. For a three-atom chain, the molecular orbitals are well known from the analysis of hypervalent bonding in, say, I_3^- or XeF_2.[54, 52, 53, 59] The two lowest orbitals are bonding and nonbonding, and the highest molecular orbital is antibonding (see Scheme 3). General bonding notions[16, 59] suggest the filling of all orbitals that are not strongly antibonding. In the

present instance this leads to four electrons in the p_z σ system and 18 electrons in lone pairs (s, p_x, and p_y), that is, an electron count of 22/3 electrons per atom for hypervalent I_3^- (or the related XeF_2).

Next we consider a linear chain with five atoms. While the orbitals are σ in character, they are "pentadienyl π-system-like" in terms of their phase relationships. The chain has three bonding and nonbonding p_z molecular orbitals (Scheme 9), filling which (along with the s, p_x, and p_y lone pairs) results in a electron count of $(6+5\times 6)/5 = 36/5$ electrons per atom. The extrapolation is clear[81]: an odd numbered *n*-member linear chain has $(n+1)/2$ bonding and nonbonding p_z levels (see Scheme 9) in addition to $3n$ s, p_x, and p_y lone pairs. To fill with two electrons per level all levels except the antibonding ones, one needs $2(3n+(n+1)/2) = 7n+1$ electrons. This amounts to $7+1/n$ electrons per atom. If *n* goes to infinity, as it does for

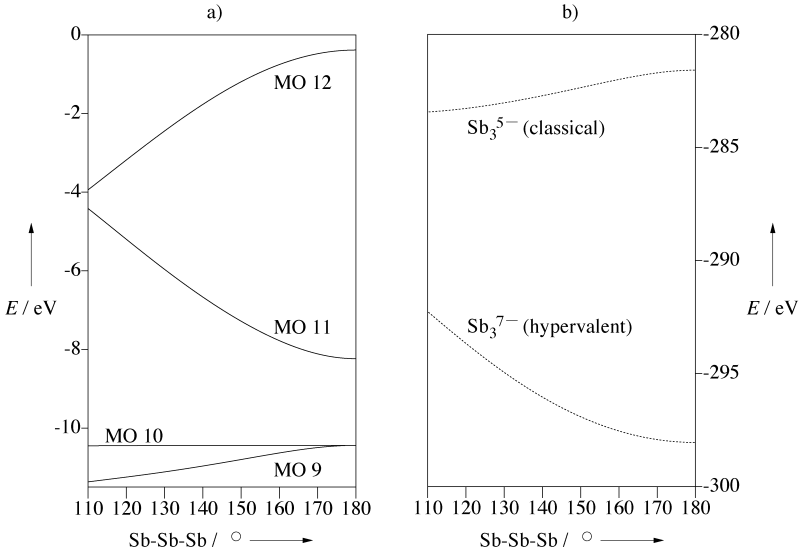

Figure 12. Walsh diagrams for the bending of Sb_3 molecules. a) Individual molecular orbital energies as a function of the bending angle; b) the total energy change for hypervalent Sb_3^{7-} and classical Sb_3^{5-} as a function of the bending angle. For Sb_3^{7-} MO 11 is filled.

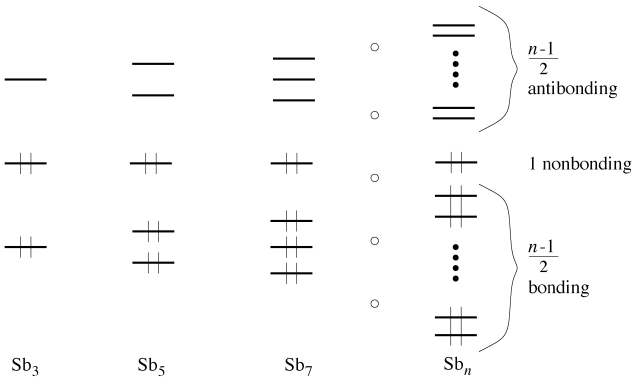

Scheme 9.

a one-dimensional linear chain, the proposed electron count of seven electrons per atom is obtained.

Before we derive the same result from a band structure analysis, we should compare the stability of a linear chain with this electron count with a kinked (zig-zag) chain. This comparison is familiar for the three-atom case, that is, for molecules such as XeF_2 and SF_2. XeF_2 has the hypervalent electron count of $7+⅓$ electrons per atom and it is linear, while SF_2 has a classical electron count, and it is bent. The isoelectronic Sb species, both found in the solid state, are Sb_3^{7-} and Sb_3^{5-}.[49, 71] The former ion is linear, while the latter one is bent, which is consistent with the molecular analogues.

A Walsh diagram for bending the Sb_3 unit is shown in Figure 12. Indeed, the 22 valence electron hypervalent structure prefers to be linear (Figure 12a) while the 20 electron classical one prefers to be bent (Figure 12b). The slope upon bending of the corresponding highest occupied molecular orbital (HOMO; MO 11) is responsible for the observed behavior. This MO is significantly destabilized upon bending, by mixing in an antibonding way with MO 9—one of the degenerate π orbitals (see Scheme 10, top). The HOMOs for the classical electron count are the doubly degenerate π

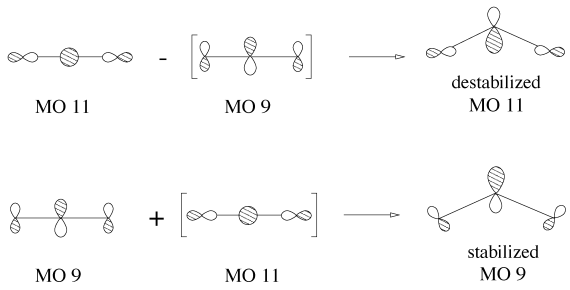

Scheme 10.

orbitals (MO 9 and 10). One of those orbitals becomes stabilized by mixing (now in a bonding way) with the higher lying MO 11 (see Scheme 10, bottom).

The energetic consequences for bending are enormous. For example, bending hypervalent Sb_3^{7-} from 180° to 110° costs 5.8 eV (Figure 12b). For classical Sb_3^{5-} the same bending leads to a stabilization by 1.85 eV. Clearly, the removal of two electrons from Sb_3^{7-} has a profound effect on its geometry. We emphasize this point because the same relationship between the locally linear and locally bent geometries is seen for infinite linear and kinked (zig-zag and helical) chains. And the energetic consequences (studied by us but not detailed here) are similar.

An even simpler explanation for the preferred geometries could be given within the VSEPR model.[82] Three lone pairs on the central atom in hypervalent Sb_3^{7-} occupy the equatorial positions in a trigonal bipyramid (Scheme 11, left), while

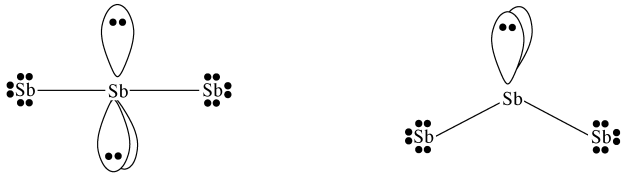

Scheme 11.

the side atoms occupy the axial positions of a trigonal bipyramid, in a linear arrangement with the central atom. The corresponding polyhedron for classical Sb_3^{5-} is a tetrahedron, with two lone pairs occupying two vertices, and two side atoms occupying the remaining two vertices (Scheme 11, right), creating an Sb-Sb-Sb bent geometry. The VSEPR picture is useful because it places bonds and lone pairs on a comparable basis.

On going to the extended geometries, the situation does not change much. For the classical electron count of six electrons per atom, zig-zag or helical chains are commonly found (elemental Te is a good example[83]; another example is the Sb sublattice in KSb[39]). On the contrary, the hypervalent electron count of seven electrons per atom is associated with linear chains, as exemplified by the Sb chains[15, 12, 58] which we discussed above. The molecular orbital picture behind this behavior is similar to the Walsh diagram (Figure 12) and VSEPR (Scheme 11) arguments given above.

We should mention that our analysis focuses on the bending coordinate in the structures. The question of the potential surface for an asymmetric stretch distortion, especially of the of the hypervalent Sb_3^{7-} (toward Sb_2^{4-} and Sb^{3-}) is not addressed. This distortion is easy in some analogous hypervalent species (for example, I_3^-) and not in others (PF_5). It is also related to the choice we will see Sb^{2-} chains make between hypervalent lines and paired distorted structures.

4.3. Linear 1D Chains: Band Structure Approach

In the previous subsection we demonstrated in one way that the electron count of seven electrons per atom is comfortable for a linear chain. Another way to come to this result is to use the band structure formalism.[17]

The computed band structure of an Sb chain at a 3.2 Å Sb–Sb distance is shown in Figure 13. If we ignore the s-p mixing (slight but not absent, as we will see), the shape of the resulting crystal orbitals is dictated purely by the symmetry and the topology of orbital interactions. Consider the s band (Figure 13): At Γ the crystal orbital is bonding and at Z it is antibonding. Since the s band is completely filled, its net effect on bonding is vanishing (all Sb–Sb bonding and antibonding combinations are filled), or even slightly antibonding (because of the bigger coefficients on the antibonding orbitals).

The π-interacting p_x and p_y orbitals "run up" along the Γ – Z line in the same manner as the s band (Figure 13). The flatness of the π band is consistent with our assumption of little π bonding. These two bands are also completely filled, therefore they do not contribute to bonding. The remaining band is σ type, based on the p_z orbital. This band "runs down" from Γ to Z. Midway between Γ and Z (at $k = \pm \pi/2a$), the p_z crystal orbital is nonbonding. The upper part of the p_z band is strongly antibonding. Destabilization within the chain would be expected if this part of the p_z band were to be filled. Therefore, a comfortable electron count (no σ-antibonding orbitals filled) is anticipated for a half-filled p_z band. With the completely filled s, p_x, p_y, and half-filled p_z band we arrive at the electron count of seven electrons per atom.

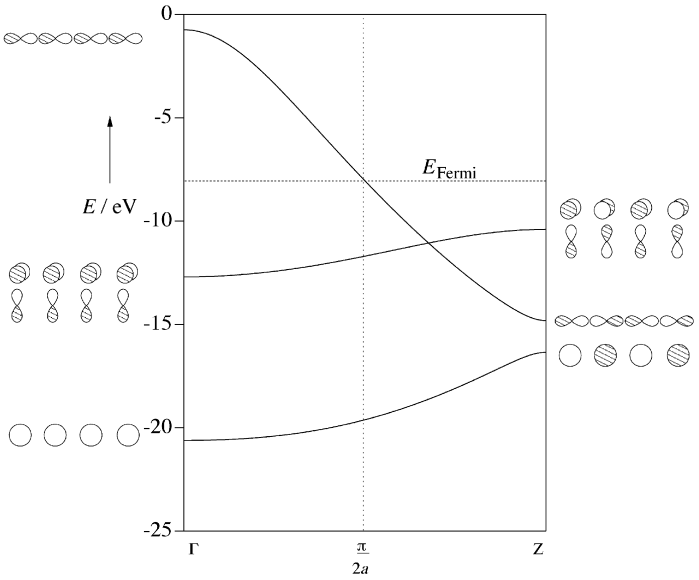

Figure 13. The band structure of a 1D Sb^{2-} chain with the Sb–Sb distance of 3.2 Å.

Note that the differential between σ and π bonding is very important in setting the favored electron count for hypervalent networks in this part of the Periodic Table. The entire width of the π band is below the center of gravity of the p_z σ band, and disparity in the $\sigma(p_z)$ versus $\pi(p_x, p_y)$ bonding exists. If this were otherwise, as in linear carbon chains, classical linear chains would be preferred at much lower electron counts. Instead of constructing the σ chain orbitals from the s lone pair and the p_z "hypervalent" band, as in Sb^{2-} linear chain, two carbon sp hybrids that develop into a band become a better starting point.[84] Taking also into account strong π bonding, linear carbon chains presumably have two double bonds per carbon atom and an electron count of four electrons per atom. It is reasonable to think that relatively strong π bonding ensures the linearity of these chains.

For the electron count of seven electrons per Sb atom, the linear chain is highly resistant to a kinking distortion. Molecular orbital considerations behind this were given in Section 4.2 for the three-atom oligomer Sb_3^{7-} (Scheme 10). In contrast, an electron count of six per atom strongly favors a kinking of the linear chain into a zig-zag chain, much in the same way as for molecular Sb_3^{5-}.

However, the Sb^{2-} linear chain, while possessing a reasonable electron count, is potentially susceptible to a pairing or Peierls distortion—a subject that we take up next. More detailed treatment of bonding patterns in infinite chains is given elsewhere.[85–87]

4.4. Peierls Distortion of a Linear 1D Sb^{2-} Chain

As we saw previously, Li_2Sb is a remarkable compound where both distorted (paired) and undistorted linear Sb

chains coexist in the same crystal structure (see Figure 6). The Sb–Sb distance in the undistorted chains is 3.26 Å and in the distorted (paired) chains the distance alternates between 2.97 and 3.56 Å.

When one sees a pairing one is naturally led to thinking of a Peierls distortion. A Peierls distortion is the extended system analogue of a Jahn–Teller distortion. For a given electron count there is a specific optimal coupling with a lattice vibration—a phonon mode—which reduces the symmetry of the lattice. In particular, a pairing distortion is indicated for a half-filled band.[17, 47, 88–91]

We already discussed the band structure of a linear Sb chain in the previous subsection. The band structure shown in Figure 13 is calculated for a unit cell containing only one Sb atom. It is not a convenient starting point for the Peierls distortion, because in the distorted chain the unit cell is doubled. Therefore, we start our analysis by doubling the unit cell of an ideal linear 1D Sb chain. In the absence of a deformation the physics and chemistry of bonding should not be changed by this hypothetical doubling process and we should obtain the same results as with the single unit cell.

What happens to the band structure in Figure 13 when the unit cell is doubled? There is an inverse relationship between the length of the direct and the reciprocal lattice vectors. By doubling the size of the direct lattice vectors, we halve the reciprocal unit cell. Since the total number of crystal orbitals must be conserved, there should be twice as many bands in the new Brillouin zone to compensate for the reduction of its size. The resulting band structure for the doubled unit cell is shown in Figure 14a. It can be thought of as a band structure for a normal cell (Figure 13) folded around vertical lines drawn at $+\pi/2a$ and $-\pi/2a$. A more detailed account of band structure folding can be found in ref. [17] and references therein by Burdett and Whangbo.

Next we examine a specific pairing distortion of an ideal chain ($\Delta = 0.1$ Å; for the definition of Δ see Scheme 12).

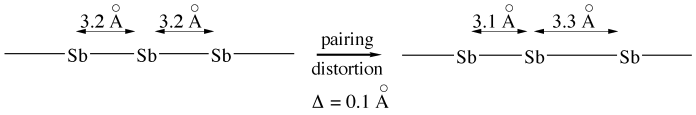

Scheme 12.

Because of the folding, all bands at Z are doubly degenerate. The pairing distortion removes that degeneracy, that is, the lower band of a pair becomes more stabilized and the upper band becomes destabilized. This may be seen for three pairs of bands in Figure 14b.

The susceptibility to the pairing distortion depends on the electron count in the chain. If the original unfolded band was fully occupied, then the stabilization of the lower branch of the folded band would not fully compensate the destabilization of the upper branch. If the original unfolded band was only half-occupied (as it is for Sb^{2-}) then the total energy is clearly lowered. Indeed, a pairing distortion of $\Delta = 0.1$ Å in magnitude occurring in an ideal Sb^{2-} chain (Sb–Sb distance of 3.2 Å) lowers the total energy by 0.16 eV per doubled unit cell in an extended Hückel (EH) calculation. The potential energy curve as a function of distortion parameter Δ is given in Figure 15 (what happens for a N^{2-} chain is discussed in the Section 4.5).

So far in our analysis we have neglected electrostatic and other forces present in real crystals. The simultaneous existence of Peierls-distorted and -undistorted linear chains in Li_2Sb indicates that other factors can overcome the driving force for the Peierls distortion. For this to happen, the potential energy surface for the pairing distortion should be shallow. Indeed, as Figure 15 shows, the energy lowering calculated for the pairing distortion in the Sb^{2-} chain is not large. A Δ value of 0.1 Å lowers the energy of the structure by only 0.16 eV.

The implications of the reasoning in the last paragraph are really important in the general context of the Periodic Table. Compounds that are susceptible to a Peierls distortion have partially filled bands, and that often makes them metallic. If the distortion occurs, then typically a band gap opens up at the Fermi level, and a metal to insulator transition occurs as well. If the potential energy surface for the Peierls distortion is shallow, the "chemical pressure" in solids[23] (this is one way one might think of Madelung and packing energies) may operate to keep the distortion from occurring. Then there will be a reasonable chance of finding late main group compounds with metallic properties. Indeed, the great majority of Sb phases containing linear chains and square sheets are metallic.

One often draws an a "diagonal" line in this region of the Periodic Table, separating nonmetallic and metallic main group elements. Could we explain the existence of the metal–nonmetal "diagonal" line by the shallowness/steepness of the potential energy surface for the Peierls distortion? In order to answer this

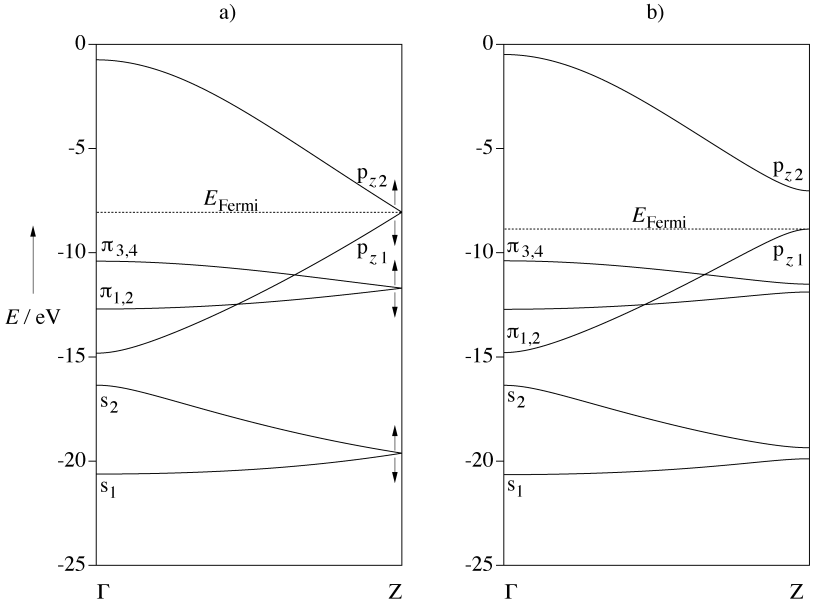

Figure 14. The band structure of a 1D Sb_2 chain with a) uniform Sb–Sb separations of 3.2 Å, b) alternating Sb–Sb distances of 3.1 and 3.3 Å.

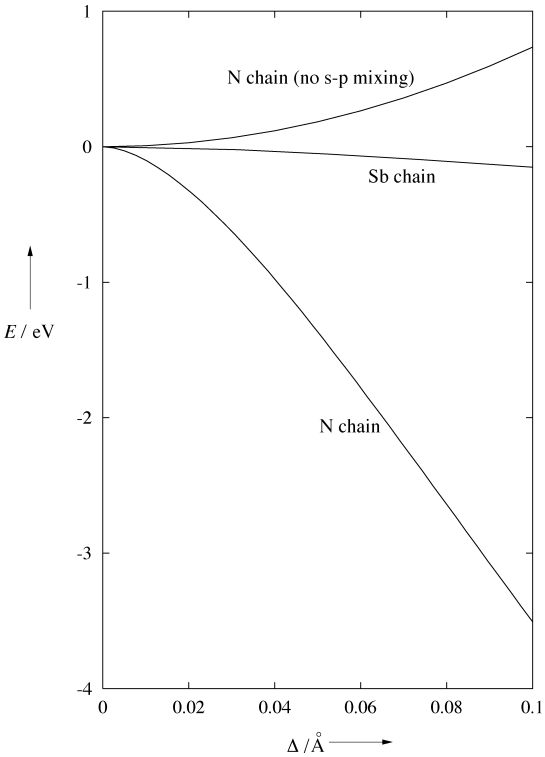

Figure 15. Total energy for Sb^{2-} and N^{2-} chains as a function of the distortion parameter Δ (for a definition of Δ see Scheme 12).

question, we consider next the Peierls distortion of a hypothetical (and nonexistent) linear N^{2-} chain.

4.5. Why a Linear 1D N^{2-} Chain Does Not Exist

The band structure of a linear 1D N^{2-} chain is shown in Figure 16a. We chose an N–N separation of 1.50 Å, a little greater than a single bond; there is no known structure to guide us here. Two assumptions that underlay our qualitative description of the band structure of an Sb chain are no longer valid. First, there are strong π interactions, reflected in the width (ca. 5 eV) of the π band in Figure 16a. Second, one notices immediately the unusually high position of the two "p_z" bands.

We remind ourselves of the bonding features of the p_z band, as we analyzed them for the Sb linear chain. In the picture appropriate for a single unit cell we found that the lower part of the p_z band is bonding (at Z), the middle is nearly nonbonding (at $k = \pi/2a$) and the upper part is antibonding (at Γ). Upon folding, these points come at Γ, Z, and Γ of the doubled unit cell (halved Brillouin zone), respectively (see Figures 14a and 16a). Examination of the N–N crystal orbital overlap population (COOP) curve (Figure 17a) indicates that at the aforementioned three points (indeed throughout the p_z band) the N–N interaction is *antibonding*. Something has changed from the simple picture that worked so well for Sb.

In deriving the band structure for a linear Sb chain we assumed that no s-p mixing occurs. Our calculations actually show that some mixing occurs even for Sb. But since its extent was not large we could safely ignore it. This is not so for the N case; the s-p mixing is in fact so large that an avoided crossing occurs between s and p_z bands. The "p_z" band has purely p_z character at Γ and purely s character at Z.[88] The s band contribution to the p_z band of nitrogen is 30% (averaged over the Brillouin zone), compared to 18% for the Sb case.

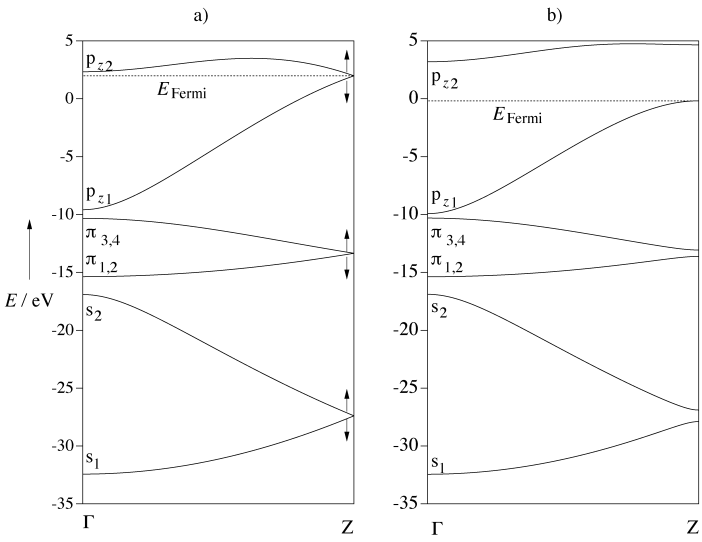

Figure 16. The band structure of a 1D N_2 chain with a) uniform N–N separations of 1.50 Å, b) alternating N–N distances of 1.45 and 1.55 Å.

As a result of the strong s-p mixing, the "p_z" band is greatly destabilized throughout the whole Brillouin zone and is strongly N–N antibonding. One would expect intuitively that a higher energy band would be more stabilized by a Peierls distortion than a lower energy band, given equal changes in the overlaps during the distortion. We provide elsewhere[92]

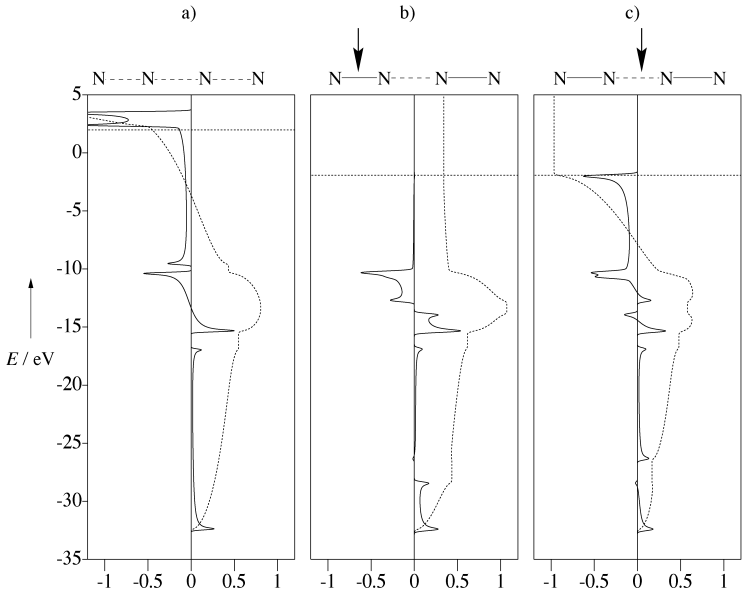

Figure 17. COOP curves (solid lines) and their integrations (dashed lines) between the nearest neighbor nitrogen atoms in an ideal chain (a) in a distorted chain with short (b) and long N–N distances (c); the magnitude Δ of the distortion is 0.1 Å.

the formal basis for this argument with the help of molecular perturbation theory.[93, 94] A word of caution is in order here. Although s-p mixing destabilizes the "p_z" band, and, therefore, creates favorable conditions for the Peierls distortion, the Peierls distortion itself is not driven by s-p mixing. Our calculations indicate that, on the contrary, the magnitude of the s-p mixing diminishes during the Peierls distortion process.

We calculated the effect of a pairing distortion of a relatively small magnitude ($\Delta = 0.10$ Å) of an ideal N chain (Scheme 13). The band structure for an undistorted chain is

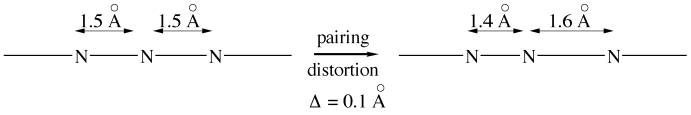

Scheme 13.

shown in Figure 16a. The stabilization (3.47 eV per N_2 unit cell) is an order of magnitude higher than for the corresponding distortion in the Sb chain (0.18 eV per Sb_2 unit cell). This relatively small distortion is sufficient to make the lower (filled) "p_z" band (p_{z1} in Figures 16a and b) lose its strongly antibonding character. The p_{z1} band rehybridizes (namely, the extent of s-p mixing in it is changed) in such a way that the sp hybrid lobes grow pointing outward from the new N_2 pairs. This significantly reduces the intra-pair N–N negative overlap population (Figure 17b) more than compensating for the incr;ease in the inter-pair N–N overlap population (Figure 17c). The effects are very clear in the integrated COOP curves.

To clarify further the important role of s-p mixing for the N-chain distortion we carried out a numerical experiment, in which the overlaps between the s and p orbitals of N were simply set to zero (that is, there is no s-p mixing). As may be inferred from Figure 15, this has an overwhelming effect on the stability of an ideal N chain—the pairing distortion becomes strongly disfavored! We trace this unexpected result to the significant stabilization of the p_z band in the ideal N chain. The midpoint of the p_z band (or point Z in Figure 16a) drops below the corresponding point of the π bands, thus making the latter the highest occupied band at Z. Since both bonding and anti-
bonding branches of the π bands near Z are filled (see Figure 16a), the pairing distortion raises the total energy. Clearly, s-p mixing plays an exceptionally important role in the tendency of a linear N chain to undergo a Peierls distortion.

4.6. The Rationale for Variable s-p Mixing

It is apparent that pairing is much more favorable for an N^{2-} chain than for a Sb^{2-} chain (see Figure 15). Actually, neither N^{2-} chains nor N_2^{4-} pairs have yet been found in extended structures, only isolated nitride (N^{3-}) and molecular azide (N_3^-) units. Nevertheless, the theoretically derived trend makes sense; the tendency to pair or, more generally, undergo a Peierls distortion is much more pronounced at the top of any group in the Periodic Table. This observation is important, and is essentially tied to the periodic tendency to undergo a metal–insulator transition. We trace the effect to a substantially greater s-p mixing in the lighter elements in the group.

The last question to be answered in this subsection is more fundamental: *Why* is s-p mixing greater for the lighter elements? From the point of view of first-order molecular perturbation theory two factors influence the strength of an interaction, which is generally proportional to $S_{ij}^2/\Delta E_{ij}$ (S_{ij} is the overlap and ΔE_{ij} is the energy difference between two orbitals i and j).[93, 94] The energy difference between the s and p orbitals of the heavier elements is smaller then for the lighter elements.[95] Therefore, the energy argument would actually suggest greater s-p mixing for the heavier elements. However, the overlap term completely reverses this tendency. As a result of the electron–electron interactions, the poorly screened s orbitals become more contracted[95] down a group in the Periodic Table (Table 3). This contraction of s orbitals is further enhanced by relativistic effects for the heavier elements, which have been discussed by several authors.[96, 14, 80]

Table 3. Average radii and one-electron orbital energies for elements of Group 5 from Hartree–Fock calculations.[95]

	N	P	As	Sb	Bi
$\langle r_s \rangle$ [Å]	0.70	0.91	1.07	1.26	1.34
$\langle r_p \rangle$ [Å]	0.75	1.09	1.33	1.53	1.64
E_s [eV]	−25.72	−18.96	−18.64	−15.84	−15.00
E_p [eV]	−15.44	−10.66	−10.06	−9.10	−8.71

Consequently, as one goes down a group the s-s and s-p overlaps are much reduced and the s orbitals in general play a lesser role in chemical bonding. As a reviewer pointed out, there are other ways to analyze this problem, such as in terms of polarizability or effective charge. The reader is referred to the important paper of Kutzelnigg for a deeper discussion.[97]

In summary, strong s-p mixing for a N^{2-} chain destabilizes greatly the filled "p_z" band, making a Peierls distortion inevitable. On the other hand, the tendency of an Sb^{2-} chain to undergo a pairing distortion is much less pronounced, which allows the existence of metallic phases that do not do not undergo a Peierls distortion. Gradual dimunition of s-p mixing from N to Bi leads to the enhancement of their potential metallic properties. We think this is a useful, if not complete, way to think about the "diagonal line" separating metals from nonmetals in the right part of the Periodic Table. To deal reliably and quantitavely with the question of the metal/nonmetal transition the effect of electron–electron interactions on the Peierls distortion has to be examined.

In the last two sections we have described only Peierls distortion of one-dimensional N and Sb chains. For higher dimensional sublattices incomplete Fermi nesting might occur, as has been recently shown by D.-K. Seo and R. Hoffmann for Group 5 elemental structures.[98]

Having described bonding in a linear 1D Sb chain, we are now ready to generalize our ideas to higher dimensions.

5. Theory: Hypervalent Bonding in Two Dimensions

5.1. Electron Counting in a Square Lattice

There are several ways that we might assemble a square lattice. One can think of a square lattice as a 2D collection of individual atoms and simply derive its crystal orbitals. An alternative view is to think of a square lattice as an array of 1D chains (Scheme 14). Since we discussed the band structure of an 1D chain in detail above, let's first use the latter approach.

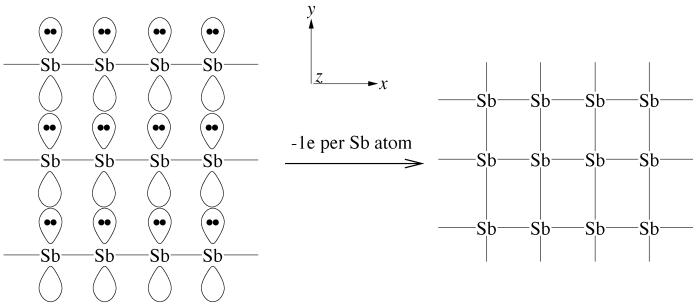

Scheme 14.

We assemble a square Sb sheet in the *xy* plane, positioning component 1D linear chains along the x direction (Figure 18a). There are three lone pairs per Sb atom in a linear Sb chain, localized now in the s, p_y, and p_z orbitals. If isolated Sb^{2-} chains are brought up to each other in the *xy* plane (see Scheme 14), repulsion would clearly develop between the p_y lone pairs of the chains.

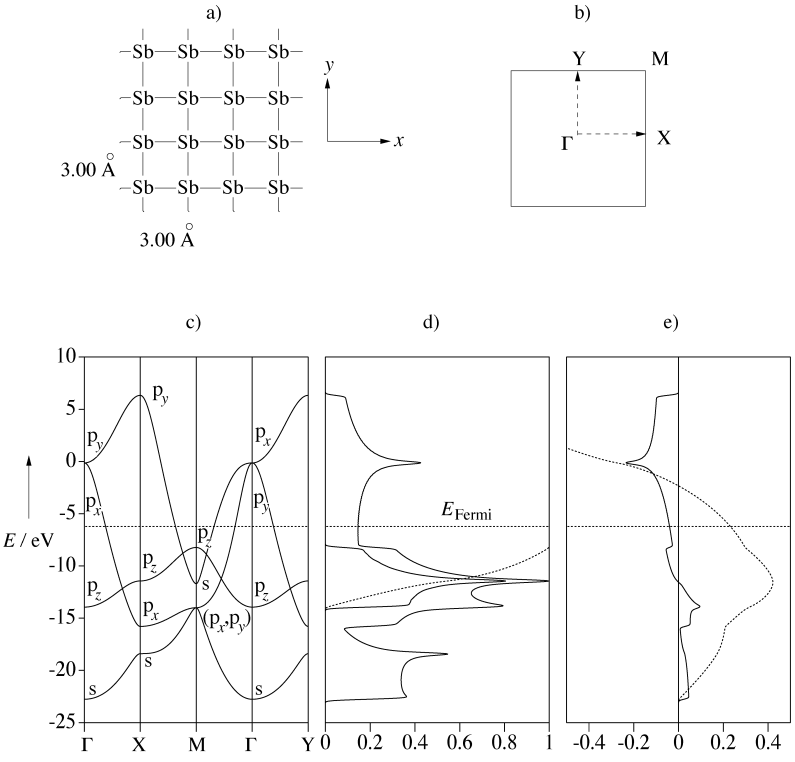

Figure 18. a) Square sheet of Sb, b) Brillouin zone, c) band structure of the square Sb^- sheet, d) p_z contribution to the total DOS, e) nearest neighbor Sb–Sb COOP (solid line) and its integration curve (dashed line).

How can we make the interactions of 1D chains in Scheme 14 attractive? Faced with the same question about two approaching CH_3^- fragments an organic chemist would propose a clear solution: to remove one electron from each CH_3^- lone pair, which in turn would lead to the formation of the stable C–C bond in ethane. We may do the same with the linear Sb chains: remove one electron from each p_y lone pair. Bonding interactions then develop in the *y* direction, much as they exist in the *x* direction (in a perfect square lattice the *x* and *y* directions are equivalent). Since we started with seven electrons per atom in the linear chain, the optimal electron count for the square lattice should be six electrons per atom.

Now we discuss the same idea from the point of view of band structure theory. A square Sb lattice has a square reciprocal unit cell as depicted in Figure 18b. The special points in the first Brillouin zone are Γ, X, Y, and M. The band structure and crystal orbitals for a generic square lattice have been discussed many times in the literature.[17, 19] We have recently described in detail the crystal orbitals for an Sb square lattice.[99] Here we discuss very briefly the band structure of a square Sb^- sheet.

In our discussion of a 1D Sb^{2-} chain in Section 4.2 we found it possible to neglect the influence of π bonding in the system. For a square lattice this assumption is still valid—the p_z band (perpendicular to the sheet) in Figure 18c is relatively narrow and completely filled (Figure 18d). In-plane π interactions of p_x and p_y bands are also small compared to σ interactions. For example, the dispersion of the σ-interacting p_x band along the Γ – X symmetry line is much wider than that of the π-interacting p_y band along the same symmetry line. Our other assumption was the relative unimportance of s-p mixing for heavy elements. For a square lattice, s-p mixing is strongest at M (Figure 18c), where an avoided crossing occurs between the s band and doubly degenerate p_x and p_y bands. Still, s-p mixing for a square Sb lattice is much less than what is found for a square N lattice. Our two major qualitative assumptions continue to hold for a square Sb lattice.

The nearest-neighbor Sb–Sb COOP curves (Figure 18e) shed further light on the bonding in the square sheet. The overlap population generated by the antibonding part of the π band cancels out its bonding part. The COOP near the Fermi level is weakly antibonding, although our qualitative picture implies that it should be nonbonding. The reason for this discrepancy was already discussed for an 1D chain—some s-p mixing does occur. The same part of the band structure for an N^{2-} chain was *strongly* antibonding (see Figure 17a).

As for the 1D chain, we need to make a connection between a square lattice and various classical geometries for the same electron count (six electrons per Sb atom). One way to do this is to examine possible pathways for a Peierls distortion of a square sheet, a subject that we take up in the next section.

5.2. Peierls Distortion of a Square Sb^- Lattice—Classical and Semiclassical Geometries

For a 1D Sb^{2-} chain, the Peierls distortion viewpoint led unambiguously (if weakly) to the formation of classical Sb_2^{4-} pairs. The possibilities for Peierls distortion of a square net are much richer. One systematic way to study them is to use the Fermi surface nesting approach.[20–22, 89–91] In this method the reciprocal lattice vector that maximally nests the Fermi surface is likely to lead to charge density waves (CDW) with the same wavevector. These most often manifest themselves in static distortions of the lattice. Since the Fermi surface topology depends clearly on the number of electrons, the nesting vector is dependent on the electron count. An elegant experimental and theoretical study of this dependency for mixed Sb and Te square lattice has been carried out by Lee and co-workers,[20] and the groups of Whangbo and Canadell have shown the utility of the Fermi surface nesting formalism.[89–91] Our group has used a different approach to study possible distortions of a square lattice.[19] Here we outline qualitatively the main results of these studies and introduce a new hypothetical distortion to ladder chains.

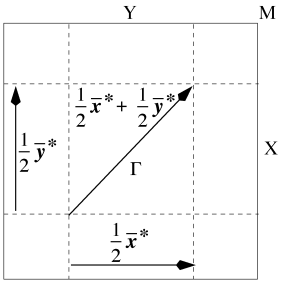

Scheme 15.

For a qualitative discussion we are again going to ignore π interactions and s-p mixing. The Fermi surface of an Sb^- square array is then particularly simple (Scheme 15). We can think of this Fermi surface as a superposition of two one dimensional Fermi surfaces for the p_x and p_y bands. As one may see from Scheme 15, there are several reciprocal vectors that nest the Fermi surface. First consider the nesting by the $\frac{1}{2}\bar{x}^*$ vector. This leads to a pairing distortion in the x direction in real space and has no effect on the y direction. The structural consequence is that 1D ladder chains emerge (Figure 19a). Since a Peierls distortion does not alter the electron count, an electron count for these ladders is also six electrons per atom (the same as for a square lattice). Following a different line of reasoning, we proposed an electron count of six electrons per atom for a ladder structure when discussing the $FeSb_2$ crystal structure. It is encouraging that our model of bonding in extended linear networks is internally consistent.

The 1D ladders that we have obtained are classically bonded in the x direction but are still hypervalent in the y direction. If the ladders become isolated from each other, then a new Peierls distortion may occur in the direction of the chain propagation (nesting vector $\frac{1}{2}\bar{y}^*$ in Scheme 15) leading to isolated Sb_4^{4-} squares (Figure 19b). The electron count for noninteracting squares corresponds to completion of an octet around each Sb, namely, a classical structure. One can also obtain isolated squares from a square sheet by a single Peierls distortion with the nested vector $\frac{1}{2}\bar{x}^*+\frac{1}{2}\bar{y}^*$ (see Scheme 15). It turns out that this unique vector in the reciprocal space does not uniquely determine the arrangement of atoms in the real space; it only tells us that there occurs unit cell doubling in both the x and y directions. However, the movement of individual atoms within the quadrupled unit cell remains uncertain.

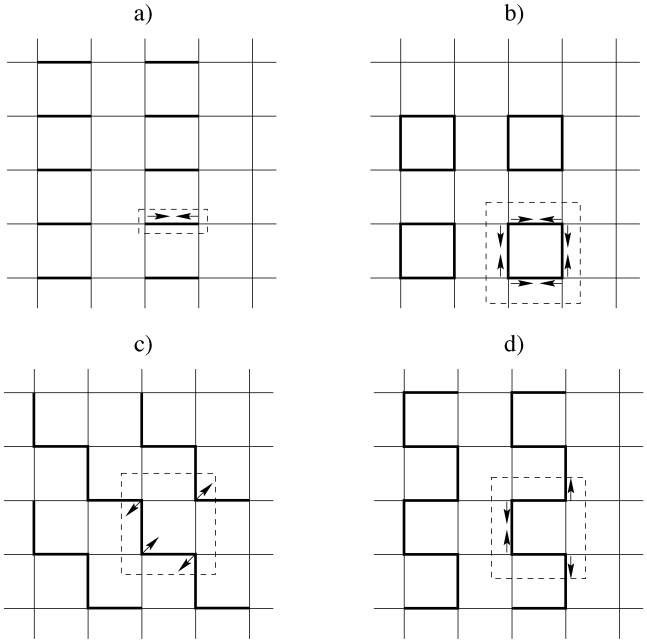

Figure 19. a) Pairing distortion in the x direction ($\frac{1}{2}\bar{x}^*$) leading to laddertype substructures; b) pairing distortions in both the x and y directions ($\frac{1}{2}\bar{x}^*+\frac{1}{2}\bar{y}^*$) resulting in squares; c) zig-zag chain formation ($\frac{1}{2}\bar{x}^*+\frac{1}{2}\bar{y}^*$); d) another distortion corresponding to $\frac{1}{2}\bar{x}^*+\frac{1}{2}\bar{y}^*$; unit cells are given in dashed lines.

In addition to isolated squares, 1D kinked chains may be formed as a result of a Peierls distortion. Two such possibilities are shown in Figures 19c and d. In the case of a zig-zag chain formation (Figure 19c) it is possible to choose an alternative unit cell with only two atoms per unit cell. In order to describe the Peierls distortion in the latter case, a non-orthogonal primitive unit cell in direct space must be used, which in turn complicates the picture in reciprocal space. A detailed treatment of orbital interactions that leads to chains of different topology is given by Tremel and Hoffmann.[19]

It is worthwhile here to introduce a general cautionary note. Sometimes words like hypervalent bonding might be taken to imply a greater stability. This may be so, but it also may well not be so. Consider for instance the salutary and classical example of I_3^-. In the gas phase the molecule is symmetrical. But in the solid state, depending on the countercation, a multitude of geometries is known, which spans pretty much the range between noninteracting $I^- + I_2$ and symmetrical I_3^-. When we get more structures, with linear chains and square nets, we expect to see a range of structures and distances "around" these symmetrical archetypes.

6. Theory: Other Topologies

6.1. Electron Counting in a Simple Cubic Lattice

In Section 5.1 we demonstrated in detail the transition from a one-dimensional chain to a square lattice. The development

of the simple cubic Sb band structure proceeds in an analogous way. The only remaining lone-pair p_z orbitals for the square Sb^- lattice (see coordinate system in scheme 14) interact repulsively when square sheets are brought together to form a cubic lattice. Therefore, as we argued before, one electron should be removed from each p_z lone pair, so bonding interactions can develop in the z direction. If a square sheet had initially six electrons per Sb, this line of reasoning leads to five electrons per Sb in a stable cubic network.

There are not that many compounds which contain formally neutral Sb atoms (five electrons per Sb atom). One of the best known examples, elemental Sb, can be made cubic under high pressure[45] (a similar high-pressure phase is known for Bi[100]). A metastable cubic phase can also be synthesized by quenching from liquid and vapor.[46] Under ambient conditions elemental Sb takes on an As-type structure—three-connected sheets stacked on top of each other in such a way (see Figure 5) that a compression along the stacked direction would result in the formation of a cubic lattice. Turning the reasoning around, one can think of an elemental Sb sheetlike structure as derived from a simple cubic lattice through a Peierls distortion (Figure 20) corresponding to reciprocal nesting vector $\frac{1}{2}\,\bar{x}^* + \frac{1}{2}\,\bar{y}^* + \frac{1}{2}\,\bar{z}^*$.[47] Notice the similarity between Figures 19c and 20.

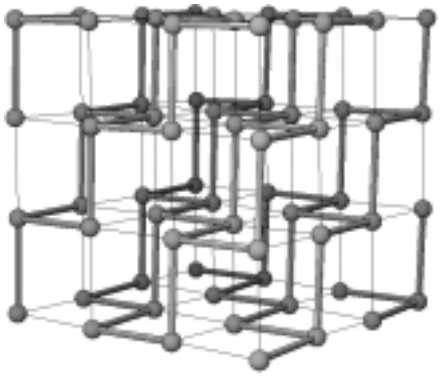

Figure 20. Peierls distortion pathway from a cubic lattice to an As-type three-connected sheet structure (thick lines).

This is hardly the only deformation available to the system.[47] One can come up with many other Peierls distortions of a simple cubic lattice, ones which would lead to classical (for example, kinked sheets) and semiclassical (for example, doubled square sheets) networks.

An interesting problem is posed for us by Po, which has six electrons per atom. This is the archetype, indeed the only element to assume a simple cubic structure under ambient conditions. What might be the source of the seeming contradiction with our argument for an electron count of five electrons per atom in a cubic lattice? The sixth electron of Po adds one third of an electron to each p_x, p_y, and p_z bands, and this might not be enough to destroy Po–Po bonding. Another reason might be the existence of strong relativistic effects that we did not explicitly consider in our derivations. Strong spin–orbit coupling makes $p_{1/2}$ atomic orbitals significantly contracted compared to $p_{3/2}$ orbitals, which in turn changes the bonding patterns in the crystal.[80] The electron counting scheme that we have discussed so far may need to be modified for elements which have pronounced relativistic spin–orbit coupling.

von Schnering has brought to our attention the fact that many binary compounds with an average valence electron count of five undergo high-temperature or pressure transitions to "more symmetrical" structures with cubic coordination. The evolution of structural types is GeS → TlI → NaCl → CsCl.[101–104]

We have considered so far a linear 1D chain, a square lattice, and a simple cubic lattice. The last topology that we examine is a 1D Sb_3 strip, which we can imagine as being cut out from a square lattice.

6.2. Extended Networks Built from Finite Hypervalent Linear Chains

There are a number of structures where an aufbau based on finite hypervalent linear chains can lead to greater insight into their electronic structure. For instance, when two linear three-membered linear chains, which were discussed earlier, share a central atom, then a square-planar coordination of the central atom results. Square-planar units can be further condensed into a 1D ribbon of vertex-sharing squares. The importance of this construction is based on the persistent nature of the three-center four-electrons bonds underlying the extended network, even though these localized three-center orbitals broaden into bands by interaction with each other and other orbitals. Consequently, electron counting rules for such extended structures may be derived in a few easy steps starting with known electron counts for finite linear chains. This point is illustrated by the following examples.

One dimensional Sb strips of various width are found in several binary and ternary Sb phases.[71, 105, 106] For example, 1D Sb strips of slightly distorted vertex-sharing rhombi comprise an isolated part of the Sb subnetwork in $La_{12}Mn_2Sb_{30}$.[71] One can imagine these strips (Scheme 16a)

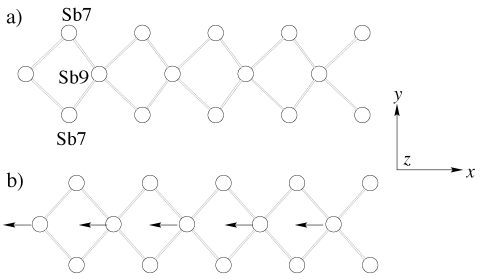

Scheme 16.

as derived from more-symmetrical undistorted strips (Scheme 16b) through a simple sliding distortion of central atoms.

What is the optimal electron count for a strip of vertex-sharing squares? The central Sb atoms in the strips (Scheme 16b) are located in a square-planar environment, which is unusual for classical compounds of main-group elements. Therefore, as a starting molecular model we choose square-planar hypervalent XeF_4 (Scheme 17a, the lines here

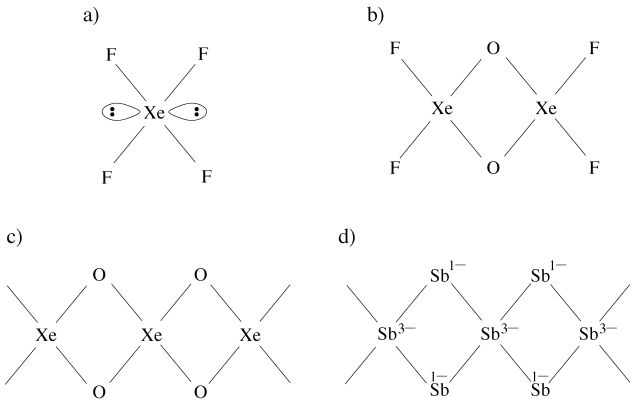

Scheme 17.

are not classical electron pair bonds, just connectivities). In this molecule the Xe atom is hypervalent while F atoms are classical (an octet can be completed around each F atom). If one wants to build a dimer out of XeF_4, one has to replace bridging F atoms by O atoms in order to preserve their classical electron count (Scheme 17b). In a similar manner, if one continues to build a trimer, a tetramer, oligomer, polymer, all the bridging F atoms have to be replaced by oxygen atoms. Therefore, a hypothetical XeO_2 polymer (Scheme 17c) has classical O atoms and hypervalent Xe atoms (12 electrons per Xe atom). The electron count in extended XeO_2 is $8+2\times6=20$ electrons per unit cell. A neutral Sb_3 strip contains only 15 electrons per unit cell, which necessitates an addition of a -5 charge to the unit cell.

An important point must be made about "real" and formal charges, and the way the latter are used in this work. To define theoretically a charge on an atom or a fragment one must choose a wavefunction (namely, the degree of approximation in computing one), and a way of analyzing that wavefunction (Mulliken population analysis, Bader partitioning, etc.).

In our work we use formal charges. As in organometallic chemistry, these are not unambiguous (should C_5H_5 carry a -1 or 0 charge? Should a halide be counted as anionic or neutral?). What is unambiguous is the total electron count, no matter whether one starts from an initial ionic or neutral (covalent) assignment. Thus Xe has ten electrons around it in XeF_2, whether one begins with Xe^{2+} and $2F^-$, or with Xe^0 and $2F^0$.

There is still another way of assigning charges, which has a history in the three-center bonding field, and this is partway between a starting point based on an ionic (or covalent) formal charge and one based on a "real" electron distribution. A Hückel analysis of the distribution of the four electrons in the three-center system puts 1.5 electrons on the terminal and 1.0 on the central atom. Such an assignment would lead to Xe^+ and two $F^{1/2-}$ centers in XeF_2.

In the spirit of Zintl–Klemm formalism, throughout this paper we will use only formal charges and a "covalent" formalism. We do this with full awareness of, and respect for, the other variants prevalent in the literature. To be specific, we will look at XeF_2 as formally being derived from a Xe atom and two F atoms. We will also look at the "isoelectronic" Sb_3^{7-} linear molecule as being made up from formal Sb^{2-} end ions and a central Sb^{3-} ion.

Returning to the Sb_3^{5-} strip (Scheme 17d), its electronic structure is directly related to molecular XeF_4. These considerations are supported by detailed band calculations. As we mentioned above, a sliding distortion is observed in these structures. This deformation can be analyzed as a solid-state analogue of a second-order Jahn–Teller distortion. The details are given in our ref. [99].

The Sb_3 strip is the most narrow one that can be cut out from a square lattice. Wider Sb strips are found in the binary Zr–Sb phases.[105–107] The square two-dimensional Te defect lattice in the binary Cs_3Te_{22} phase can also be thought of as being comprised from finite (five-membered) linear chains.[108, 109] Electron counting rules for these ribbons and sheets will be published elsewhere.[110]

7. Navigating between Classical and Hypervalent Structures: Oxidation versus Peierls Distortion

It is time to face a fundamental question: that of the interrelationship of dimensionality and deformation. The electron counting regularities we derived *did not* emerge from a principle of maximized bonding. Instead they assumed a certain electron count, and traced the bonding and geometrical consequences. For instance, a linear geometry is much favored over the kinked classical geometry for a linear Sb chain with seven electrons per atom (Sb^{2-}). For this electron count, the only classical alternative to the linear hypervalent chain consists of isolated Sb_2^{4-} pairs—the result of the Peierls distortion of the linear chain (Figure 21).

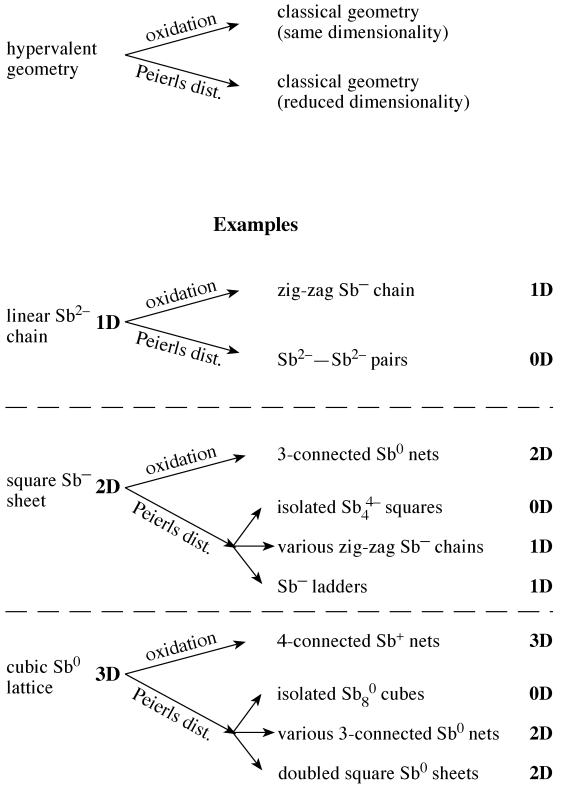

Figure 21. A schematic diagram showing relationships between electron counting, the Peierls distortion, and the dimensionality.

However, if we imagine the anion chain in an ionic atmosphere of cations whose number can vary, the possibility of a change in electron count of the main group sublattice opens up. When Sb^{2-} is oxidized to Sb^{-}, the classical kinked (zig-zag or helical) chain is much preferred over the linear chain.

In general, we have an important principle: if one wants to transform a hypervalent structure into a classical one with the same lattice dimensionality, one has to oxidize the hypervalent structure. The Peierls distortion, which conserves the electron count, transforms the hypervalent structures into classical or semiclassical ones with the lattice dimensionality reduced. Figure 21 summarizes and exemplifies this principle.

We examined briefly in Section 5.2 the Peierls-distortion pathways of a square Sb^{-} lattice (see Figure 19). The resulting classical isolated squares, zig-zag chains, and semiclassical ladders retain the original electron count of six electrons per atom (Figure 21), while their dimensionality is reduced from two to one or zero. Oxidation of the square Sb^{-} sheet can lead to a three-connected classical "As-type" Sb^{0} net with the same dimensionality (2D). A possible mechanism for this transformation might include an intermediate hexagonal net, which then puckers (Figure 22). The transformation of a square lattice into a hexagonal net has been described by Burdett and Lee.[47] We believe that for the electron count of five electrons per atom the As-type net is much more stable than the square net. Nevertheless, kinetic barriers might prevent this transformation, hence creating a metastable square net.

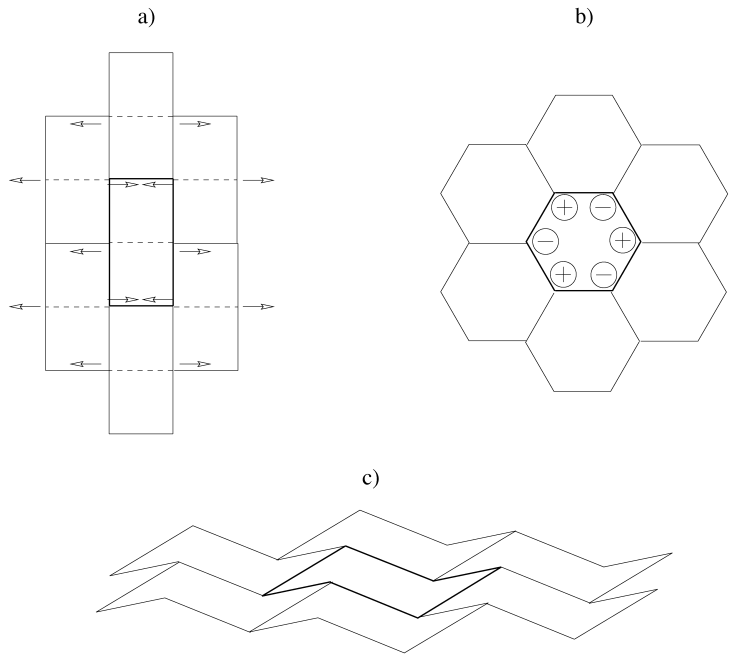

Figure 22. A hypothetical pathway connecting a square lattice into an As-type net. a) Arrows indicate schematically the atom motions and show how a square lattice might transform into a hexagonal network; b) plus and minus indicate the out-of-plane motion of atoms of the As-type net (c).

Oxidation of the cubic Sb^{0} lattice might result in a four-connected Sb^{+} net, with the preservation of the original dimensionality. A hypothetical two-step pathway for the transformation of a simple cubic lattice to a diamond structure is given in Figure 23. It begins by orienting the cubic lattice along (111) and looking at it as a repetition of three double layers (A, A′), (B, B′), and (C, C′; see Figure 23a). In the first step of the transformation, the double layers flatten, creating tetrahedral angles within the sheets and separate from each other (Figure 23b). Next, the double layers are envisioned as sliding on top of each other, adjusting their vertical coordinates so as to create the diamond lattice (Figure 23c). Since extensive bond breaking and bond formation occur during this transformation (six-connected network changes into four-connected one), kinetic barriers may preclude the formation of the diamond lattice.

The Peierls distortion of a cubic lattice reduces its dimensionality from three to two, one, or zero. One may use the schematic (and incomplete) diagram of Figure 21 as an approximate guide for navigating between the hypervalent and classical networks.

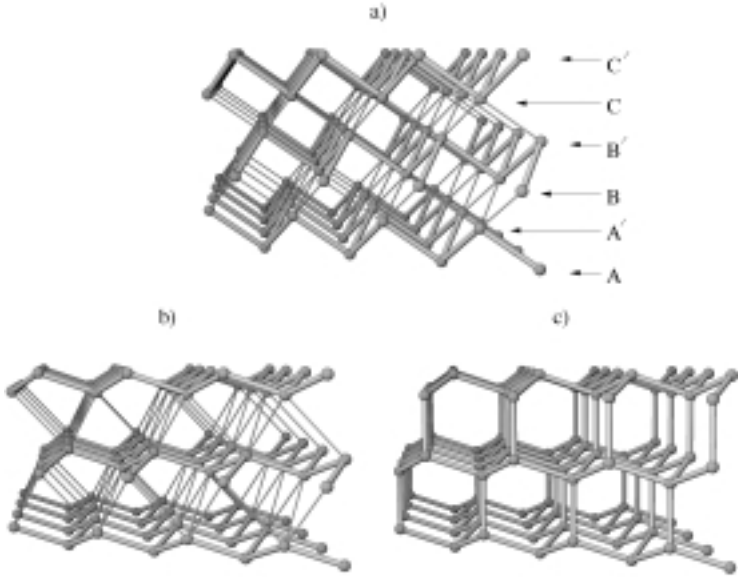

Figure 23. A hypothetical pathway transforming a simple cubic lattice into a diamond lattice. a) The simple cubic lattice represented as a repeated pattern of six layers: A, A′, B, B′, C, C′; b) As-type 3-connected sheets are created with tetrahedral angles; c) diamond lattice.

8. Theory: Summary of the Preceding Sections

In the discussion above we derived optimal electron counting for different hypervalent geometries. We demonstrated that a linear Sb chain is relatively stable with seven electrons per atom, a square Sb sheet with six electrons per atom, and a simple cubic Sb network with five electrons per atom. The Peierls distortion of a square sheet may lead to semiclassical ladders with the same electron count of six electrons per atom. The analogous distortion of a cubic lattice might lead to doubled square sheets, with an electron count of five electrons per atom. By carefully examining the Peierls distortion pathways of a cubic lattice or a square sheet, one

may derive electron counting schemes for many of the resulting classical and semiclassical lattices.

Another topology we considered is that of Sb_3 strips cut from a square lattice. By making a connection to molecular hypervalent XeF_4 we were able to derive an electron count of 20 electrons per unit cell (Sb_3^{5-}). This sublattice (and other strips) are subject to a potential second-order Jahn–Teller distortion, which leads to more stable, classical isolated Sb_3^{5-} units.[99]

At the end we showed the connection between electron counting, the Peierls distortion, and the dimensionality. The electron counting scheme that we have suggested for electron-rich networks is only an approximation, a rough guide to the beautifully complicated reality of antimonide framework bonding. One reason for the complexity is the often metallic character of these networks—fractional filling of the bands is common. The number of electrons that we derived for each network indicates only the most likely number of electrons that can be expected for that particular network. Our derivations apply to the heavier late main group elements, where π bonding and s-p mixing are not important. For the lighter elements where s-p mixing is important, the Peierls distorted classical structures are much more favorable, which is why linear metallic 1D N^{2-} chains do not exist.

The electron counting considerations that we propose can be used as a kind of aufbau, the foundation, for more elaborate analysis. In the following section we demonstrate how Sb–Sb bonding in the fairly complicated alloy $La_{12}Mn_2Sb_{30}$[71] can be understood with the help of these simple electron counting schemes. The applicability of the proposed electron counting principles to other main group elements will be examined next.

9. Building Complex Networks from Low-Dimensional Sb Sheets and Strips

In many cases a given complex structure can be theoretically broken down into simpler pieces, studied as such, and reassembled back. In this "retrotheoretical analysis"[99] the Zintl–Klemm electron counting scheme is indispensable. The electron counting schemes developed in this review make the nonclassical and semiclassical electron-rich multicenter networks new building blocks for such a "retrotheoretical analysis". We exemplify this process in this section, where we analyze qualitatively the Sb–Sb bonding in the $La_{12}Mn_2Sb_{30}$ alloy. For a more complete discussion of the bonding in this structure we refer readers to the original paper.[99]

$La_{12}Mn_2Sb_{30}$ (Figure 24) is a member of a series of new ternary compounds ($RE_{12}M_2Sb_{30}$) reported recently by Rogl, Cordier, and co-workers.[71] Magnetic measurements indicate[71] that rare earth metals are tripositive in all compounds, and the Mn ions are dipositive in $Ce_{12}Mn_2Sb_{30}$. If one assumes that Mn is dipositive also in $La_{12}Mn_2Sb_{30}$, then the number of electrons formally transferred to the Sb network is unambiguously calculated as $12 \times 3 + 2 \times 2 = 40$.

The Sb sublattice of $La_{12}Mn_2Sb_{30}$ crystal structure consists of no less than three noninteracting sublattices—a 3D Sb_{20} network (Figure 25b), 1D Sb_3 strips (see Scheme 16a), and

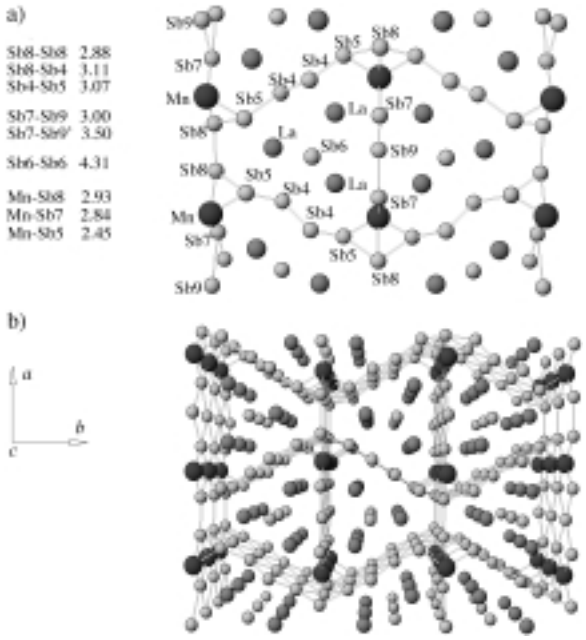

Figure 24. a) Unit cell of $La_{12}Mn_2Sb_{30}$; b) perspective view of the crystal structure of $La_{12}Mn_2Sb_{30}$; Sb = small spheres; La = medium size spheres; Mn = large dark spheres (half-occupied).

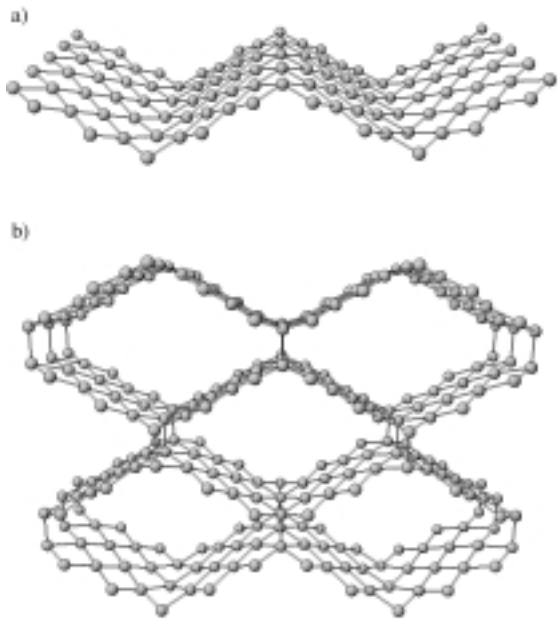

Figure 25. a) A 2D kinked sheet of Sb atoms; b) 3D Sb_{20} substructure.

isolated Sb atoms. By taking into account the crystal site multiplicities, the Sb_{30} substructure can be written as $Sb_{20}^{3D\,net}Sb_6^{1D\,strip}Sb_4^{atom}$. By taking the retrotheoretical approach one step further, we break down the three-dimensional Sb_{20} network into 2D kinked sheets (Figure 25a). The latter sheets can be hypothetically flattened into a square lattice. The stages of this retrotheoretical analysis are indicated in Figure 26.

The simple building blocks that we have to analyze are 1) isolated Sb atoms, 2) 1D Sb_3 strips, and 3) square Sb sheets. According to the Zintl–Klemm concept we assign a -3 charge to isolated Sb atoms, which then contribute a -12

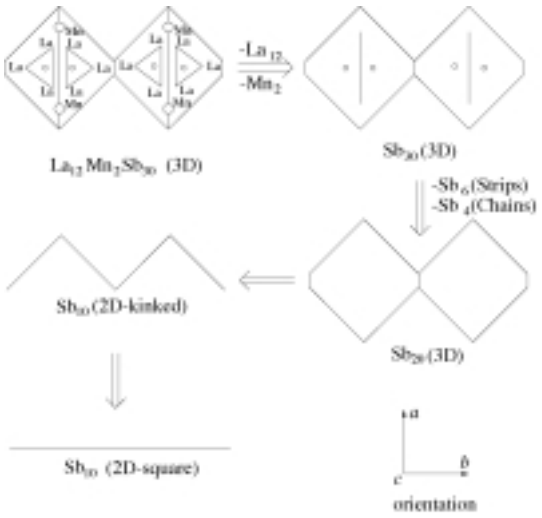

Figure 26. Schematic representation of "retrotheoretical" disassembly of $La_{12}Mn_2Sb_{30}$. A side view parallel to the *c* axis is shown.

charge to the full Sb_{30} network. The 1D Sb_3 strip (Scheme 16) should carry a -5 charge, following our earlier analysis. Since there are two such units in the unit cell of $La_{12}Mn_2Sb_{30}$, they contribute a -10 charge.

We begin by assigning a -1 charge to each Sb atom in a square lattice. The sheet depicted in Figure 25a can be derived from a square Sb sheet by kinking at every fifth diagonal line. A detailed analysis shows that this kinking leads to s-p hybridization and localization of the π orbitals at the kinks, but otherwise does not significantly influence the electronic structure of the square sheet.[99] The electron count remains at six electrons per Sb atom for the kinked sheet. The stacking of the kinked sheets into a three-dimensional network (Figure 25b) would lead to repulsion between neighboring sheets as a consequence of the interaction of lone pairs (Scheme 18). To make the interaction between two neighboring sheets bonding, one electron has to be removed from each Sb atom participating in intersheet linkage (a fifth of the total number of Sb atoms). This translates into the removal of $\frac{1}{5} \times 20 = 4$ electrons from the Sb_{20}^{20-} unit cell, making it Sb_{20}^{16-}.

The contributions of the isolated Sb atoms, 1D Sb strips, and 3D Sb subnetwork to the total Sb charge are then -12, -10, and -16, respectively. The overall -38 charge on the Sb_{30} substructure falls two electrons short of the -40 charge donated by the La and Mn ions. The disposition of the last two electrons (from a total of 200 electrons in the unit cell) is a matter of some interest, and is no doubt related to the conducting properties of the material. The bonding around the Mn center and the fate of the two electrons are discussed in our original paper.[99]

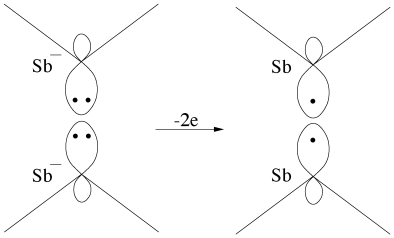

Scheme 18.

10. Hypervalent Linear Chains and their Derivatives Made of Other Heavy Main Group Elements

The hypervalent bonding patterns in Sb compounds conform surprisingly well to our electron counting scheme. In this section we look at hypervalent linear chains of some other heavy main group elements, mainly Te, Se, and Sn. A selective compilation of binary and ternary phases containing linear chains or their derivatives is given in Table 4.

First, we discuss the linear chains in the compounds where the assignment of the formal oxidation states to cations is more or less straightforward, then we take up more complicated cases. We demonstrate in this section that the electron count of seven electrons per atom in the linear chain serves as a good starting point for the most of these compounds, and that the deviations from this electron count are observed in a rather narrow range. In the process we make sense, we believe, of some pretty incredible structures.

10.1. Simpler Binary Phases

Simple linear Te chains are found in the CuTe crystal structure.[111, 112] The Te–Te bond length between uniformly

Table 4. Heavy main group compounds containing linear chains.

Compound	Related Structures	Geometrical patterns
K_5Se_3, Cs_5Te_3[114]		dumbbells aligned into a linear chain
CuTe[111, 112]		linear chains
TlTe[263]		linear chains with handles
Tl_5Te_3[264]		linear chains condensed into a 3D structure
Tl_4MTe_3 (M = Sn, Pb)[115]	Tl_5Te_3	linear chains condensed into a 3D structure
Tl_9ME_6 (M = Sb, Bi; E = Se, Te)[115]	Tl_5Te_3	linear chains condensed into a 3D structure
UTe_2[118, 120]	β-$ErSe_2$	linear chains
$ErSe_2$[122]	UTe_2	linear chains
$Dy_{0.5}U_{0.5}Te_2$[121]	UTe_2, β-$ErSe_2$	linear chains
ME_3 (M = Ti, Zr, Hf; E = S, Se, Te)[123]	UTe_2	dumbbells aligned into a linear chain
α-UTe_3[265]	$ZrTe_3$	dumbbells aligned into a linear chain
MTh_2Se_6 (M = K, Rb)[125]	$ZrSe_3$	CDW-distorted linear chain
$Tl_{0.56}UTe_3$[129]	$ZrTe_3$	linear chain
$CsTh_2Te_6$[126]	$ZrTe_3$	linear chains
$M_2Th_2E_6$ (M = K, Cs; E = Se, Te)[127]	$ZrTe_3$	linear chains
$CuTh_2Te_6$[128]	$ZrTe_3$	linear chains
$CsTiUTe_5$[266]		linear chains
$Cu_{0.28}LaTe_2$[130]		linear chains
$Dy_3Cu_2Te_7$[131]		linear chains
MM'_3Te_8(M = Cs, Rb; M′ = Ce, Nd) [243]		linear chains kinked at every second atom
UTe_5[267]		linear chains kinked at every second atom

spaced Te atoms within the Te chain is 3.16 Å, a typical distance for a hypervalent Te–Te bond (3.05 Å in hypervalent Te_5^{2-} in Cs_2Te_5[113]). One associates two common oxidation states with the Cu ion, +1 and +2. We believe that the latter is improbable in this compound, since in that case Te^{2-} ions would be expected to be more than 4 Å apart from each other. An assumption of Cu^+ leads to Te^-, which is consistent with our electron counting scheme of seven electrons per atom in the linear chain.

The linear chains in K_5Se_3 and Cs_5Te_3[114] have undergone a pairing distortion, more emphasized for the former compound. The Te–Te intra-pair distance in Cs_5Te_3 is 2.81 Å, while the Te–Te inter-pair distance is 3.85 Å. In addition to Te_2 dumbbells aligned into a linear chain there exist also isolated Te atoms in this compound. Taking into account the crystal site multiplicities, the charges in Cs_5Te_3 may be assigned as $(Cs_{10})^{+10}(Te_2^{pair})^{2-}(Te_4^{atom})^{8-}$. An electron count of seven electrons per atom is reasonable for isolated Te_2 pairs as well as for Te atoms aligned into a linear chain; we have discussed this choice in some detail in Section 3.4.

Simple linear chains and their derivatives are found in the TlTe binary phase (Figure 27). In this compound some of the linear Te chains have "handles" attached to them, with each

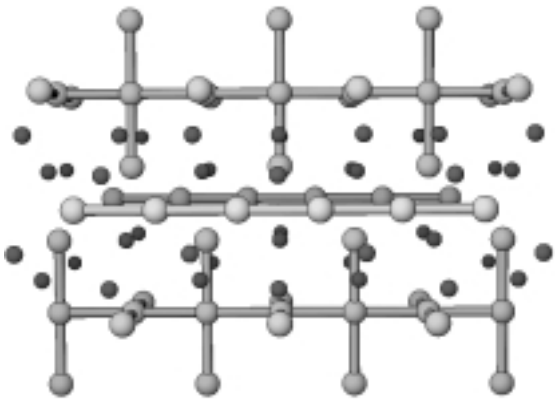

Figure 27. A perspective view of the crystal structure of TlTe. Tl = small dark spheres; Te = large light spheres.

handle oriented perpendicular to the next one. The Te–Te bond length within the chains in both simple linear chains and composite linear chains is 3.09 Å. The distance between the Te atoms in the chain and on the sidearms in the composite linear chains is 3.03 Å. This distance, although shorter than the one within the chains, is still on the hypervalent side of the range of Te–Te bond lengths.

We may use our electron counting scheme for hypervalent bonding in the solid state as a starting point for the rationalization of the stoichiometry of this compound. We begin by assigning a −1 charge to Te atoms in the simple linear chains. For the linear chains with handles we follow a two-step procedure, where we imagine the composite chain being assembled hypothetically from a simple linear chain and isolated side atoms (handles). A −1 charge should be assigned to Te atoms in an isolated linear chain. We prepare "side" Te atoms for subsequent bonding by making them also have a charge of −1, so they can contribute only one electron to bonding. Two such side Te^- ions interact with the lone pair (p_x, p_y) on the central Te atom, forming a three-center four-electron hypervalent bond (Scheme 19). We have seen this picture earlier (see Scheme 3), when discussing the bonding in

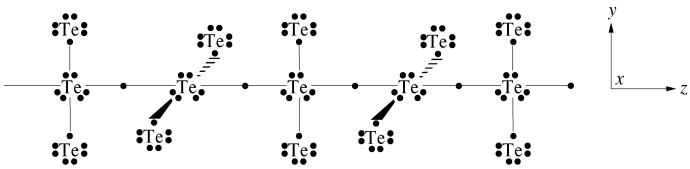

Scheme 19.

XeF_2 and I_3^- molecules. All three types of Te atoms (simple chain atoms, central atoms in the composite chain, and sidearm atoms in the composite chain) carry a −1 charge. Since Tl is commonly found monopositive, the Tl^+Te^- formulation seems to be reasonable.

10.2. The Tl_5Te_3 Binary Phase and its Ternary Derivatives

A perspective view of the Tl_4SnTe_3 crystal structure is given in Figure 28. One could perform a retrotheoretical disassembly of the beautiful and intricate $SnTe_3$ subnetwork in this

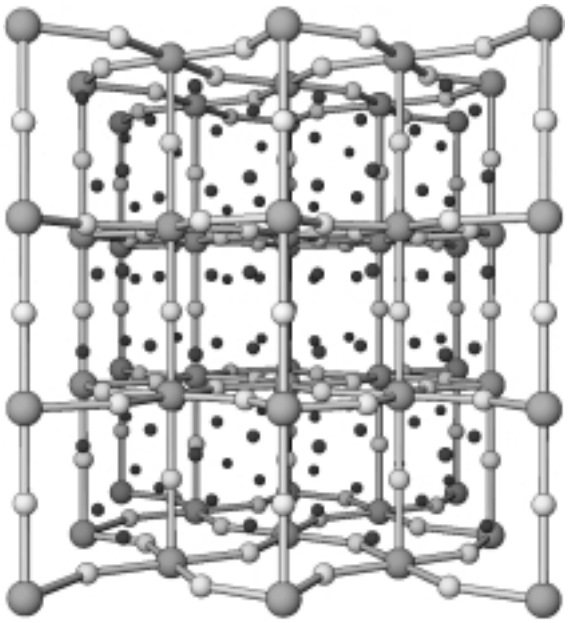

Figure 28. A perspective view of the crystal structure of Tl_4SnTe_3. Tl = small dark spheres; Te = small light spheres; Sn = large light spheres.

compound in various alternative ways. Since we are obsessed with linear chains, we view this network as linear SnTe chains connected together by bridging Te atoms (Figure 28). One could also imagine this network as being composed of vertex-sharing $SnTe_6$ octahedra, similar to the ReO_3 network. Notice that these $SnTe_6$ octahedra are then tilted with respect to each other within horizontal planes. The Sn–Te bond length within the linear chain is 3.26 Å, and between Sn atoms and sidearm

Te atoms is 3.30 Å. These bond lengths indicate hypervalent bonding between Sn and Te atoms.

We carry out the hypothetical assembly of the $SnTe_3$ network in Tl_4SnTe_3 in two distinct steps. First, we form linear SnTe chains and then we connect them with bridging Te atoms. The isolated SnTe linear chain should carry a -4 charge per SnTe unit, since the neutral SnTe unit is short by four of the fourteen electrons per two atoms needed for an ideal linear chain. Given this charge on the SnTe unit, each Sn and Te atom carries three lone pairs (s, p_x, and p_y) and a p_z chain orbital filled with only one electron (the z direction is chosen as the SnTe chain propagation axis).

We prepare the bridging Te atoms for subsequent bonding by making them neutral, which in turn provides two unpaired electrons per Te atom for bonding with the linear chains. As we have discussed for the Te chains with handles in the TlTe phase, three-center four-electron hypervalent bonds form between two side Te atoms and the p_x, p_y orbitals of the Sn atoms in the chains (Scheme 20). This reasoning leads to a -4 charge on the $SnTe_3$ unit, namely, $(SnTe)^{4-}Te_2^{bridging})^0$. To counterbalance the negative charge, the Tl atoms should be monopositive, which is a typical oxidation state for the Tl ion.

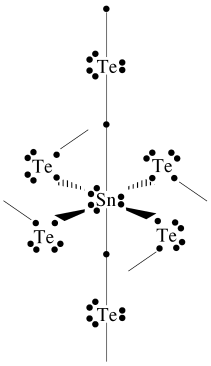

Scheme 20.

Each Sn atom in this structure plays the role of the hypervalent central atom (compare with Xe in XeF_4 or XeF_6) and participates in two linear three-center bonds. On the other hand, the sidearm Te atoms are classically bonded, since the Sn-Te-Sn angle is not linear (143°). It turns out that if all sidearm Te atoms were made linear then the structure would still keep the same electron count! Therefore, one could expect a soft potential energy surface for bending of the Sn-Te-Sn angle, which in turn might explain the large value observed for the Sn-Te-Sn angle.

A wide variety of compounds isostructural to Tl_4SnTe_3 have also been reported.[115] In the isoelectronic compound Tl_4PbTe_3 Sn is replaced by Pb, with the same geometrical features around the Te and Pb atoms as in Tl_4SnTe_3. The Tl_9BX_6 series of compounds (B = Sb or Bi, X = Se or Te) may be obtained from Tl_4SnTe_3 by first doubling its empirical formula to $Tl_8(SnSn)Te_6$, then by replacing the SnSn unit by TlSb or TlBi units, and finally by replacing all Te atoms by Se atoms if appropriate. The Sn positions in Tl_4SnTe_3 are randomly occupied by Tl and Bi or Sb in Tl_9BX_6. Notice that the substitution of SnSn by TlSb or TlBi keeps the same number of electrons in the system.

Finally, the crystal structure of parent Tl_5Te_3 may be derived from Tl_4SnTe_3 in the same way as Tl_9BX_6 was derived. Only in this case two Sn atoms are replaced by two Tl atoms, leaving the system two electrons less per $Tl_{10}Te_6$ formula unit. If one assumes that these two electrons are removed from p orbitals which are engaged in chain bonding, and given that there are two chain TlTe units in $Tl_{10}Te_6$, the electron count becomes 6.5 electrons per Tl or Te atom in the isolated chain. To learn more about the structural and physical properties of the Tl_5Te_3 family of compounds readers are referred to a recent paper by Böttcher and co-workers.[116] An alternative ionic treatment of Tl_5Te_3 and derivative phases is given by Nordell and Miller.[117]

10.3. UTe_2 and its Derivative Phases

The linear Te chains, found in the UTe_2 crystal structure, are almost uniformly spaced, with Te–Te bond lengths of 3.05 and 3.07 Å.[118, 119] The U atoms are surrounded by Te atoms in a bicapped trigonal-prismatic manner, and they are condensed in the vertical direction through Te_4 rectangular faces (Figure 29). Isolated Te atoms are also found in the UTe_2 structure, with a 1:1 ratio of chain to isolated Te atoms.

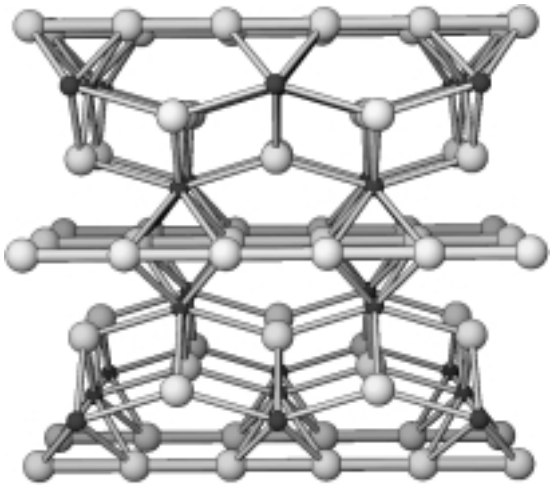
Figure 29. A perspective view of the crystal structure of UTe_2. U = small dark spheres; Te = large light spheres.

If one were to assign a $+4$ charge to U, a typical uranium oxidation state, one would force a -2 charge on both the isolated and chain Te atoms. Given the clearly bonding interactions between chain Te atoms, Beck and Dausch propose a $+(3+\delta)$ charge on the U atoms and a $-(1+\delta)$ charge on the chain Te atoms.[120] This assignment of charges is further supported by the substitution of U by trivalent Dy in UTe_2 to form $Dy_{0.5}U_{0.5}Te_2$.[121] The isostructural β-$ErTe_2$ phase was also reported.[122] By taking all these facts into account, we also concur that the oxidation state of U is much closer to $+3$ in UTe_2, and the Te atoms in the linear chains carry approximately seven electrons per atom, which is consistent with our electron counting scheme.

10.4. $ZrTe_3$ and Related Binary Phases

The $ZrTe_3$ crystal structure[123, 124] is closely related to that of UTe_2 (Figure 30). One may arrive at $ZrTe_3$ by inserting an additional plane of linear Te chains into the UTe_2 structure (Figure 29). The nearly equidistant linear Te chains in UTe_2 are more distorted in $ZrTe_3$, the Te–Te bond lengths being 2.79 Å and 3.10 Å, respectively.[123, 124] The U atoms in UTe_2 share rectangular faces in the vertical direction, which is no

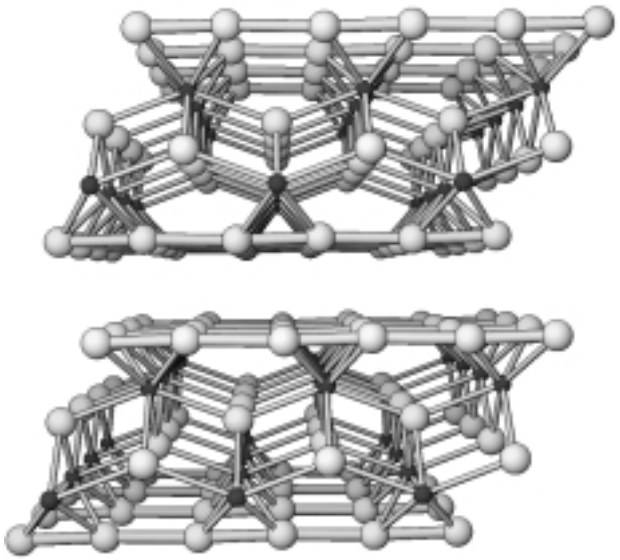

Figure 30. A perspective view of the crystal structure of $ZrTe_3$. Zr = small dark spheres; Te = large light spheres.

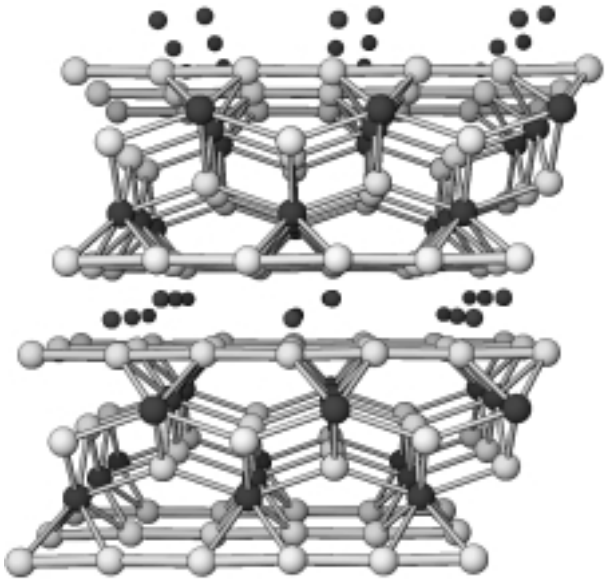

Figure 31. A perspective view of the crystal structure of $CuTh_2Te_6$. Th = large dark spheres; Cu = small dark spheres; Te = large light spheres.

longer the case for the $ZrTe_3$ crystal structure. Zr_2Te_6 slabs touch each other at van der Waals separation through the planes of linear Te chains.

If one assumes a -1 charge on the chain Te atoms and a -2 charge on the isolated Te atoms, then the Te_3 subnetwork should carry a -4 charge $(Te_2^{chain})^{2-}(Te^{atom})^{2-}$. Consequently, this forces a $+4$ oxidation state on Zr, which seems reasonable. Since the linear chains are pairwise distorted in $ZrTe_3$, one would expect a semiconducting behavior from this compound. This is not so, however. Linear muffin tin orbital (LMTO) DFT calculations by Stöwe and Wagner indicated that some Te and Zr bands crossed the Fermi level, and thus rationalized the metallic conductivity.[124] The formal oxidation state of Zr atoms was found to be near $+4$, as expected.[124]

Isostructural TX_3 binary phases were reported for other tetravalent metals (T = Zr, Hf, U) as well as for X = Se.[123] In all of these compounds, Te or Se atoms in the linear chains appear to have a -1 oxidation state, that is, seven electrons per atom.

10.5. AT_2X_6 Compounds: Ternary Phases with the $ZrTe_3$ Structure

A large number of ternary AT_2X_6 (A = K, Rb, Cs, Cu; T = U, Th; X = Se, Te) compounds have been reported which are closely related to the $ZrTe_3$ binary phase.[125–128] In all of these compounds the T_2X_6 slabs are similar to those found in $ZrTe_3$, but with monopositive ions intercalated into the van der Waals gap between the slabs (compare Figures 30 and 31). Two outcomes are possible upon the introduction of an extra electron into the T_2X_6 subnetwork—either the T^{4+} atoms become partially reduced to $T^{3.5+}$ or the X^- atoms in the linear chains are reduced to $X^{1.25-}$.

From the limited data available we suggest that both scenarios actually take place. Magnetic susceptibility measurements carried out for the $CuTh_2Te_6$ ternary phase indicate an effective magnetic moment of $2.06\,\mu_B$ per unit cell.[128] Assuming a $+4$ oxidation state for the Th atoms, and taking into account the presumably nonmagnetic nature of both Cu^+ ions and of the partially filled broad Te chain bands, one would expect diamagnetic behavior from this compound. Therefore, we attribute the paramagnetic behavior of $CuTh_2Te_6$ to the partial reduction of Th^{4+} ions, which could make them magnetic. It would follow that the Te atoms in the chain carry a charge closer to -1 than to -1.25.

The second scenario—the reduction of linear Se chains, happens in $MThSe_6$ (M = K, Rb).[125] These compounds show diamagnetic behavior, which suggests a $+4$ oxidation state of the Th atoms. Extensive physical measurements, including Raman spectroscopy, electron diffraction studies, and pair distribution function analysis, led Kanatzidis and co-workers to the conclusion that the plane of Se chains undergoes a static 4×4 CDW distortion (Scheme 21)[125] with linear Se chains distorting into Se_2^{2-} dumbbells and with the Se^{2-} isolated atoms completing an octet around each Se atom.

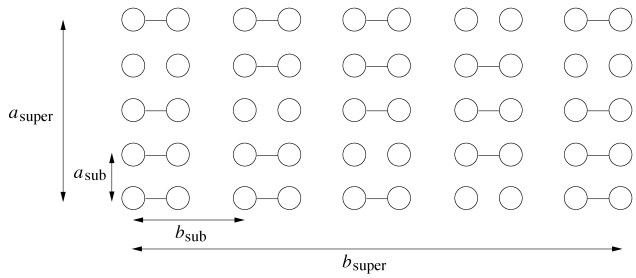

Scheme 21.

The limited set of physical property measurements on the compounds with an AT_2X_6 stoichiometry suggests that either tetrapositive T ions are reduced as in $CuTh_2Te_6$ (paramagnetic), or the linear X^- chains are reduced as in $MThSe_6$ (M =

K, Rb; diamagnetic), which results in a distortion of the linear chain into X_2^{4-} dumbbells and isolated X^{2-} atoms. In the former case, the X atoms in the linear chain carry approximately seven electrons per atom.

10.6. Linear Te Chains Which are not Mononegative

The $Tl_{0.56}UTe_3$ crystal is also isostructural to the $ZrTe_3$ binary phase and AT_2X_6 ternary phases discussed in Sections 10.4 and 10.5, respectively.[129] The Te chains, found in this compound, are almost uniformly spaced at 3.04 and 3.05 Å. The magnetic susceptibility measurements indicate an effective paramagnetic moment of 3.27 μ_B, which the authors suggest is close to the typical values for that observed for the U^{4+} ion.[129] If the U ions are indeed tetravalent in this compound, and assuming no CDW distortions, one is led to a -1.28 charge on the Te atoms in the linear chains.

A similar situation is observed for the $Cu_{0.28}LaTe_2$ ternary phase,[130] where uniformly spaced linear Te chains carry a -1.28 charge per Te atom. It is remarkable that in the related $LaTe_2$ binary phase the Te atoms form a square sheet instead of linear chains ($La^{3+}(Te^{atom})^{2-}Te^-$). Thus, when an additional 0.28 electrons are introduced into a square Te^- sheet, the latter disintegrates into linear chains.

Nearly perfect linear Te chains in the crystal structure of $Dy_3Cu_2Te_7$ have been reported recently by Lee and co-workers.[131] Assuming a +3 oxidation state for Dy and a +1 oxidation state for Cu, the authors arrive at a -1.25 oxidation state for the Te atoms in the linear chains.

10.7. Summary

We have examined in this section the bonding patterns and possible electron counting of a selection of binary and ternary phases of heavy main group elements which contain linear chains or their derivatives. It appears that the electron count of seven electrons per atom is dominant in these compounds, with a few exceptions of 7.25–7.28 electrons per chain atom found in Te ternary phases. We argued earlier that an electron count of six electrons per atom would force the linear chain to kink, while no bonding at all is expected at an electron count of eight electrons per atom. We estimate that the effective range for the electron count for a hypervalent linear chain might be between 6.5 and 7.5 electrons. The compounds made and structurally characterized to date point to a still narrower range of electron counts.

Having looked into the range of electron counts for linear chains, we next examine the range of possible electron counts for square sheets of elements of Groups 4 and 6.

11. Square Sheets in the Compounds of Group 4 Elements

Square sheets of Group 4 elements are realized in a wide variety of compositions and structure types and they offer a stringent test of our electron counting scheme. We first look at binary compounds having the $ZrSi_2$ structure type, followed by ternary and quaternary derivatives of $ZrSi_2$. The filled version of the $ZrSi_2$ type, the $CeNiSi_2$ structure type, is also considered. Finally, we examine some ternary compounds having the $CaBe_2Ge_2$ structure type, a ternary derivative of the $BaAl_4$ structure.

11.1 Binary $M^{IV}X_2$ and $M^{II}X_2$ Compounds

We have already encountered the $ZrSi_2$ structure type when discussing the $YbSb_2$ binary phase (see Figure 8). In that compound, which consists of zig-zag chains and square sheets of Sb atoms, we assigned a -1 charge to the Sb atoms in both networks. If one were to replace the divalent Yb cations by tetravalent ones, and the Sb atoms by Group 4 elements, then the total number of electrons remains the same.

However, many $M^{IV}X_2$ phases crystallize in quite different structure types, in particular in the $TiSi_2$, $CrSi_2$, $ThSi_2$, and AlB_2 structures. The crystal structures and electrical properties of $ZrSi_2$ and polymorphs of $TiSi_2$ have been extensively scrutinized recently for their potential application as contact materials in ultra-large-scale integrated circuits (ULSI).[132–135] Indeed, some $M^{IV}X_2$ structures listed in Figure 32 crystallize

	Ti^{4+} 0.74 Å	Hf^{4+} 0.83 Å	Zr^{4+} 0.84 Å	U^{4+} 1.00 Å	Th^{4+} 1.05 Å
Si 1.90 Å	**0.39** $ZrSi_2$ $TiSi_2$	**0.44** $ZrSi_2$	**0.44** $ZrSi_2$	**0.53** $ThSi_2$ AlB_2	**0.55** $ThSi_2$ AlB_2
Ge 2.00 Å	**0.37** $TiSi_2$	**0.42** $ZrSi_2$	**0.42** $ZrSi_2$	**0.50** $ZrSi_2$	**0.53** $ZrSi_2$ $ThSi_2$ $ThGe_2$
Sn 2.16 Å	**0.34**	**0.38** $CrSi_2$	**0.39** $TiSi_2$	**0.46**	**0.49** $ZrSi_2$

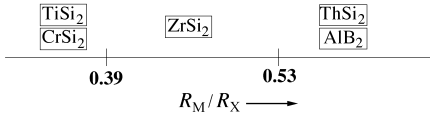

Figure 32. Crystal structure types of $M^{IV}X_2$ compounds, where X = Si, Ge, Sn.[132, 134–147] The ionic radii of M^{IV} ions for coordination number eight (found in the $ZrSi_2$ structure) were taken from the CRC Handbook of Chemistry and Physics,[155] while the corresponding radii of X were estimated from averaged metal–element bond lengths in $HfSi_2$ ($ZrSi_2$-type), $HfGe_2$ ($ZrSi_2$-type), and $ZrSn_2$ ($ZrSi_2$-type) crystal structures. The ionic radii ratio R_M/R_X is given for each pair. Some of the stoichiometries exhibit polymorphism, as indicated by the simultaneous inclusion of several structure types in corresponding fields.

with the same $ZrSi_2$ structure type (shown in Figure 33 a), that is, with zig-zag chains and square sheets of X^{2-} (six electrons per X atom).

Given the same electron count for all the compounds in Figure 32, it is apparent that other factors play a key role in determining the stability of various structure types. Inspired by the structural maps of Villars and co-workers[148, 149] and by earlier work of many other authors, we have been able to separate various structure types into distinct domains using the metal–element ionic size ratio R_M/R_X as a key parameter

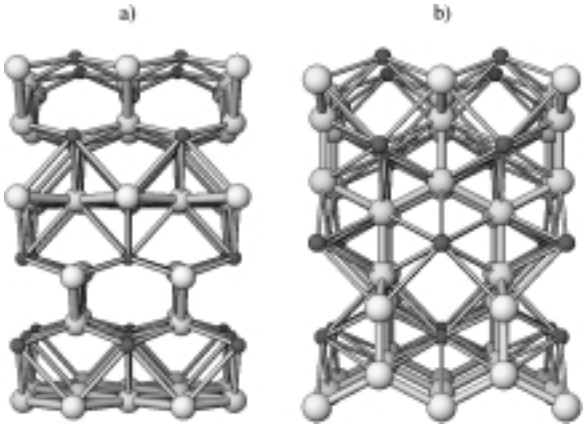

Figure 33. a) A perspective view of the $ThSn_2$ ($ZrSi_2$ type) crystal structure. Th = small dark spheres; Sn = large light spheres. b) A perspective view of the $EuSi_2$ ($ThSi_2$ type) crystal structure. Eu = small dark spheres; Si = large light spheres.

(Figure 32). The $ZrSi_2$ structure is stable between R_M/R_X ratios of 0.39 and 0.53. We will pick up this point in Section 11.2 when discussing the crystal chemistry of rare earth disilicides, digermanides, and distannides.

When Yb^{2+} atoms in the $YbSb_2$ crystal structure are substituted by Sm^{3+} atoms (see the earlier discussion in Section 3.5 on Sb compounds), the zig-zag chains accommodate the extra electron by breaking up into isolated Sb_2 pairs, preserving the electron count of six electrons per atom in the square sheets. One would like to know if this robust electron count for the square sheet is characteristic for sheets comprised of the Group 4 elements as well. For example, what are the consequences of replacing tetravalent cations by trivalent and divalent ones?

The structures provide a straightforward answer for the divalent Ca, Sr, and Eu cations. In these $M^{II}X_2$ compounds the X atoms carry an average -1 charge, that is, five electrons per atom. Such an electron count implies a classical three-connected network. This is indeed what happens: Si atoms in $EuSi_2$ form three-connected networks in both the $ThSi_2$[150] (Figure 33b) and AlB_2[151] structure types (Figure 34a for

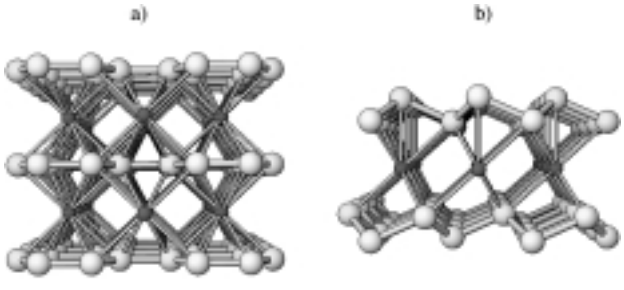

Figure 34. a) A perspective view of the $YbSi_2$ (AlB_2 type) crystal structure. Yb = small dark spheres; Si = large light spheres. b) A perspective view of the $CaSi_2$ ($CaSi_2$ type) crystal structure. Ca = small dark spheres; Si = large light spheres.

$YbSi_2$ in the AlB_2 structure type). In the latter the Si atoms form a graphite-like sheet sandwiching the metal ions. Corrugated three-connected As-like sheets are found[152] in the $CaSi_2$ crystal structure (Figure 34b), which may be transformed under pressure into a three-connected $ThSi_2$ network[153] (Figure 33b). $SrSi_2$ forms yet another three-connected Si network,[154] which also may be transformed into a $ThSi_2$ network under pressure.[153]

If the ratio of the ionic radii is indeed a critical parameter in determining the stability of the $ZrSi_2$ structure type (Figure 32), then the larger size of divalent Ca, Sr, and Eu[155] may be the reason for the absence of this structure type, that is, the R^{II}_M/R_X ratio is well over 0.53 (Figure 32). Therefore, we consider next the substitution of tetravalent cations in MX_2 compounds by trivalent rare earth ones, which have ionic radii comparable to those of Th^{4+} and U^{4+} ions.

11.2. Binary REX_2 Phases

Figure 35 shows in graphic form the major structure types which are assumed by REX_2 compounds. Let it not be said that chemistry is about simplicity—no less than eight structure types are displayed by this isoelectronic group of compounds.

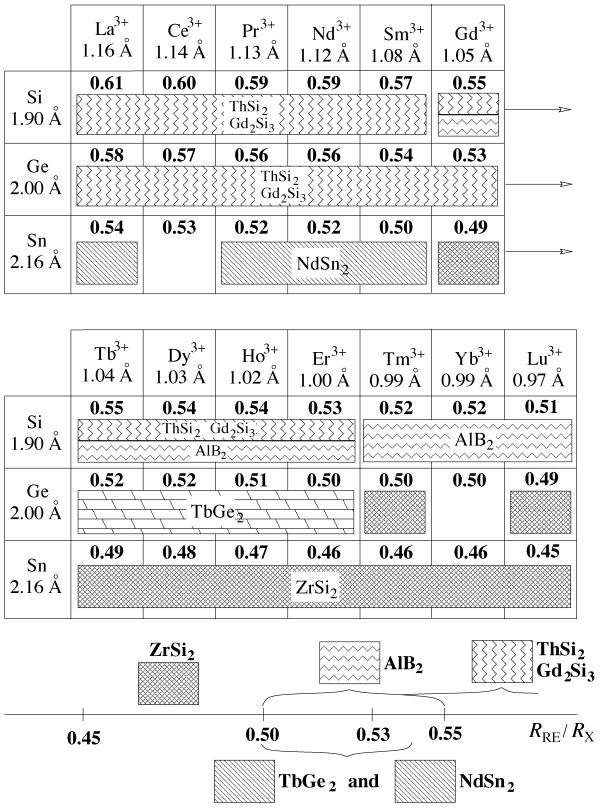

Figure 35. Crystal structure types of $M^{III}X_2$ compounds, where X = Si, Ge, Sn.[156, 158–177] The ionic radii of M^{III} for coordination number eight (found in the $ZrSi_2$ structure) were taken from the CRC Handbook of Chemistry and Physics.[155] The ionic radii ratio R_M/R_X is given for each pair.

As indicated by many authors in the field,[156–163] the ratio of ionic sizes and the degree of nonstoichiometry (defects on X sites) are the most important factors in stabilizing various structure types. Our calculated R_{RE}/R_X ionic ratios strongly indicate that stability zones exist for all structure types (Figure 35). The $ZrSi_2$ structure type is realized for the smallest R_{RE}/R_X ratio, while the tetragonal $ThSi_2$ structure

type and the closely related orthorhombic Gd_2Si_3 structure type are realized for the largest ratio. For the small ratio range of 0.50–0.55 several structure type domains coexist, with $TbGe_2$ being a $ZrSi_2$–$ThSi_2$ hybrid structure type. Rare earth disicilicides, RE = Gd, Er, having the R_{RE}/R_X ratio at the boundary of $ThSi_2/Gd_2Si_3$ and AlB_2 stability zones, crystallize in all three structure types, depending on the temperature and other conditions (Figure 35).

A simplistic approach to understanding the structural domain formation in Figures 32 and 35 may be obtained from perusal of the coordination polyhedra of rare earth metals in these structure types (Table 5). We have taken into account only the closest bonding rare earth–element contacts, and also for $NdSn_2$ two strong Nd–Nd interactions have been considered. By comparing the data from Table 5 with the structure maps in Figures 32 and 35, one observes a reasonable correlation between the ionic size ratio and the higher coordination number of the rare earth atoms.

Table 5. Coordination number of metal ions in various ME_2 structure types presented as a sum of the number of neighboring atoms + the number of atoms in the next shell, located approximately 10% further away than the closest atoms. The Nd atoms in $NdSn_2$ are connected to two other Nd atoms (6* = 4 M-X + 2 M-M).

Structure type	$CrSi_2$, $TiSi_2$	$ZrSi_2$	$NdSn_2$	AlB_2	$ThSi_2$
coordination polyhedron	4 + 6	8 + 2	6* + 6	12 + 0	12 + 0

To further rationalize these observations we notice that the $ThSi_2$ structure obeys Zintl–Klemm electron counting rules only for divalent metals, that is, the three-connected X^- network is electronically saturated in $M^{2+}(X^-)_2$ (with a lone pair of electrons at each Si atom). An extra electron is introduced by trivalent rare earth metals; this electron could either reduce the rare earth ions or enter the σ* antibonding orbitals of the X framework. There is neither direct evidence for the reduction of the rare earth ions nor for significant weakening of X–X bonding (the Si–Si bond lengths are 2.31 and 2.42 Å in $Eu^{2+}Si_2$ and 2.28 and 2.43 Å in $La^{3+}Si_2$; 2.35 Å is a normal Si–Si single bond length).

Still another way to stabilize the system when extra electrons are present is to introduce defects into the anionic sublattice. Dangling bonds on the X atoms adjacent to the defect sites are created in this way; these dangling bonds could in turn become lone pairs by absorbing additional electrons.

The explanation given above is consistent with the X atom deficiency most commonly reported for these compounds.[162, 163] Rare earth disilicides with the $ThSi_2$ structure type are often found with a $REX_{1.7-1.8}$ stoichiometry. The number of X vacancies is even higher for the compounds with the AlB_2 structure type, for which the X stoichiometry is often less than $REX_{1.7}$.[161, 163] Several authors have argued that the AlB_2 structures should be stable at even lower electron counts than the $ThSi_2$ ones,[170, 178] which might be one of the explanations of the higher X deficiency in these compounds.

By considering the data in Figures 32 and 35 we conclude that for ion size ratios R_M/R_X between 0.40 and 0.50, $ZrSi_2$ is the only structure type that is available to MX_2 compounds. This postulation is supported by the existence of the $TbGe_2$ structure type (Figure 36) at the boundary of $ZrSi_2$–$ThSi_2$ stability zones. In the $TbGe_2$ crystal structure half of the square Ge sheets from the $ZrSi_2$ structure type undergo a puckering distortion and merge with the Ge zig-zag chains above and below, which creates finite slabs of the $ThSi_2$ structure type sandwiched between square Ge sheets. By assigning a −2 charge to two-connected Ge atoms and a −1 charge to three-connected Ge atoms in the slabs, we arrive at a −1 charge on Ge atoms in the square sheets of $(Tb_2)^{6+}(Ge_3^{slab})^{4-}(Ge^{square})^{2-}$.

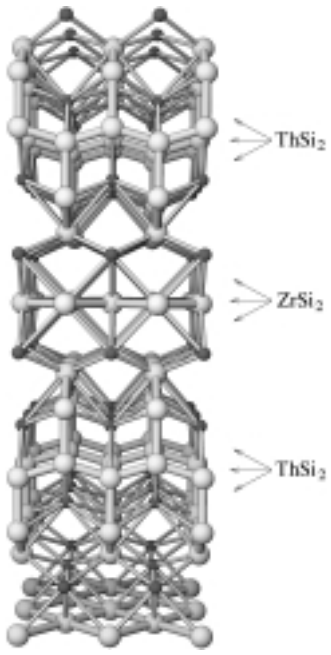

Figure 36. a) A perspective view of the crystal structure of $TbGe_2$. Tb = small dark spheres; Ge = large light spheres.

The electron count of six electrons per atom in square Ge sheets in the $TbGe_2$ structure is reduced to five for REX_2 compounds with the $ZrSi_2$ structure type. Thus square sheets of Group 4 elements may also exist for that electron count. Are there any structural consequences of the five electron count, since the nonbonding or slightly antibonding region of square sheet hypervalent bands are emptied in this case (see the discussion in Section 5)?

We have only the $ErSn_2$[156]structure to go by. One observes the following difference between the crystal structures of $ThSn_2$ ($ZrSi_2$ type) and $ErSn_2$ ($ZrSi_2$ type): the distance between the Sn atoms in the square sheets and Sn atoms in the zig-zag chains is reduced from 3.90 Å in $ThSn_2$ to 3.67 Å in $ErSn_2$, although Th^{4+} and Er^{3+} have comparable ionic sizes (see Figures 32 and 35). Moreover, the same distance in the "electronically saturated" $TbGe_2$ crystal structure is 3.81 Å, in spite of Ge being smaller than Sn. We believe that oxidation of the square sheet from six to five electrons per atom results in the tendency of "unsaturated" square sheet atoms to form secondary interactions with the zig-zag chains.

This conclusion is further supported by the light rare earth stannides crystallizing with the $NdSn_2$ structure type.[166, 168] In these compounds the square sheets merge fully with the zig-zag chains, simultaneously breaking bonds between the zig-zag chain atoms (Figure 37). This results in a remarkable layered structure of vertex-sharing octahedra, separated by rare earth ions.

Vajenine and Hoffmann recently demonstrated that the electron count in 2D sheets of vertex-sharing Al octahedra should be around 10–12 electrons per octahedron, which is significantly less than 22 electrons found in Nd_2Sn_4 (six electrons coming from Nd_2 and sixteen electrons from Sn_4).[179] Preliminary calculations indicate that the contraction of s

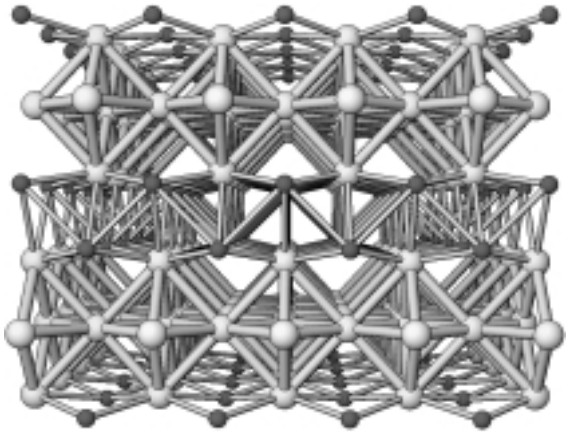

Figure 37. a) A perspective view of the crystal structure of $NdSn_2$. Nd = small dark spheres; Sn = large light spheres.

orbitals and the relative unimportance of π bonding for the heavier elements (see the earlier discussion in this paper) could substantially increase the magic electron count for such networks of condensed octahedra.[180] We expect a 2D lattice of vertex-sharing octahedra of heavy main group elements to be stable around 18 electrons per octahedron.[180] The existence of short Nd – Nd contacts (3.15 Å) in $NdSn_2$ implies that each Nd atom donates less than three electrons to the Sn subnetwork, which brings down the number of electrons per octahedron from 22 to 20 or, perhaps, 18.

11.3. Compounds with the $CeNiSi_2$ Structure Type

In the discussion above we concluded that when tetravalent metal atoms in the $ZrSi_2$ structure are substituted by trivalent rare earth ones the electron count in square sheets reduces from six to five, which induces certain secondary interactions with zig-zag chains. If it were possible to fill the square-pyramidal voids in the $RESn_2$ series of compounds ($ZrSi_2$ type) with metal cations, then the electron count in Sn square sheets could, in principle, be brought back from five to six, or perhaps even seven electrons per sheet atom. Gladyshevskii, Bodak, and co-workers reported the synthesis and characterization of several $RELiSn_2$ ternary phases (RE = La, Ce, Pr, Nd, Sm, Gd, Tb, Dy, Ho, Er, Tm, Lu) which crystallize with the $CeNiSi_2$ structure, a filled version of the $ZrSi_2$ structure.[181] A perspective view of the isostructural $BaCuSn_2$ is shown in Figure 38. For the purpose of simplicity we have not drawn connections between Ba/rare earth atoms and the Sn sublattice, as was shown above for the $ZrSi_2$ structure (see Figure 33a).

The magnetic susceptibility measurements indicate that all rare earth atoms are tripositive in $RELiSn_2$.[181] Given the plausible assumption of Li being monopositive, we are led to the $RE^{3+}Li^{+}(Sn^{zig\text{-}zag})^{2-}(Sn^{square})^{2-}$ formulation, namely, once again six electrons per square sheet atom. Schäfer and co-workers prepared some isostructural LaT_xSn_2 compounds (T being a transition metal atom; T = Cu: $x = 0.56$, T = Ni: $x = 0.74$, T = Co: $x = 0.52$, T = Fe: $x = 0.34$).[182] According to the authors, if all these compounds were to be isoelectronic, then Cu should be 2+ in $LaCu_{0.56}Sn_2$, Ni 1.33+ in $LaNi_{0.74}$, Co 2+ in $LaCo_{0.52}Sn_2$, and Fe 3+ in $LaFe_{0.34}Sn_2$[182] This line of reasoning is consistent with Cu sites being fully occupied in $BaCuSn_2$, since the substitution of La^{3+} by Ba^{2+} and the simultaneous enhancement of the Cu^{2+} occupation from 0.56 to 1 would keep the number of electrons approximately constant.

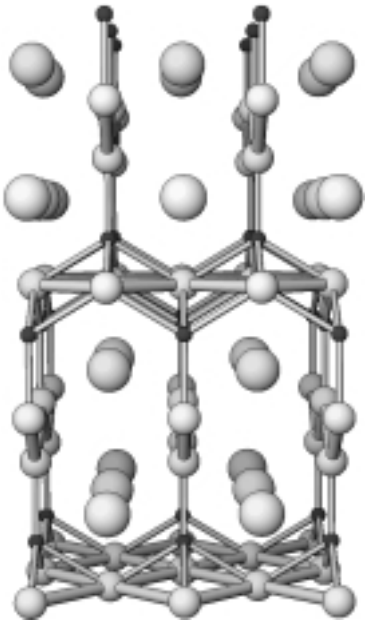

Figure 38. a) A perspective view of the crystal structure of $BaCuSn_2$ ($CeNiSi_2$ type). Cu = small dark spheres; Sn = larger light spheres; Ba = the largest light spheres.

The proposed trivalency of Fe[182] is supported by the results of Bodak and co-workers who reported $REFe_{0.33}Si_2$ compounds with other rare earth elements (RE = Y, Tb, Ho, Er, Tm, Lu).[183] It is interesting to note that $REFeSi_2$ compounds with full Fe stoichiometry crystallize with an alternative $TbFeSi_2$ structure type.[184] The Ni occupation value in $RENi_xE_2$ (E = Si, Ge, Sn) compounds varies from 1.5 to 2, which renders the determination of its oxidation state difficult.[182, 185–189] Kumigashira and co-workers have concluded from a high-energy-resolution photoemission study of $CeNiSi_2$ and $CePtSi_2$ that the d bands of Ni and Pt are, respectively, 2.0 eV and 4.4 eV below the Fermi level. If one assumes that Ni does not contribute any electrons to the Si sublattice, and given the valence fluctuation of Ce (from 3.35 at 300 K to 3.65 at 50 K, as indicated by magnetic susceptibility measurements), one is led to 5.35 – 5.65 electrons per square Si atom in this compound.[187, 185] Extensive reviews of the $CeNiSi_2$ type compounds are given by Parthé and Chabot[190] and Rogl.[191] Proserpio, Chacon, and Zheng[189] provide an alternative theoretical view of Ge subnetworks in $LaNiGe_2$ as donor layers and acceptors which lead to chain formation.

Now we are ready to examine if the square sheets can be reduced to have more than six electrons per atom.

11.4. Square Sheets of Group 4 Elements in Compounds Having $ZrSi_2$-Related Structures

If one takes as a starting point the $ZrSi_2$ binary phase, then an obvious way to introduce extra electrons into the structure is to replace Group 4 Si by a Group 5 or 6 element. Indeed, Si

may be replaced by more electron-rich Se in the ZrSiSe ternary compound shown in Figure 39a.[192] In principle there are two anionic subnetworks in the $ZrSi_2$ crystal structure that could absorb these two extra electrons: square sheets and zig-zag chains. We encountered a similar situation earlier in the paper when contemplating the consequences of the replacement of divalent Yb in $YbSb_2$ (also the $ZrSi_2$ structure type)

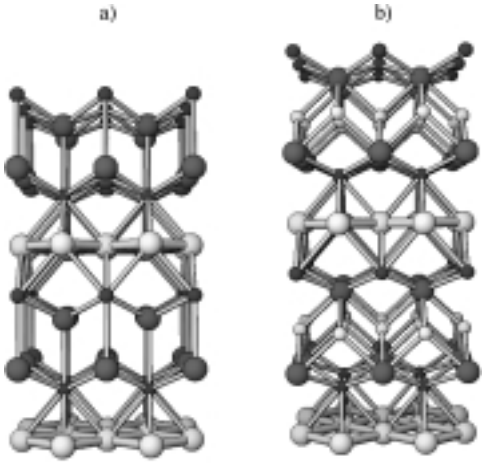

Figure 39. a) A perspective view of the crystal structure of ZrSeSi (PbFCl type). Zr = small dark spheres; Si = large light spheres; Se = large dark spheres. b) A perspective view of the crystal structure of ZrCuAsSi (ZrCuAsSi type). Zr = small dark spheres; Cu = small light spheres; Si = large light spheres; As = large dark spheres.

by a trivalent cation. In that case, it turned out that zig-zag Sb^- chains got reduced and broke into isolated Sb_2^{4-} pairs, as in $SmSb_2$ (see Figures 8 and 9).

A similar pattern is found also for the ZrSiSe crystal structure (the PbFCl structure type, sometimes referred to as the anti-Cu_2Sb type, as well as by other names[193]). The Se atoms occupy positions related to zig-zag Si positions in the $ZrSi_2$ structure, but the zig-zag chains disintegrate into isolated atoms. Hence, to complete an octet around each Se we assign charges to ZrSiSe as $Zr^{4+}(Si^{square})^{2-}(Se^{atom})^{2-}$. Therefore, the electron count of six electrons per square sheet atom in $ZrSi_2$ is preserved as well in ZrSiSe. Isoelectronic compounds having the same PbFCl structure type have been reported for most of the chalcogen-Group 4 element-tetravalent metal combinations (see Table 6). The same number of electrons is also preserved when both the chalcogen and the Group 4 element are simultaneously replaced by a Group 5 element. The resulting pnictide square sheets then carry six electrons per atom as well ($Th^{4+}(Pn^{atom})^{3-}(Pn^{square})^-$; Pn = As, Sb, Bi).[194–196] We will return to PbFCl type compounds in the next section when considering rare earth dichalcogenides.

In an isoelectronic substitution of ZrSiSe, tetravalent Zr is replaced by pentavalent Nb or Ta, and, simultaneously, Se by As.[197, 198] These compounds also crystallize with the same Cu_2Sb structure type, with the As atoms being found in isolated positions. The assignment of formal charges as $M^{5+}(Si^{square})^{2-}(As^{atom})^{3-}$ (M = Nb, Ta) still suggests an electron count of six electrons per atom in square Si sheets.

The next step in elaboration of these compounds was taken by Johnson and Jeitschko, who substituted isoelectronically pentavalent Nb atoms in NbSiAs by tetravalent Zr or Hf and monovalent Cu atoms.[201] The crystal structure of ZrCuAsSi is shown in Figure 39b. Cu atoms insert themselves inbetween isolated As atoms in a tetrahedrally coordinated environment. One may also think of the ZrCuAsSi crystal structure as being derived from a $ZrSi_2$ crystal structure by first replacing Si atoms in the zig-zag chains by As atoms, then inserting a plane of Cu atoms so as to break zig-zag chains into isolated atoms (compare Figures 33a and 39b).[204] Thus, the electron count of six electrons per atom in square Si sheets persists for these quaternary phases as well.

It turns out that it is possible to replace Group 5 As atoms in ZrCuAsSi and HfCuAsSi back by a Group 4 element.[202–204] The resulting $CuME_2$ (M = Hf, Zr; E = Si, Ge) ternary phases crystallize with the same ZrCuAsSi structure type, thus having one electron less per formula unit. If one assumes that an octet around each isolated Si or Ge atom, then a -1 charge has to be assigned to the Si and Ge atoms in the square sheets. In discussing the $ErSn_2$ crystal structure we have suggested that "electronically unsaturated" Sn^- square sheets develop secondary interactions with zig-zag Sn chains. One observes here a similar trend as well: the $Si^{square}-X^{atom}$ distance shrinks gradually as the electron count of the square sheet diminishes from 6 to 5.5 and then to 5. For instance, the Cu–As and Cu–Si bond lengths are similar in CuZrAsSi and $CuZrSi_2$, while the $Si^{square}-X^{atom}$ distance shrinks from 3.58 to 3.37 Å.

An intermediate electron count of 5.5 per square sheet atom is found in a series of compounds with the $CuHf_2Ge_4$ and $Cu_4Zr_3Si_6$ structure types (Table 6). As pointed out by Thirion and co-workers, one may imagine these compounds as being derived from the $ZrSi_2$ crystal structure by inserting Cu planes into the zig-zag chains in $ZrSi_2$.[204] In the $CuHf_2Ge_4$ crystal structure, for example, Cu planes break half of the zig-zag chains rendering the $Cu^+(Hf_2)^{8+}(Ge^{atom})^{4-}(Ge^{zig\text{-}zag})^{2-}$-$(Ge_2^{square})^{3-}$ assignment of charges. The $Cu_4Zr_3Si_6$ crystal structure is somewhat further modified, having Si_2 pairs in addition to square Si sheets and isolated atoms (Figure 40). The short Si–Si bond in the Si_2 pairs (2.29 Å) suggests that

Table 6. Compounds containing Group 4 elements which crystallize in structure types related to $ZrSi_2$.

Structure type	Compounds	Electrons per atom^{square}
Cu_2Sb	HfGeS,[192] HfGeSe,[192] HfGeTe,[192] HfSiSe,[192] HfSiTe,[192] ZrGeS,[199] ZrGeSe,[199] ZrGeTe,[199] ZrSiS,[199] ZrSiSe,[192] ZrSiTe,[199] UGeS,[200] USiS,[200] USnTe,[200] NbAsSi,[197] TaAsSi[198]	6
ZrCuAsSi	ZrCuAsSi,[201][a] HfCuAsSi,[201][a] $CuHfGe_2$,[202][b] $CuZrGe_2$,[202][b] $CuHfSi_2$,[202, 203][b] $CuZrSi_2$[202–204][b]	6[a]/5[b]
$CuHf_2Ge_4$	$CuHf_2Ge_4$, $CuHf_2Si_4$,[204] $CuZr_2Ge_4$,[205] $CuZr_2Si_4$[204]	5.5
$Cu_4Zr_3Si_6$	$Cu_4Zr_3Si_6$[204]	5.5 (see the text)

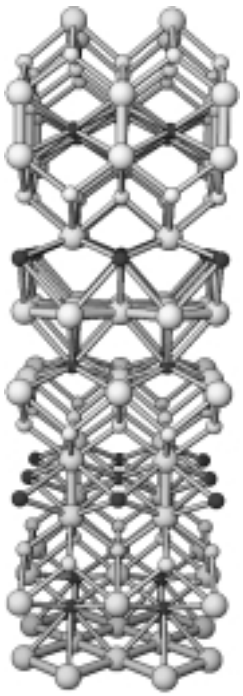

Figure 40. A perspective view of the crystal structure of $Cu_4Zr_3Si_6$. Zr = small dark spheres; Cu = small light spheres; Si = large light spheres.

they are oxidized relative to the single bond Si_2^{6-} formulation, perhaps to Si_2^{5-} (the Si–Si bond length in elemental Si with the diamond structure is 2.35 Å; the Si–Si bond in Si_2^{6-} pairs in $BaMg_2Si_2$ is 2.48 Å[206]). Assuming the −5 charge on Si_2 pairs, the remaining formal charges may be assigned as $(Cu_4)^{4+}(Zr_3)^{12+}(Si_2^{atom})^{8-}(Si_2^{pair})^{5-}(Si_2^{square})^{3-}$, namely, 5.5 electrons per Si atom in the square sheet. The Si^{square}–Si^{atom} distance of 3.47 Å is intermediate between six (CuZrAsSi) and five ($CuZrSi_2$) electrons per atom in the square sheet compounds (Table 7).

Upon substituting the Group 4 elements by chalcogens in the $ZrSi_2$ structure, two additional electrons enter the zig-zag chains and break them into isolated chalcogen atoms. A multitude of other substitutions of the resulting ZrSiS-like structures by various elements demonstrates clearly that the electron count of six electrons per square sheet atom is really dominant in related crystal structures. However, reduced electron counts of 5.5 and 5 electrons per square sheet atom are realized as well. For these compounds, "electronically unsaturated" square sheets come closer in distance to the isolated element atoms, as demonstrated earlier for the $RESn_2$ compounds. In the following subsection, which wraps up our discussion of the square sheets of Group 4 elements, we consider a group of ternary compounds with the $BaAl_4$ structure type.

11.5. Square Sheets of Group 4 Elements in the $BaAl_4$-Derived Compounds

Two common ternary derivatives of the $BaAl_4$ structure are the $ThCr_2Si_2$ and $CaBe_2Ge_2$ structure types (Figure 41). In the former one, the most electronegative element X occupies a single crystallographic site, forming X···X pairs, which may

Table 7. Selected geometrical data for various $ZrSi_2$-related crystal structures containing square Si sheets.

	Si^{square}-$X^{[a]}$ [Å]	Si^{square}-Si^{square} [Å]	M^{IV}-Si^{square} [Å]	M^{IV}-$X^{[a]}$ [Å]	Cu-$X^{[a]}$ [Å]	Electrons per $atom^{square}$
HfSeSi	3.68	2.57	2.82	2.77	–	6
ZrSeSi	3.64	2.56	2.81	2.75	–	6
CuZrAsSi	3.58	2.60	2.83	2.76	2.51	6
$CuZr_3Si_6$	3.47	2.64	2.84	2.76	2.44	5.5
$CuZrSi_2$	3.37	2.63	2.86	2.71	2.53	5
$CuHfSi_2$	3.36	2.64	2.86	2.71	2.52	5

[a] X = Se^{atom} for HfSeSi and ZrSeSi; X = As^{atom} for CuZrAsSi; X = Si^{atom} for $CuZr_3Si_6$, $CuZrSi_2$, and $CuHfSi_2$.

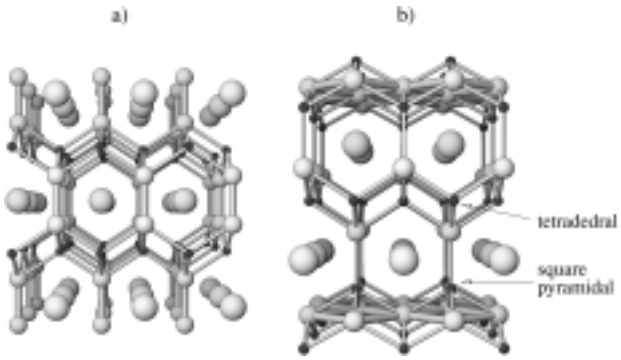

Figure 41. a) A perspective view of the crystal structure of $BaMg_2Ge_2$ ($ThCr_2Si_2$ type). Mg = small dark spheres; Ge = larger light spheres; Ba = the largest light spheres. b) A perspective view of the crystal structure of $BaZn_2Sn_2$ ($CaBe_2Ge_2$ type). Zn = small dark spheres; Sn = larger light spheres; Ba = the largest light spheres.

be bonded. In the $CaBe_2Ge_2$ crystal structure, X atoms occupy two distinct crystallographic sites, which results in square sheets and isolated atoms. Hoffmann and Zheng have analyzed the variation in X–X interactions in X_2 dumbbells in the $ThCr_2Si_2$ compounds as a function of the filling of the X_2 σ* orbital for various transition metals.[207] They have also considered the formation of $CaBe_2Ge_2$ structures as a consequence of donor–acceptor interactions.[208]

In this review we are led to still another perspective on this fascinating structure. Since X square sheets are present only in the $CaBe_2Ge_2$-type phases we are going to concentrate only on those. Furthermore, we ignore, for the moment, the interactions between the anionic X subnetwork and the remaining cations (which was the focus of the previous work). From this simplified point of view, the assignment of charges to alkaline earth members of this structural family is rather straightforward: $Ca^{2+}(Be^{2+})_2(Ge^{atom})^{4-}(Ge^{square})^{2-}$, that is, again six electrons per atom in square Ge sheets. The rather long Ge–Ge bond length of 2.84 Å within square Ge^{2-} sheets[209] is consistent with the hypervalent nature of those bonds.

The same electron count is present for other alkaline earth compounds, namely $BaMg_2Pb_2$ (Pb–Pb bond length is 3.54 Å in square sheets) and $BaZn_2Sn_2$ (Sn–Sn bond length is 3.32 Å in square sheets), assuming Zn is divalent in the latter compound.[209] The $BaMg_2Sn_2$ crystal structure (Figure 42) is an intergrowth of $ThCr_2Si_2$ and $CaBe_2Ge_2$ structure types, namely, square Sn

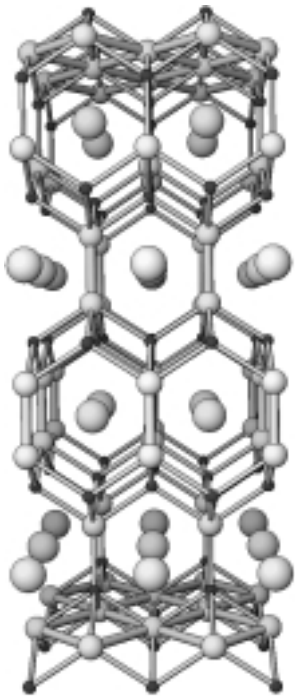

Figure 42. A perspective view of the crystal structure of $BaMg_2Sn_2$. Mg = small dark spheres; Sn = larger light spheres; Ba = the largest light spheres.

sheets, Sn_2 dumbbells, and isolated Sn atoms are present simultaneously.[206] If we follow our usual path and assign a -4 charge to isolated Sn, a -6 charge to Sn_2 pairs, then we are led again to square Sn^{2-} sheets ($(Ba_2)^{4+}(Mg_4)^{8+}(Sn^{atom})^{4-}(Sn_2^{pair})^{6-}(Sn^{square})^{2-}$). The Sn–Sn distance of 3.46 Å within square Sn^{2-} sheets, although within a hypervalent bonding range, is noticeably longer than the Sn–Sn distance of 3.13 Å found in square Sn^{2-} sheets in $ThSn_2$. It is not clear at present if such a difference in Sn–Sn bond lengths is caused by electronic or by electrostatic and size factors.

A few MM'_2X_2 compounds (M = U, La, Ce, Sm; M′ = Ni, Cu, Rh, Pd, Ir, Pt) with the $CaBe_2Ge_2$ structure type have been reported.[182, 191, 210–212] Here we concern ourselves only with the Cu-containing compounds, where we could possibly speculate about the possible formal oxidation states of the Cu atoms. In the MCu_2X_2 ($CaBe_2Ge_2$-type) structure there are two distinct types of Cu atoms, those having tetrahedral and square-pyramidal coordinations (Figure 41 b). We discussed earlier the proposition of Schäfer and co-workers to consider Cu as dipositive in $LaCu_{0.56}Sn_2$,[182] the Cu atoms also having a square-pyramidal coordination. If one extends this line of reasoning and assumes square-pyramidal Cu atoms to be dipositive, and the tetrahedral Cu atoms to be monopositive, then the following picture emerges for Cu ternary phases with the $CaBe_2Ge_2$ structure.

Purwanto and co-workers have reported the $UCu_{1.5}Sn_2$ crystal structure, in which the Cu deficiency is fully concentrated in square-pyramidal sites.[213] If U is assumed to be tetravalent, one arrives at the $U^{4+}(Cu^{tetr.})^{+}(Cu_{0.5}^{sq\text{-}pyr.})^{+}(Sn^{atom})^{4-}(Sn^{square})^{2-}$ formulation. This interpretation is consistent with Cu having a full occupancy in related rare earth compounds ($RECu_2Sn_2$, RE = La, Ce, Sm), as the loss of a single electron in the U/RE substitution is compensated by additional 0.5 Cu^{2+} square-pyramidal ions.[182, 214–217] Although our suggestion of mixed Cu^{2+}/Cu^{+} oxidation states is consistent both with the earlier work of Schäfer and co-workers,[182] as well as with the stoichiometries of reported experimental compounds, it remains somewhat speculative. Unfortunately, we can say even less about $CaBe_2Ge_2$-type compounds containing Ir, Rh, Ni, Pd, and Pt—a common difficulty in determining formal oxidation states of these nonmagnetic transition metal atoms.[211, 215, 216, 218, 219] Another interesting complication of many of these phases is the rich interplay of Kondo-like and heavy fermion behavior.[211, 214–216]

Ternary alkaline earth compounds having the $CaBe_2Ge_2$ crystal structure contain square sheets of Group 4 elements which carry six electrons per square sheet atom. If one assumes a mixed Cu^{+}/Cu^{2+} valence in the ternary U/rare earth compounds, then one is led to six electrons per square sheet atom in these compounds as well. The difficulty of assigning a formal charge to other transition metals in $CaBe_2Ge_2$-type phases renders it difficult to make the electron counting in square sheets of these phases definitive.

11.6. Summary

We have looked in this section at binary, ternary, and quaternary compounds of Group 4 elements which contain square sheets as a structural motif. Square sheets carry six electrons per atom in $M^{IV}X_2$ compounds having the $ZrSi_2$ crystal structure, which is consistent with our hypervalent bonding scheme. When the tetravalent metal is replaced by a trivalent rare earth one, then square sheets are realized in two structure types: $TbGe_2$ and $ZrSi_2$. The electron count of six electrons per atom in compounds of the $TbGe_2$ type is reduced to five in $ZrSi_2$-type compounds. In the latter, the "electronic unsaturation" of square sheets leads to secondary interactions of the sheets with zig-zag chains. The ultimate manifestation of this extra bonding is the structural collapse of square sheets and zig-zag chains into two-dimensional sheets of vertex-sharing Sn octahedra in the $NdSn_2$ structure.

When square-pyramidal voids in the $ZrSi_2$ structure are filled by metal ions, a $CeNiSi_2$ structure type is formed. It is suggested that in most of these compounds the square sheets of Group 4 elements carry six electrons per atom.

If a substitution is made in the $ZrSi_2$ structure so as to inject more electrons into the anionic subnetwork, then these extra electrons enter the zig-zag chains, breaking them apart. The resulting ternary and quaternary phases crystallize in several structure types, having six electrons per square sheet atom in most of the compounds. Reduced electron counts of 5 and 5.5 electrons per atom are realized as well, which result again in certain secondary interactions between square sheets and zig-zag chains or isolated atoms.

Square sheets of Group 4 elements are also found in the $CaBe_2Ge_2$ structure type, a ternary derivative of the well-known $BaAl_4$ structure. For those compounds where the assignment of oxidation states to metal cations is unambiguous, we find an electron count of six electrons per atom in square sheets. For the Cu-containing ternary phases we have proposed a mixed Cu^{2+}/Cu^{+} valence, which would also result in six electrons per square sheet atom in these compounds. The oxidation states of other transition metals with the $CaBe_2Ge_2$ structure type have not been determined.

The overall analysis of the compounds containing square sheets of Group 4 elements strongly indicates a preferred electron count of six electrons per square sheet atom. However, electron counts between five and six electrons per square sheet atom are realized as well. In certain cases these unsaturated square sheets develop secondary interactions with other anionic subnetworks.

Having looked at a large number of compounds containing square sheets of Group 4 and 5 elements, we have not found any that carry more than six electrons per square sheet atom. Square chalcogen sheets provide an opportunity to examine square sheets which are electron rich relative to our formulation, the last topic of our paper.

12. Square Chalcogen Sheets

In applying our electron counting scheme to square sheets of chalcogen atoms one is immediately faced with the following problem: chalcogen atoms carrying six electrons (the magic number for the square sheet) would be neutral. We have not really stressed the significance of ionic interactions in this paper, but it is self-evident that Madelung energies

influence critically the stability of a particular crystal structure relative to other alternatives. Given that the square sheets of chalcogen atoms would be immersed in the matrix of surrounding cations, their charge neutrality would undermine ionic forces which would otherwise strongly bind anionic sheets in the lattice. A possible way to overcome the charge neutrality problem is to place additional negative charge on the square chalcogen sheets. However, by thus solving one difficulty we have simultaneously created another one: those additional electrons would enter square sheet states which are strongly antibonding, thus weakening the bonding between the square sheet chalcogen atoms. In the extreme case, no bonding interactions are expected between Te^{2-} ions.

In the following discussion we examine in some detail square sheets of chalcogen atoms in a variety of binary, ternary, and quaternary phases. Our goal is to assess empirically what might be the maximum negative charge which may be placed on chalcogen atoms in square sheets. Almost all chalcogen square sheets that we have looked at are susceptible to a CDW formation, a feature critical for our subsequent analysis.

12.1. Binary RES_2, $RESe_2$, and $RETe_2$ Phases

We have discussed the PbFCl structure in some detail when considering the ZrSiSe ternary phase (Figure 39a). If tetravalent Zr is replaced by trivalent Nd and, in addition, Si and Se are replaced by Te, then the $NdTe_2$ structure is obtained (Figure 43).[220, 221] This structure consists of Te square sheets as well as isolated Te atoms. The Te–Te distance within Te square sheets is 3.10 Å, a typical hypervalent Te–Te bond length (3.05 Å in hypervalent Te_5^{2-} in Cs_2Te_5.[113])

The electron count of six electrons per square sheet Si atom was established for the ZrSiSe phase $(Zr^{4+}(Si^{square})^{2-}$-$(Se^{atom})^{2-}$; see Section 11.4). When Zr is substituted by Nd, one electron is lost, which in turn is over-compensated by two electrons as Group 4 Si atoms are replaced by Group 6 Te atoms (the replacement of Se by Te is isoelectronic). The resulting assignment of charges, $Nd^{3+}(Te^{atom})^{2-}(Te^{square})^{-}$, seems to imply the existence of square sheets of main group elements with the electron count of seven electrons per atom. However, the story is not so simple. A closer look at the $NdTe_2$ crystal structure data reveals very large in-plane pancakelike parameters of anisotropic displacement for the square Te atoms, a feature seen also in the $LaTe_2$ and $CeTe_2$ crystal structures.[221, 222] The in-plane Te anisotropy, combined with the reported Te deficiency for many $RETe_2$ phases, points to possible distortions of square sheets in these compounds.[220, 223–225] These distortions are more clearly pronounced for similar rare earth diselenides, so we take a look at them first. Rare earth diselenides have been reported with various degrees of nonstoichiometry, which critically influences their corresponding crystal structures. The stoichiometric $RESe_2$ phases crystallize in a derivative of the PbFCl structure, in which the square Se sheets are distorted into a herringbone network of Se_2 pairs ($CeSe_2$[226]; $LaSe_2$[227, 228]; $PrSe_2$[229]). A schematic diagram of the distortion pathway is given below (Scheme 22). If the Se lattice were undistorted,

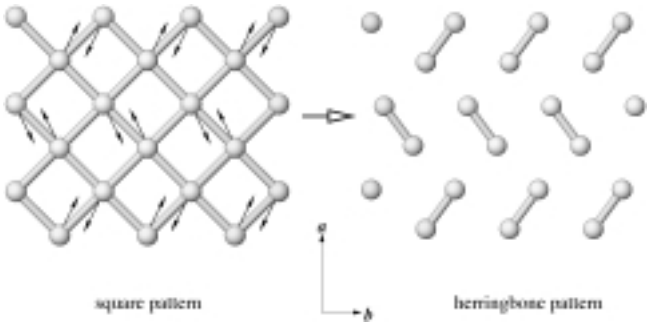

Scheme 22.

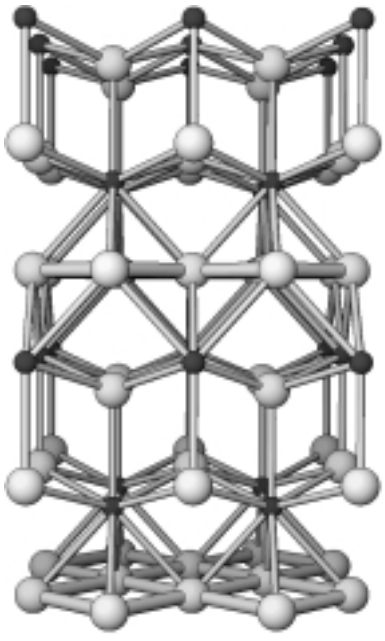

Figure 43. A perspective view of the crystal structure of $NdTe_2$ (PbFCl type). Nd = small dark spheres; Te = large light spheres.

the Se–Se distance would be a uniform 2.98 Å, while in the real herringbone lattice ($CeSe_2$[226]) there are Se–Se short intrapair (2.47 Å) and long interpair (3.06 Å, 3.06 Å, 3.40 Å) distances. Lee and Foran rationalized the Se herringbone pattern in terms of maximum HOMO–LUMO interactions between the lone pair on Se_2 (HOMO) with the Se_2 σ* orbital (LUMO).[20]

Pair formation from square Se^{-} sheets is perhaps an indication of the instability of square sheets carrying seven electrons per atom. It is remarkable that the resulting "classical" $RE^{3+}(Se^{atom})^{2-}(Se^{pair})^{-}$ compounds obey Zintl–Klemm electron counting rules. Chen and Dorhout have prepared rare earth disulfides with the same $CeSe_2$ crystal structure (RE = La, Pr).[229] As we have mentioned earlier, the crystal structures of rare earth ditellurides have been refined so as to produce undistorted square Te lattices. This, however, leads to strong in-plane anisotropies.[221, 222] DiMasi, Lee, and co-workers examined $LaTe_2$ crystals with a transmission electron microscopy, and they observed superstructure reflections corresponding to the wave vector $q = a^*/2$. Since a similar doubling of the *a* axis also occurs in the distortion of

square Se sheets to the herringbone network discussed above, the authors examined and found a general agreement between the experimental diffraction pattern and a simulated diffraction pattern resulting from a CDW similar to $LaSe_2$.[20] Consequently, their study (combined with earlier discovery of strong square Te anisotropy) points to the instability of square sheets of seven electrons per atom with respect to a CDW formation.

This conclusion is further supported by the physical property measurements on $LaTe_2$ and $CeTe_2$, carried out by Kwon and co-workers.[222, 230, 231] The electrical resistivity data indicates that $CeTe_2$ is a semimetal with "extremely low carrier concentration".[231] This picture is consistent with a CDW formation in conducting square Te sheets, which in turn would open gaps in most parts of the Fermi surface.

In summary, stoichiometric rare earth diselenides and disulfides form herringbonelike distorted square sheets, which indicates that the pair formation from a seven electron per atom square sheet is a strongly favorable process. The same conclusion applies to Te^- square sheets as demonstrated by the CDW formation in $LaTe_2$ and $CeTe_2$. The instability of square sheets carrying seven electrons per atom manifests itself in another yet way: by creating vacancies in square sheets. This subject has been discussed in some detail for the $RESe_{2-x}$ and $RETe_{2-x}$ phases by Lee and co-workers,[21, 22, 232–234] following earlier structural work.[235–237]

12.2. Binary $RETe_3$ and RE_2Te_5 Phases

The $NdTe_3$ structure may be thought of as being derived from the $NdTe_2$ structure by doubling all square Te sheets in the latter (compare Figures 43 and 44). As a result nonbonding contacts develop between neighboring square Te sheets.[238] One may assign charges to $NdTe_3$ as $Nd^{3+}(Te^{atom})^{2-}(Te_2^{square})^-$, that is, only 6.5 electrons reside in square Te sheets. Since this is intermediate between the presumably stable six electrons per atom and the unstable seven electrons per atom electron counts, one would expect a higher degree of stability from square Te sheets in $NdTe_3$.

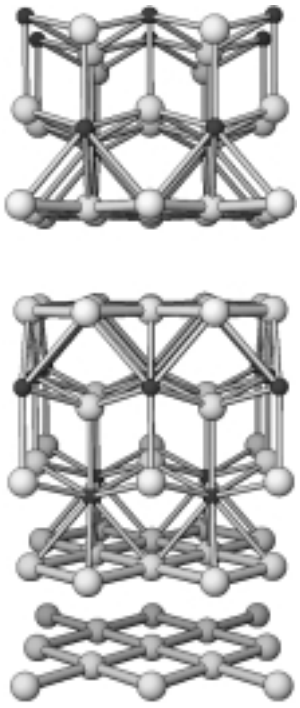

Figure 44. A perspective view of the crystal structure of $NdTe_3$. Nd = small dark spheres; Te = large light spheres.

This is indeed what happens. An X-ray structural analysis of $SmTe_3$ by Lee and co-workers indicated only a slight anisotropy of the square Te atoms, which points to a smaller amplitude of the square sheet distortion.[239] Transmission electron microscopy measurements on a number of rare earth tritellurides (RE = La, Sm, Gd, Tb, Dy, Ho, Er, Tm) demonstrated incommensurate CDW distortions in the square Te sheets, with a sinusoidal modulation of square Te atomic positions.[23] The experimentally observed superlattice wave vector agrees well with the Fermi surface nesting vector determined from extended Hückel calculations.[23] The resulting partial band gap opening was measured directly by angle-resolved photoemission spectroscopy (ARPES), which provided direct evidence of the Fermi surface nesting picture.[240] Since some of parts of the Fermi surface persist, these compounds exhibit metallic properties.[239]

Noël and Levet reported the β-UTe_3 crystal structure to be isostructural to $NdTe_3$.[241] Magnetic susceptibility measurements were consistent with a +4 oxidation state for the U atoms, which would correspond to the $U^{4+}(Te^{atom})^{2-}(Te_2^{square})^{2-}$ assignment of charges.[241] CDW distortion of the resulting square Te^- sheets was not examined, a possibility which would be anticipated from the discussion above.

Consecutive single and double square Te sheets are separated by isolated SmTe slabs in another related rare earth–Te binary phase, Sm_2Te_5. This compound may be thought of as an intergrowth of $NdTe_2$ and $NdTe_3$ crystal structures (not shown here).[239] The Sm_2Te_5 crystal structure refinement by Lee and co-workers showed that Te atoms in single square sheets were partially occupied and possessed anisotropic thermal parameters.[239] One could speculate that the metallic conductivity demonstrated by Sm_2Te_5 occurs predominantly through less-distorted double sheets of Te atoms.

The $KCuCeTe_4$ quaternary phase is also an intergrowth compound consisting of $CeTe_3$-like layers and $(CuTe^{atom})^-$ layers isolated by K^+ layers (Cu^+ is implied).[242] Charges may be assigned to the overall neutral $CeTe_3$ layer as $Ce^{3+}(Te^{atom})^{2-}(Te_2^{square})^-$, that is, 6.5 electrons per square sheet atom. Kanatzidis and co-workers found an incommensurate CDW distortion of square Te nets, which, however, does not completely destroy the Fermi surface of this material.[242]

Given the discussion above, one may draw the conclusion that an electron count of 6.5 electrons per square sheet Te atom stabilizes somewhat those square sheets, producing only small amplitude incommensurate CDW. However, strong distortions are observed in the relatively isolated square $Te^{2/3-}$ sheets in quaternary $K_{0.33}Ba_{0.67}AgTe_2$.[24] We examine this next, as well as the highly unusual zig-zag Te chain formation from defect square Te sheets found in the ternary ARE_3Te_8 series of compounds (A = K, Cs, Rb; RE = Ce, Nd).[243]

12.3. $K_{0.33}Ba_{0.67}AgTe_2$ and ARE_3Te_8 Phases

A perspective view of the $K_{0.33}Ba_{0.67}AgTe_2$ crystal structure is shown in Figure 45.[24] The layered structure consists of square Te sheets and isolated AgTe slabs sandwiched between K/Ba layers. The assignment of formal charges, $(K_{0.33})^{0.33+}(Ba_{0.67})^{1.34+}Ag^+(Te^{atom})^{2-}(Te^{square})^{0.67-}$, suggests 6.67 electrons in the square Te sheets. A remarkable feature of the $K_{0.33}Ba_{0.67}AgTe_2$ crystal structure is the isolated character of the square Te sheets which neighbor only K/Ba atoms. Thus,

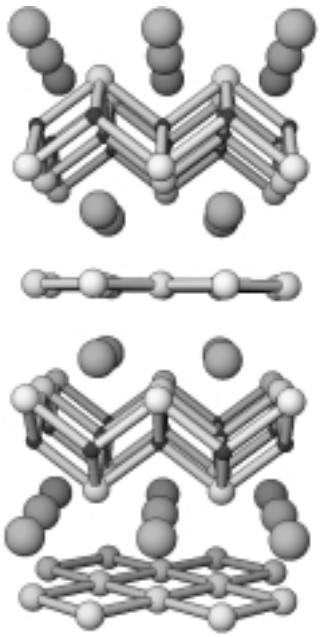

Figure 45. A perspective view of the crystal structure of $K_{0.33}Ba_{0.67}AgTe_2$. Te = medium light spheres; Ag = small light spheres; $K_{0.33}/Ba_{0.67}$ = large light spheres.

these square sheets provide a good opportunity to examine distortions of the square Te sheet free from the interference of other interactions.

The crystal structure refinement of $K_{0.33}Ba_{0.67}AgTe_2$ (carried out by Lee, Kanatzidis, and co-workers) indicated anisotropic thermal parameters for the Te atoms in the square, elongated along Te–Te bonds.[24] Electron diffraction studies revealed a CDW formation, consistent with the semiconducting nature of this compound (namely, completely destroyed Fermi surface).[24] Second moment scaled extended Hückel calculations suggested several distortion pathways; the lowest energy structure is shown in Scheme 23. The simulated diffraction pattern calculated for this distortion agreed well with the experimental one.[24] Although Te_3^{2-} trimers are engaged in strong secondary interactions which maximize their HOMO–LUMO interactions,[24] they are essentially classical Zintl–Klemm anions. It is remarkable that square Te^- sheets oligomerize into Te_2^{2-} pairs while square $Te^{2/3-}$ sheets distort into Te_3^{2-} trimers.

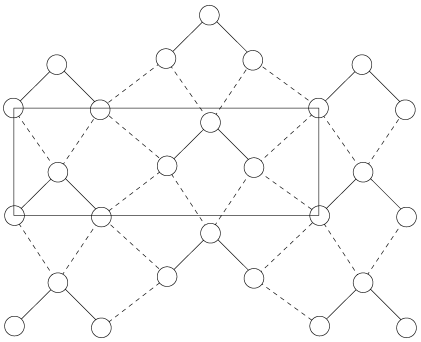

Scheme 23.

Another peculiar distortion of defect square Te sheets is observed in ARE_3Te_8 ternary phases (A = K, Cs, Rb; RE = Ce, Nd).[243] Their corresponding structures, not shown here, consists of defect $RETe_3$ layers (see Section 12.2) sandwiched between alkali cations. Te defects occur in square sheets, which leads to the assignment of charge as $A^+(RE_3)^{9+}(Te_3^{atom})^{6-}(Te_5^{square})^{4-}$. The authors were able to refine further the Te positions in distorted square sheets, which produced the superstructure shown in Figure 46. This

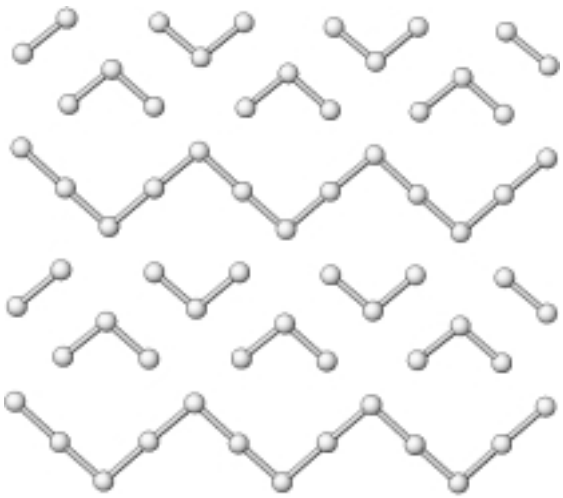

Figure 46. The defect-distorted square Te lattice in KNd_3Te_8.

square lattice distortion was predicted earlier by Lee and coworkers on theoretical grounds.[232]

Defect square Te_5^{4-} sheets in ARE_3Te_8 break into Te_3^{2-} classical trimers and infinite zig-zag Te_2^{2-} chains (see Figure 46). We examine the electron counting in the latter zig-zag chains using the following simple arguments: Te zig-zag chains consist of two types of Te atoms—those having bent and linear local geometries. Two-connected bent Te atoms are classical, thus, carry six electrons (no charge). Two-connected linear Te atoms should be compared to Xe (as in XeF_2), therefore, they carry a -2 charge. On adding up the charges on two Te atoms one arrives at the Te_2^{2-} formulation, which agrees with the experimental assignment of charges. The semiconducting behavior of these compounds is consistent with the strongly distorted nature of square Te sheets.

Square $Te^{2/3-}$ sheets in $K_{0.33}Ba_{0.67}AgTe_2$ are strongly distorted into classical Te_3^{2-} trimers, which demonstrate semiconducting properties. Defect square Te_5^{4-} sheets in the ARE_3Te_8 series of compounds are also oligomerized into Te_3^{2-} classical trimers and unusual infinite zig-zag Te_2^{2-} chains. The electron count in the latter may be derived by taking into account the local bonding environment of Te atoms. Considering all the experimental evidence, one is led to believe that square sheets with an electron count of more than 6.5 electrons per atom are highly unstable with respect to a CDW formation.

12.4. Summary

One has to apply our electron counting scheme to chalcogen square sheets with caution, since six electrons per atom chalcogen atoms would have a neutral charge. Such neutrality would provide minimal interactions of these sheets to the surrounding cationic lattice. If additional negative charge is placed on square sheets, then a significant strengthening of ionic interactions is expected, at the cost of populating antibonding states of the square chalcogen sheet. The interplay between the latter two competing forces determines the narrow range of electron counts for which undistorted square sheets of chalcogen atoms are known to exist.

By analyzing compounds containing mononegative square chalcogen sheets one may draw a conclusion that these sheets are highly unstable with respect to formation of a classical dichalcogen pair. This is explicitly seen for stoichiometric rare earth diselenides and disulfides, in which case a herringbone network of Se_2^{2-} (S_2^{2-}) pairs is found. While undistorted square sheets are expected to be metallic, the latter compounds are semiconducting, which points to complete opening of the Fermi gap. Stoichiometric rare earth ditellurides are subject to CDW formation with presumably the same herringbone pattern structure, as demonstrated for $LaTe_2$.

Nonstoichiometric rare earth diselenides and ditellurides contain defective square sheets, which are strongly distorted into classical pairs and chalcogen atoms. These species are engaged in strong secondary contacts with each other, maximizing the interactions between the lone pair (HOMO) and the σ* orbital (LUMO). As we have explained elsewhere, there is a continuum of bonding between hypervalent electron-rich three-center bonding—so called "secondary interactions"—and donor–acceptor frontier orbital interaction.[59] All these compounds are semiconducting, which confirms Fermi gap opening caused by distortion of the square sheet.

Square Te sheets carrying only 6.5 electrons per atom are found in rare earth tritellurides. Although these sheets are also subject to CDW distortion, the latter turns out to be only a small amplitude sinusoidal modulation of the Te atomic positions of the square sheet. The directly measured Fermi surface of $SmTe_3$ demonstrates incomplete Fermi surface nesting, as also evidenced by its metallic properties.

The square $Te^{2/3-}$ sheets found in quaternary $K_{0.33}Ba_{0.67}AgTe_2$ are strongly distorted into classical Te_3^{2-} trimers, which suggests that the electron count over 6.5 electrons per atom causes square Te sheets to distort. Its semiconducting behavior is in agreement with this conclusion. Classical Te_3^{2-} trimer formation is also seen in defective square Te_5^{4-} sheets, found in the ARE_3Te_8 series of compounds. Another structural motif obtained from distortion of the square sheet in these compounds is an unusual infinite Te_2^{2-} zig-zag chain. The electron count in the zig-zag Te_2^{2-} chains may be rationalized by comparing local coordination of bent and linear two-connected Te atoms to molecular analogues.

Our survey of square chalcogen sheets strongly suggests the upper limit of 6.5 electrons per square sheet atom as a condition of undistorted square sheet stability. More negatively charged square chalcogen sheets oligomerize into both classical species as well as nonclassical ones (zig-zag Te_2^{2-} chains in ARE_3Te_8). On the other hand no neutral or cationic square chalcogen sheets are known, as expected from simple electrostatic and electronegativity arguments. Taking into account the earlier discussion on square sheets of Sb and Group 4 elements, we believe that the stability zone for square sheet electron counts lies between 5.5 and 6.5 electrons per atom.

13. Summary and Outlook

Heavy late main group elements tend to form unusual, if sometimes geometrically simple, extended low-dimensional networks which just do not occur "normally" in molecules. In this paper we have carried through a systematic analysis of electron-rich multi-center extended structures aimed at deriving unambiguous electron counting schemes for various topologies. In particular we looked at a linear 1D chain (seven electrons per atom), a square sheet (six electrons peratom), a cubic lattice (five electrons per atom), an 1D ladder (six electrons per atom), a 1D X_3 strip (20 electrons per three atoms), and a number of more complex networks derived from these building blocks. We also exemplified the use of these building blocks in an aufbau of more complex structures.

We have also outlined the reasons and the possible pathways of the Peierls distortions for some of these networks. Relatively weak s-p mixing for heavier main group elements, caused by the contraction of less-screened s orbitals, is one of the main reasons behind the existence of their low-dimensional Peierls-undistorted metallic networks. In contrast, we think that strong s-p mixing for light elements (for example N) makes their Peierls distortion extremely favorable, thus excluding, for instance, the possibility of the existence of hypervalent networks of N.

Combined with classical Zintl–Klemm electron counting, the hypervalent electron counting scheme derived here may be successfully applied to understand the electronic structures of a large variety of Sb compounds. Linear Sb^{2-} chains, square Sb^- sheets, and other nonclassical networks are found in a great number of seemingly unrelated Sb phases. Indeed, we have yet to encounter an Sb phase which is in a clear violation of the proposed electron counting scheme.

Actually, because of the fractional filling of hypervalent bands in these networks, we expect the numbers of electrons derived for each network to vary a little. Linear chains of elements other than Sb also indicate that seven electrons per linear chain atom is a preferred electron count; however, some linear chains have electron count of 7.25 electrons per atom. Interestingly enough, this simple linear chain electron count serves successfully as a good starting point for rationalizing the electronic structure of a nontrivial three-dimensional network, that is found in the Tl_4SnTe_3 series of compounds.

We have also examined in great detail square sheets of Group 4 and Group 6 elements. In the former case, the preferred electron count is clearly six electrons per square sheet atom. However, some square sheets of Group 4 elements are also realized with lesser electron counts of 5.5 and 5 electrons per atom, in which case secondary interactions develop between "electronically unsaturated" square sheets and other anionic subnetworks.

Six electrons per square sheet atom would render chalcogen atoms neutral, not an advantage in an anionic atmosphere. Consequently, one expects somewhat negative square chalcogen sheets to be more stable. Most of the square chalcogen sheets carrying seven electrons per square sheet atom are severely distorted into classical dichalcogen pairs (for example the Se_2^{2-} herringbone network in $LaSe_2$). The strong tendency to form defect square sheets as well as the persistence of CDW distortions also emphasizes the intrinsic instability of square sheets carrying seven electrons per atom. It appears that 6.5 electrons per chalcogen atom in the square sheets, as found in rare earth tritellurides, are less distorted,

although a small amplitude CDW formation is still observed. It is quite remarkable that in an aufbau using both classical and hypervalent building blocks, it has been possible to make sense of bonding in nontrivial intermetallic compounds as complex as $La_{12}Mn_2Sb_{30}$. We hope that with the help of the hypervalent building blocks discussed in this paper, many other intermetallic compounds of heavy late main group elements may be successfully studied as well.

14. Appendix I: Computational Details

All calculations were performed with the help of "Yet Another extended Hückel Molecular Orbital Package (YAeHMOP)", a program developed in our group by G. Landrum.[244] The standard atomic parameters were used for Sb, N, and Zr. The parameters are listed in Table 8 with the corresponding references.

Table 8. Extended Hückel parameters. The ζ values are the exponents of the Slater orbital basis set, the c_i values the coefficients in a double-ζ expansion.

Atom	Orbital	H_{ii} [eV]	ζ_1	c_1	ζ_2	(c_2)	Ref.
Sb	5s	– 18.8	2.323				[268]
	5p	– 11.7	1.999				
N	2s	– 26.0	1.95				[77]
	2p	– 13.4	1.95				
Zr	5s	– 9.87	1.817				[269]
	5p	– 6.76	1.776				
	4d	– 11.18	3.835	0.6210	1.505	0.5769	

Addendum

While this manuscript was in press we learned that Stöwe had found that TlTe undergoes a rather peculiar Pierls distortion at 172 K, where only half of the chains with "handles" are affected.[270] The pairing distortion indicates the preservation of the band structure patterns of the underlying simple linear chain in the composite chain. Stöwe has also offered direct structural evidence of the square Te sheet distortion in $LaTe_2$ and $PrTe_2$.[271] This observation is consistent with the instability of the electron count of seven electrons per atom in a square sheet, as advocated throughout this review.

We thank many former and current members of our research group, in particular, Norman Goldberg, Dong-Kyun Seo, Grigori Vajenine and Peter Kroll for helpful discussions. We also express our gratitude to Greg Landrum, Arthur Mar, and Stephen Lee for reading this manuscript and suggesting improvements. Hans Georg von Schnering made many important suggestions to us in the course of reviewing our paper. We gratefully acknowledge the National Science Foundation for its generous support of this work by Research Grant CHE-9970089 and the Cornell Theory Center for computer time. Drawings of all crystal structures were produced with the "Atoms 3.1" software package.

Received: July 6, 1999 [A 352]

[1] E. Zintl, *Angew. Chem.* **1939**, 52, 1.
[2] *Chemistry, Structure, and Bonding of Zintl Phases and Ions* (Ed.: S. M. Kauzlarich), VCH, New York, **1996**.
[3] H. Schäfer, B. Eisenmann, W. Müller, *Angew. Chem.* **1973**, *85*, 742; Ang*ew. Chem. Int. Ed.* **1973**, *12*, 694.
[4] A. Simon, *J. Solid. State Chem.* **1985**, *57*, 2.
[5] S. Lee, L. Hoistad, *J. Alloys Comp.* **1995**, *229*, 66.
[6] U. Häussermann, R. Nesper, *J. Alloys Comp.* **1995**, *218*, 244.
[7] K. Wade, *Inorg. Chem. Radiochem.* **1976**, *18*, 1.
[8] D. P. Mingos, D. J. Wales, *Introduction To Cluster Chemistry*, Prentice Hall, Englewood Clis, NJ, USA, **1990**.
[9] C. Zheng, R. Hoffmann, *Z. Naturforsch. B* **1986**, *41*, 292.
[10] C. Belin, M. Tillard-Charbonnel, *Prog. Solid State Chem.* **1993**, *22*, 59.
[11] R. Nesper, *Angew. Chem.* **1991**, *103*, 806; *Angew. Chem. Ed. Engl.* **1991**, *30*, 789.
[12] M. Brylak, W. Jeitschko, *Z. Naturforsch. B* **1994**, *49*, 747.
[13] M. Brylak, M. H. Möller, W. Jeitschko, *J. Solid State Chem.* **1995**, *115*, 305.
[14] R. Nesper, *Prog. Solid State Chem.* **1990**, *20*, 1.
[15] W. Müller, *Z. Naturforsch. B* **1977**, *32*, 357.
[16] T. Albright, J. Burdett, M.-H. Whangbo, *Orbital Interactions in Chemistry*, Wiley, New York, **1985**.
[17] R. Hoffmann, *A Chemist's View of Bonding in Extended Structures*, VCH, New York, **1988**.
[18] R. E. Peierls, *Quantum Theory of Solids*, Oxford University Press, London, **1955**.
[19] W. Tremel, R. Hoffmann, *J. Am. Chem. Soc.* **1987**, *109*, 124.
[20] E. DiMasi, B. Foran, M. C. Aronson, S. Lee, *Phys. Rev. B* **1996**, *54*, 12587.
[21] S. Lee, B. Foran, *J. Am. Chem. Soc.* **1996**, *118*, 9139.
[22] E. DiMasi, M. C. Aronson, B. Foran, S. Lee, *Physica B* **1995**, *206/207*, 386.
[23] E. DiMasi, M. C. Aronson, J. F. Mansfield, B. Foran, S. Lee, *Phys. Rev. B* **1995**, *52*, 14516.
[24] X. Zhang, J. Li, B. Foran, S. Lee, H.-Y Guo, T. Hogan, C. R. Kannewurf, M. G. Kanatzidis, *J. Am. Chem. Soc.* **1995**, *117*, 10513.
[25] N. Tokitoh, Y. Arai, T. Sasamori, R. Okazaki, S. Nagase, H. Uekusa, Y. Ohashi, *J. Am. Chem. Soc.* **1998**, *120*, 433.
[26] R. Hoffmann, *Am. Sci.* **1991**, *79*, 11.
[27] If one π bond is included in the Sb four-ring, then the corresponding electron count diminishes by two. In this treatment we neglect the possibility of π bonding between Sb atoms, a position justified by the extreme rearness of Sb–Sb π bonds.
[28] N. N. Zuravlev, G. S. Zhdanov, *Sov. Phys. Crystallogr.* **1956**, *1*, 404.
[29] S. Rundqvist, N. O. Ersson, *Ark. Kemi* **1968**, *30*, 103.
[30] D. J. Braun, W. Jeitschko, *J. Less-Common Met.* **1980**, *72*, 147.
[31] C. B. H. Evers, W. Jeitschko, L. Boonk, D. J. Braun, T. Ebel, U. D. Scholz , *J. Alloys Comp.* **1995**, *224*, 184.
[32] D. Jung, M.-H. Whangbo, S. Alvarez, *Inorg. Chem.* **1990**, *29*, 2252.
[33] T. Schmidt, G. Kliche, H. D. Lutz, *Acta Cristallogr. Sec. C* **1987**, *43*, 1678.
[34] F. Grandjean, A. Gèrard, D. J. Braun, W. Jeitschko, *J. Phys. Chem. Solids* **1984**, *45*, 877.
[35] G. P. Meisner, M. S. Torikachvili, K. N. Yang, M. B. Maple, R. P. Guertin, *J. Appl. Phys.* **1985**, *57*, 3073.
[36] B. Eisenmann, H. Jordan, H. Schäfer, *Z. Naturforsch. B* **1985**, *40*, 1603.
[37] G. Chapius, F. Hulliger, R. Schmelczer, *J. Solid. State Chem.* **1980**, *31*, 59.
[38] B. Eisenmann, *Z. Naturforsch. B* **1979**, *34*, 1162.
[39] W. Hönle, H. G. von Schnering, *Z. Kristallogr.* **1981**, *155*, 307.
[40] F. Hulliger, R. Schmelczer, *J. Solid State Chem.* **1978**, *26*, 389.
[41] N. W. Alcock, *Adv. Inorg. Radiochem.* **1972**, 15, 1.
[42] G. A. Landrum, R. Hoffmann, *Angew. Chem.*, in press.
[43] K. Deller, B. Eisenmann, *Z. Naturforsch. B* **1978**, *33*, 676.
[44] C. S. Barrett, P. Cucka, K. Haefner, *Acta Crystallogr.* **1963**, *16*, 451.
[45] L. F. Vereshchagin, S. S. Kobalkina, *Sov. Phy. JETP (Engl. Transl.)* **1965**, *20*, 274.
[46] D. Akhtar, V. D. Vankar, T. C. Goel, K. L. Chopra, *J. Mater. Sci.* **1979**, *14*, 988.
[47] J. K. Burdett, S. Lee, *J. Am. Chem. Soc.* **1983**, *105*, 1079.
[48] G. Cordier, H. Schäfer, M. Stelter, *Z. Anorg. Allg. Chem.* **1984**, *519*, 183.

[49] A. Rehr, S. M. Kauzlarich, *J. Alloys Comp*. **1994**, *207*, 424.
[50] R. F. Gallup, C. Y. Fong, S. M. Kauzlarich, *Inorg. Chem*. **1992**, *31*, 115.
[51] S. M. Kauzlarich, M. M. Thomas, D. A. Odink, M. M. Olmstead, *J. Am. Chem. Soc*. **1991**, *113*, 7205.
[52] R. E. Rundle, *J. Am. Chem. Soc*. **1963**, *85*, 112.
[53] R. E. Rundle, *J. Am. Chem. Soc*. **1979**, *101*, 5057.
[54] G. C. Pimentel, *J. Chem. Phys*. **1951**, *19*, 446.
[55] J. I. Musher, *Angew. Chem*. **1969**, *81*, 68; *Angew. Chem. Int. Ed. Engl*. **1969**, *8*, 54.
[56] M. Häser, *J. Am. Chem. Soc*. **1996**, *118*, 7311.
[57] The octahedral symmetry introduces some special features, which cause one to think about degrees of hypervalency: G. A. Landrum, H. B. Bürgi, R. Hoffmann, T. Ward, unpublished results.
[58] M. J. Ferguson, R. W. Hushagen, A. Mar, *J. Alloys Comp*. **1997**, *249*, 191.
[59] G. A. Landrum, N. Goldberg, R. Hoffmann, *J. Chem. Soc. Dalton Trans*. **1997**, 3605.
[60] P. Pyykkö, *Chem. Rev*. **1997**, *97*, 597.
[61] B. R. Wang, R. Bodnar, H. Steinfink, *Inorg. Chem*. **1966**, *5*, 1468.
[62] P. C. Canfield, J. D. Thompson, Z. Fisk, *J. Appl. Phys*. **1991**, *70*, 5992.
[63] E. Brechtel, G. Cordier, H. Schäfer, *J. Less-Common Met*. **1981**, *79*, 131.
[64] G. Cordier, H. Schäfer, P. Woll, *Z. Naturforsch. B* **1985**, *40*, 1097.
[65] O. Sologub, K. Hiebl, P. Rogl, H. Noël, O. Bodak, *J. Alloys Comp*. **1994**, *210*, 153.
[66] A. Leithe-Jasper, P. Rogl, *J. Alloys Comp*. **1994**, *203*, 133.
[67] O. Sologub, H. Noël, A. Leithe-Jasper, P. Rogl, *J. Solid State Chem*. **1995**, *115*, 441.
[68] O. Sologub, K. Hiebl, P. Rogl, O. Bodak, *J. Alloys Comp*. **1995**, *227*, 40.
[69] P. Wollesen, W. Jeitschko, M. Brylak, L. Dietrich, *J. Alloys Comp*. **1996**, *245*, L5.
[70] H. Flandorfer, O. Sologub, C. Godart, K. Hiebl, A. Leithe-Jasper, P. Rogl, H. Noël, *Solid State Commun*. **1996**, *97*, 561.
[71] O. Sologub, M. Vybornovand, P. Rogl, K. Hiebl, G. Cordier, P. Woll, *J. Solid. State Chem*. **1996**, *122*, 262.
[72] H. Holseth, A. Kjekshus, *Acta Chem. Scand*. **1968**, *22*, 3273.
[73] H. Holseth, A. Kjekshus, *J. Less-Common Met*. **1968**, *16*, 472.
[74] T. Siegrist, F. Hulliger, *J. Solid. State Chem*. **1986**, *63*, 23.
[75] G. Bruzzone, G. B. Bonino, *Atti. Accad. Naz. Lincei Cl. Sci. Fis. Mat. Nat. Rend.* **1970**, *48*, 235.
[76] C. B. Showmaker, D. P. Shoemaker, *Acta Crystallogr*. **1965**, *18*, 900.
[77] R. Hoffmann, *J. Chem. Phys*. **1963**, *39*, 1397.
[78] R. Hoffmann, *J. Chem. Phys*. **1964**, *40*, 2745.
[79] R. Hoffmann, *J. Chem. Phys*. **1964**, *40*, 2474.
[80] L. L. Lohr, *Inorg. Chem*. **1987**, *26*, 2005.
[81] T. Albright, J. Burdett, M.-H. Whangbo, *Orbital Interactions in Chemistry*, Wiley, New York, **1985**, chap. 12.
[82] R. J. Gillespie, *Molecular Geometry*, Van Nostrand-Reinhold, London, **1972**.
[83] P. Cherin, P. Unger, *Acta Cristallogr*. **1967**, *23*, 670.
[84] J. Burdett, *Chemical Bonding In Solids*, Oxford University Press, New York, **1995**.
[85] D. A. Keszler, R. Hoffmann, *J. Am. Chem. Soc*. **1987**, *109*, 118.
[86] R. Hoffmann, C. Janiak, C. Kollmar, *Macromolecules* **1991**, *24*, 3725.
[87] H. Genin, R. Hoffmann, *J. Am. Chem. Soc*. **1995**, *117*, 12328.
[88] J. K. Burdett, *Prog. Solid State Chem*. **1984**, *15*, 173.
[89] E. Canadell, M.-H. Whangbo, *Chem. Rev*. **1991**, *91*, 965.
[90] M.-H. Whangbo, E. Canadell, P. Foury, J.-P. Pouget, *Science* **1991**, *252*, 96.
[91] M.-H. Whangbo, E. Canadell, *J. Am. Chem. Soc*. **1992**, *114*, 9587.
[92] "Looking At Chemistry Through The Unifying Lens Of Molecular Orbital Theory: From Extended Hypervalent Bonding To Hydrocarbon Chemisorption And The Reactivity Of Organic Molecules": G. A. Papoian, PhD thesis, Cornell University, Ithaca, NY, USA, **1999**.
[93] A. Imamura, *Mol. Phys*. **1968**, *15*, 225.
[94] M.-H. Whangbo in *Computational Theoretical Organic Chemistry* (Eds.: I. G. Csizmadia, R. Daudel), Reidel, Boston, **1981**, p. 233.
[95] C. Froese Fischer, *At. Data* **1972**, *4*, 301.
[96] S. Lee, *J. Am. Chem. Soc*. **1991**, *113*, 8611.
[97] W. Kutzelnigg, *Angew. Chem*. **1984**, 96, 262; *Angew. Chem. Int. Ed. Engl*. **1984**, 23, 272.
[98] D.-K. Seo, R. Hoffmann, unpublished results.
[99] G. Papoian, R. Hoffmann, *J. Solid State Chem*. **1998**, *139*, 8.
[100] R. Jaggi, *Helv. Phys. Acta* **1964**, *37*, 618.
[101] T. Chattopadhyay, J. X. Boucherle, H. G. von Schnering, *J. Phys. C* **1987**, *20*, 1431.
[102] T. Chattopadhyay, R. P. Santandrea, H. G. von Schnering, *J. Phys. Chem. Solids* **1985**, *46*, 351.
[103] T. Chattopadhyay, J. Pannetier, H. G. von Schnering, *J. Phys. Chem. Solids* **1986**, *47*, 879.
[104] H. G. von Schnering, H. Wiedemeier, *Z. Kristallogr.* **1981**, *156*, 143.
[105] E. Garcia, J. D. Corbett, *J. Solid State Chem*. **1988**, *73*, 452.
[106] A. Kjekshus, *Acta Chem. Scand*. **1972**, *26*, 1633.
[107] E. Garcia, J. D. Corbett, *J. Solid State Chem*. **1988**, *73*, 440.
[108] W. S. Sheldrick, M. Wachhold, *Angew. Chem*. **1995**, *107*, 490; *Angew. Chem. Int. Ed. Engl*. **1995**, *34*, 450.
[109] W. S. Sheldrick, M. Wachhold, *Chem. Commun*. **1996**, 607.
[110] G. A. Papoian, R. Hoffmann, unpublished results.
[111] K. Anderko, K. Schubert, *Z. Metallkd.* **1954**, *45*, 371.
[112] R. V. Baranova, Z. G. Pinsker, *Sov. Phys. Crystallogr. (Engl. Transl.)* **1964**, *9*, 83.
[113] P. Böttcher, U. Kretschmann, *Z. Anorg. Allg. Chem*. **1982**, *491*, 39.
[114] I. Schewe-Miller, P. Böttcher, *Z. Kristallogr.* **1991**, *196*, 137.
[115] Yu. V. Voroshilov, M. I. Gurzan, Z. Z. Kish, L. V. Lada, *Inorg. Mater. (Engl. Transl.)* **1988**, *24*, 1265.
[116] P. Böttcher, T. Doert, C. Druska, S. Bradtmöller, *J. Alloys Comp*. **1997**, *246*, 209.
[117] K. J. Nordell, G. J. Miller, *J. Alloys Comp*. **1996**, *241*, 51.
[118] A. J. K. Haneveld, F. Jellinek, *J. Less-Common Met*. **1970**, *21*, 45.
[119] K. Stöwe, *J. Solid State Chem*. **1996**, *127*, 202.
[120] H. P. Beck, W. Dausch, *Z. Naturforsch. B* **1988**, *43*, 1547.
[121] V. K. Slovyanskikh, N. T. Kuznetsov, N. V. Gracheva, *Russ. J. Inorg. Chem. (Engl. Transl.)* **1985**, *30*, 314.
[122] A. J. K. Haneveld, F. Jellinek, *J. Less-Common Met*. **1971**, *24*, 229.
[123] S. Furuset, H. Fjellvag, *Acta Chem. Scand*. **1991**, *45*, 694.
[124] K. Stöwe, F. R. Wagner, *J. Solid State Chem*. **1998**, *138*, 160.
[125] K.-S. Choi, R. Patschke, J. L. Billinge, M. J. Waner, M. Dantus, M. G. Kanatzidis, *J. Am. Chem. Soc*. **1998**, *120*, 10706.
[126] J. A. Cody, J. A. Ibers, *Inorg. Chem*. **1996**, *35*, 3836.
[127] E. J. Wu, M. A. Pell, J. A. Ibers, *J. Alloys Comp*. **1997**, *255*, 106.
[128] A. A. Narducci, J. A. Ibers, *Inorg. Chem*. **1998**, *37*, 3798.
[129] O. Tougait, A. Daoudi, M. Potel, H. Noël, *Mater. Res. Bull.* **1997**, *32*, 1239.
[130] N.-H. Dung, M.-P. Pardo, P. Boy, *Acta Cristallogr. Sec. C* **1983**, *39C*, 668.
[131] F. Q. Huang, S. Lee, W. Choe, C. Auriel, *Inorg. Chem*., submitted.
[132] T. Yamauchi, S. Zaima, K. Mizuno, H. Kitamura, Y. Koide, Y. Yasuda, *J. Appl. Phys*. **1991**, *69*, 7050.
[133] M. Setton, J. Van der Spiegel, *J. Appl. Phys*. **1991**, *70*, 193.
[134] T. Yamauchi, S. Zaima, K. Mizuno, H. Kitamura, Y. Koide, Y. Yasuda, *Appl. Phys. Lett*. **1990**, *57*, 1105.
[135] A. Bourret, F. M. d'Heurle, F. K. Le Goues, A. Charai, *J. Appl. Phys*. **1990**, *67*, 241.
[136] H. Schachner, H. Nowotny, H. Kudielka, *Monatsh. Chem*. **1954**, *85*, 1140.
[137] J. F. Smith, D. M. Bailey, *Acta Crystallogr*. **1957**, *10*, 341.
[138] P. G. Cotter, J. A. Kohn, A. Potter, *J. Am. Ceram. Soc*. **1956**, *39*, 11.
[139] O. G. Karpinskiy, B. A. Evseyev, *Russ. Metall. (Engl. Transl.)* **1969**, *3*, 128.
[140] A. Brown, *Acta Crystallogr*. **1962**, *15*, 652.
[141] A. Brown, *Acta Crystallogr*. **1961**, *14*, 860.
[142] S. Cirafici, A. Palenzona, P. Manfrinetti, *J. Less-Common Met*. **1983**, *90*, 49.
[143] A. E. Dwight, *Argonne Nat. Lab. Rep. ANL* **1982**, 1.
[144] M. V. Rudometkina, Yu. D. Seropegin, A. V. Griobanov, L. S. Gusei, *J. Less-Common Met*. **1989**, *147*, 239.
[145] E. S. Makarov, V. N. Bykov, *Kristallografiya* **1959**, *4*, 164.
[146] H. Boller, H. Nowotny, A. Wittmann, *Monatsh. Chem*. **1960**, *91*, 1174.
[147] H. Nowotny, H. Schachner, *Monatsh. Chem*. **1953**, *84*, 169.
[148] P. Villars, K. Mathis, F. Hullinger in *The Structures of Binary Compounds, Vol. 2* (Eds: F. R. de Boer, D. G. Pettifor), North-Holland, Amsterdam, **1989**, chap. 1.

[149] P. Villars, *J. Less-Common Met*. **1984**, *99*, 33.
[150] J. Evers, G. Oehlinger, A Weiss, F. Hulliger, *J. Less-Common Met*. **1983**, *90*, L19.
[151] R. Nesper, H. G. von Schnering, J. Curda, *Solid Compounds of Transition Elements VI, International Conference* (Stuttgart, Germany) **1979**, p. 150.
[152] J. Evers, *J. Solid. State Chem*. **1979**, *28*, 369.
[153] J. Evers, G. Oehlinger, A Weiss, *J. Solid. State Chem.* **1977**, *20*, 173.
[154] K. Janzon, H. Schäfer, A Weiss, *Angew. Chem*. **1965**, *77*, 258; *Angew. Chem. Int. Ed. Engl*. **1965**, *4*, 245.
[155] *CRC Handbook of Chemistry and Physics*, 79th ed. (Ed.: D. R. Lide), CRC Press, Washington, DC, USA **1979**.
[156] A. Iandelli, A. Palenzona, *Atti Accad. Naz. Lincei Cl. Sci. Fis. Mat. Nat. Rend*. **1966**, *40*, 623.
[157] F. A. Schidt, O. D. McMasters, O. N. Carlson, *J. Less-Common Met*. **1972**, *26*, 53.
[158] I. Mayer, Y. Eshdat, *Inorg. Chem*. **1968**, *7*, 1904.
[159] I. Mayer, E. Yanir, I. Schidlovsky, *Inorg. Chem*. **1967**, *6*, 842.
[160] I. Binder, *J. Am. Ceram. Soc*. **1960**, *43*, 287.
[161] A. Iandelli, A. Palenzona, G. L. Olcese, *J. Less-Common Met*. **1979**, *64*, 213.
[162] J. Pierre, B. Lambert-Andron, J. L. Soubeyroux, *J. Magn. Magn. Mater*. **1989**, *81*, 39.
[163] P. Schobinger-Papamantellos, D. B. De Mooij, K. H. J. Buschow, *J. Magn. Magn. Mater*. **1989**, *79*, 231.
[164] G. Borzone, A. Borsese, R. Ferro, *Z. Anorg. Allg. Chem*. **1983**, *501*, 199.
[165] G. Borzone, A. Borsese, R. Ferro, *J. Less-Common Met*. **1982**, *85*, 195.
[166] F. Weitzer, K. Hiebl, P. Rogl, *J. Solid. State Chem*. **1992**, *98*, 291.
[167] F. Weitzer, K. Hiebl, P. Rogl, *Solid State Commun*. **1992**, *82*, 353.
[168] A. Palenzona, P. Manfrinetti, *J. Alloys Comp*. **1993**, *201*, 43.
[169] E. I. Gladyshevskii, *J. Struct. Chem. (Engl. Transl.)* **1964**, *5*, 523.
[170] K. Sekizawa, *J. Phys. Soc. Jpn*. **1966**, *21*, 274.
[171] P. Schobinger-Papamantellos, D. B. De Mooij, K. H. J. Buschow, *J. Less-Common Met*. **1988**, *144*, 265.
[172] V. N. Eremenko, K. A. Meleshevich, Yu. I. Buyanov, P. S. Martensyuk, *Poroshk. Metall. (Kiev)* **1989**, *28*, 543.
[173] V. N. Eremenko, X. Q. Che, Yu. I. Buyanov, A. M. Khar'kova, *Inorg. Mater. (Engl. Transl.)* **1975**, *11*, 133.
[174] J. Perry, I. Binder, B. Post, *J. Phys. Chem*. **1959**, *63*, 616.
[175] J. Perry, E. Banks, B. Post, *J. Phys. Chem*. **1959**, *63*, 2073.
[176] A. Iandelli, A. Palenzona in *Handbook of the Physics and Chemistry of Rare Earths*, *Vol. 2* (Eds.: K. A. Gscheidner, Jr., L. Eyring), North-Holland, Amsterdam, **1979**, chap. 13.
[177] J. Pierre, E. Slaud, D. Frachon, *J. Less-Common Met*. **1988**, *139*, 321.
[178] S. Lee, *J. Am. Chem. Soc*. **1991**, *113*, 101.
[179] G. V. Vajenine, R. Hoffmann, *J. Am. Chem. Soc*. **1998**, *120*, 4200.
[180] G. A. Papoian, M. D. Bojin, R. Hoffmann, unpublished results.
[181] V. V. Pavlyuk, O. I. Bodak, V. K. Pecharskii, R. V. Skolozdra, E. I. Gladyshevskii, *Inorg. Mater. (Engl. Transl.)* **1989**, *25*, 962.
[182] W. Dörrscheidt, G. Savelsberg, J. Stöhr, H. Schäfer, *J. Less-Common Met*. **1982**, *83*, 269.
[183] L. V. Krivulya, O. I. Bodak, Yu. K. Gorelenko, *Inorg. Mater. (Engl. Transl.)* **1986**, *22*, 1685.
[184] G. Venturini, B. Malaman, M. Meot-Meyer, D. Fruchart, G. Le Caer, D. Malterre, B. Roques, *Rev. Chim. Miner.* **1986**, *23*, 162.
[185] V. K. Pecharsky, K. A. Gschneidner, Jr., L. L. Miller, *Phys. Rev. B* **1991**, *43*, 10906.
[186] W. Bazela, J. Leciejewicz, K. Maletka, A. Szytula, *J. Magn. Magn. Mater*. **1992**, *109*, 305.
[187] H. Kumigashira, A. Chainani, T. Yokoya, O. Akaki, T. Takahashi, M. Ito, M. Kasaya, O. Sakai, *Phys. Rev. B* **1996**, *53*, 2565.
[188] P. Schobinger-Papamantellos, K. H. J. Buschow, C. Wilkinson, F. Fauth, C. Ritter, *J. Magn. Magn. Mater*. **1998**, *189*, 214.
[189] D. M. Proserpio, G. Chacon, C. Zheng, *Chem. Mater*. **1998**, *10*, 1286.
[190] E. Parté, B. Chabot in *Handbook of the Physics and Chemistry of Rare Earths*, *Vol. 6* (Eds.: K. A. Gscheidner, Jr., L. Eyring), Elsevier Science, Amsterdam, **1984**, chap. 48.
[191] P. Rogl in in *Handbook of the Physics and Chemistry of Rare Earths*, *Vol. 7* (Eds.: K. A. Gscheidner, Jr., L. Eyring), Elsevier Science, Amsterdam, **1984**, chap. 51.
[192] H. Onken, K. Vierheilig, H. Hahn, *Z. Anorg. Allg. Chem*. **1964**, *333*, 267.
[193] W. Tremel, R. Hoffmann, *J. Am. Chem. Soc*. **1987**, *109*, 124.
[194] R. Ferro, *Acta Crystallogr*. **1955**, *8*, 360.
[195] R. Ferro, *Acta Crystallogr*. **1956**, *9*, 817.
[196] R. Ferro, *Acta Crystallogr*. **1957**, *10*, 476.
[197] V. Johnson, W. Jeitschko, *J. Solid. State Chem*. **1973**, *16*, 306.
[198] F. Hulliger, *J. Less-Common Met*. **1973**, *30*, 397.
[199] A. J. Klein Haneveld, F. Jellinek, *Recl. Trav. Chim. Des Pays-Bas* **1964**, *83*, 776.
[200] A. J. Klein Haneveld, F. Jellinek, *J. Less-Common Met*. **1969**, *18*, 123.
[201] V. Johnson, W. Jeitschko, *J. Solid State Chem*. **1974**, *11*, 161.
[202] L. S. Andrukhiv, L. O. Lysenko, Ya. P. Yarmolyuk, E. I. Hladyshevsky, *Dopov. Akad. Nauk Ukr. RSR Ser. A* **1975**, *7*, 645.
[203] H. Sprenger, *J. Less-Common Met*. **1974**, *34*, 39.
[204] F. Thirion, G. Venturini, B. Malaman, J. Steinmetz, B. Roques, *J. Less-Common Met*. **1983**, *95*, 47.
[205] F. Thirion, B. Malaman, G. Venturini, J. Steinmetz, B. Roques, *J. Less-Common Met*. **1984**, *96*, 153.
[206] B. Eisenmann, H. Schäfer, *Z. Anorg. Allg. Chem*. **1974**, *403*, 163.
[207] C. Zheng, R. Hoffmann, *J. Phys. Chem*. **1985**, *89*, 4175.
[208] C. Zheng, R. Hoffmann, *J. Am. Chem. Soc*. **1986**, *108*, 3078.
[209] B. Eisenmann, N. May, W. Müller, H. Schäfer, *Z. Naturforsch. B* **1972**, *27*, 1155.
[210] G. Cordier, E. Czech, H. Schäfer, P. Woll, *J. Less-Common Met*. **1985**, *110*, 327.
[211] A. Dommann, F. Hulliger, H. R. Ott, V. Gramlich, *J. Less-Common Met*. **1985**, *110*, 331.
[212] A. Szytula, J. Leciejewicz in *Handbook of the Physics and Chemistry of Rare Earths*, *Vol. 1* (Eds.: K. A. Gscheidner, Jr., L. Eyring), Elsevier Science, Amsterdam, **1989**, chap. 83.
[213] A. Purwanto, R. A. Robinson, H. Nakotte, I. P. Swainson, M. S. Torikachvili, *J. Appl. Phys.* **1996**, *79*, 6411.
[214] V. V. Gridin, S. A. Sergeenkov, A. Strydom, P. de V. du Plessis, *Phys. Rev. B* **1994**, *50*, 12995.
[215] W. P. Beyermann, M. F. Hundley, P. C. Canfield, C. Godart, M. Selsane, Z. Fisk, J. L. Smith, J. D. Thompson, *Physica B* **1991**, *171*, 373.
[216] M. Selsane, M. Lebail, N. Hamdaoui, J. P. Kappler, H. Noël, J. C. Achard, C. Godart, *Physica B* **1990**, *163*, 213.
[217] U. Rauchschwalbe, U. Gottwick, U. Ahlheim, H. M. Mayer, F. Steglich, *J. Less-Common Met*. **1985**, *111*, 265.
[218] B. Lloret, B. Buffat, B. Chevalier, J. Etourneau, *J. Magn. Magn. Mater*. **1987**, *67*, 232.
[219] R. A Steeman, A. J. Dirkmaat, A. A. Menovsky, E. Frikkee, G. J. Nieuwenhuys, J. A. Mydosh, *Physica B* **1990**, *163*, 382.
[220] W. Lin, H. Steinfink, E. J. Weiss, *Inorg. Chem*. **1965**, *4*, 877.
[221] R. Wang, H. Steinfink, W. F. Bradley, *Inorg. Chem*. **1966**, *5*, 142.
[222] J.-G. Park, I. P. Swainson, W. J. L. Buyers, M. H. Jung, Y. S. Kwon, *Physica B* **1998**, *241–243*, 684.
[223] T. H. Ramsey, H. Steinfink, E. J. Weiss, *Inorg. Chem*. **1965**, *4*, 1154.
[224] M. P. Pardo, J. Flahaut, L. Domange, *Bull. Soc. Chim. France* **1964**, 3267.
[225] S.-M. Park, S.-J. Park, S.-J. Kim, *J. Solid. State Chem*. **1998**, *140*, 300.
[226] J.-P. Marcon, R. Pascard, *C. R. Seances Acad. Sci. Ser. C* **1968**, *266*, 270.
[227] P. S. Bénazeth, D. Carré, P. Laruelle, *Acta Crystallogr. Sect. B* **1982**, *38*, 33.
[228] P. S. Bénazeth, D. Carré, P. Laruelle, *Acta Crystallogr. Sect. B* **1982**, *38*, 37.
[229] J. C. Chen, P. K. Dorhout, *J. Solid State Chem*. **1995**, *117*, 318.
[230] M. H. Jung, Y. S. Kwon, T. Kinoshita, S. Kimura, *Physica B* **1997**, *230–232*, 151.
[231] M. H. Jung, Y. S. Kwon, T. Suzuki, *Physica B* **1997**, *240*, 83.
[232] B. Foran, S. Lee, *J. Am. Chem. Soc*. **1994**, *116*, 154.
[233] A. van der Lee, L. M. Hoistad, M. Evain, B. J. Foran, S. Lee, *Chem. Mater*. **1997**, *9*, 218.
[234] B. Foran, S. Lee, M. Aronson, *Chem. Mater*. **1993**, *5*, 974.
[235] P. S. Bénazeth, D. Carré, M. Guittard, M. J. Flahaut, *C. R. Seances Acad. Sci. Ser. C* **1975**, *280*, 1021.
[236] M. Grupe, W. Urland, *J. Less-Common Met*. **1991**, *170*, 271.
[237] P. Plambeck-Fischer, W. Abriel, W. Urland, *J. Solid. State Chem*. **1989**, *78*, 164.

[238] B. K. Norling, H. Steinfink, *Inorg. Chem*. **1966**, *5*, 1488.
[239] E. DiMasi, B. Foran, M. Aronson, S. Lee, *Chem. Mater*. **1994**, *6*, 1867.
[240] G.-H. Gweon, J. D. Denlinger, J. A. Clack, J. W. Allen, C. G. Olson, E. DiMasi, M. C. Aronson, B. Foran, S. Lee, *Phys. Rev. Lett*. **1998**, *81*, 886.
[241] H. Noël, J. C. Levet, *J. Solid State Chem*. **1989**, *79*, 28.
[242] R. Patschke, J. Heising, M. G. Kanatzidis, P. Brazis, C. R. Kannewurf, *Chem. Mater*. **1998**, *10*, 695.
[243] R. Patschke, J. Heising, J. Schindler, C. R. Kannewurf, M. G. Kanatzidis, *J. Solid State Chem.* **1998**, *135*, 111.
[244] G. A. Landrum, http://overlap.chem.cornell.edu:8080/yaehmop.html **1995**.
[245] E. Brechtel, G. Cordier, H. Schäfer, *Z. Naturforsch. B* **1981**, *36*, 1341.
[246] O. Liebrich, H. Schäfer, A. Weiss, *Z. Naturforsch. B* **1970**, *25*, 650.
[247] N. A. Ignat'ev, Ya. A. Ugai, K. B. Aleinikova, N. S. Rabotkina, *J. Struct. Chem. (Engl. Transl.)* **1971**, *12*, 665.
[248] H. W. Mayer, I. Mikhail, K. Schubert, J. *Less-Common Met*. **1978**, *59*, 43.
[249] K. E. Al min, *Acta Chem. Scand*. **1948**, *2*, 400.
[250] W. K. Hofmann, W. Jeitschko, *J. Less-Common Met*. **1988**, *138*, 313.
[251] K. Deller, B. Eisenmann, *Z. Naturforsch. B* **1976**, *31*, 29.
[252] H. G. von Schnering, W. Hönle, G. Krogull, *Z. Naturforsch. B* **1979**, *34*, 1678.
[253] K. Deller, B. Eisenmann, *Z. Anorg. Allg. Chem*. **1976**, *425*, 104.
[254] A. Rehr, F. Guerra, S. Parkin, H. Hope, S. M. Kauzlarich, *Inorg. Chem*. **1995**, *34*, 6218.
[255] A. Kjekshus, T. Rakke, A. F. Andresen, *Acta Chem. Scand*. **1970**, *24*, 3309.
[256] T. Rosenqvist, *Acta Metall.* **1953**, *1*, 761.
[257] A. Kjekshus, T. Rakke, A. F. Andresen, *Acta Chem. Scand. Ser. A* **1974**, *28*, 996.
[258] B. R. Wang, H. Steinfink, *Inorg. Chem*. **1967**, *6*, 1685.
[259] N. L. Eatough, T. Hall, *Inorg. Chem*. **1969**, *8*, 1439.
[260] M. N. Abdusalyamova, *J. Alloys Comp*. **1993**, *202*, 15.
[261] M. Brylak, W. Jeitschko, *Z. Naturforsch. B* **1995**, *50*, 899.
[262] J. Dünner, A. Mewis, M. Roepke, G. Michels, *Z. Anorg. Allg. Chem.* **1995**, *621*, 1523.
[263] J. Weiss, H. Schäfer, B. Eisenmann, G. Schön, *Z. Naturforsch. B* **1974**, *29*, 585.
[264] I. Schewe, P. Böttcher, H. G. von Schnering, *Z. Kristallogr.* **1989**, *188*, 287.
[265] E. W. Breeze, N. H. Brett, J. White, *J. Nucl. Mater.* **1971**, *39*, 157.
[266] J. A. Cody, J. A. Ibers, *Inorg. Chem*. **1995**, *34*, 3165.
[267] H. Noël, *Inorg. Chim. Acta* **1985**, *109*, 205.
[268] T. Hughbanks, R. Hoffmann, M.-H. Whangbo, K. R. Stewart, O. E. Eisenstein, E. Canadell, *J. Am. Chem. Soc*. **1982**, *104*, 3876.
[269] K. Tatsumi, A. Nakamura, P. Hofmann, P. Stauffert, R. Hoffmann, *J. Am. Chem. Soc*. **1985**, *107*, 4440.
[270] K. Stöwe, *J. Solid State Chem*. **2000**, *149*, 123.
[271] K. Stöwe, *Z. Anorg. Allg. Chem*. **2000**, *626*, 803.